

ALMA MATER STUDIORUM · UNIVERSITÀ DI BOLOGNA

SCHOOL OF ENGINEERING AND ARCHITECTURE

Master Thesis in Civil Engineering

Curriculum Structures

**Data analysis of collapse mechanisms of a 3D printed
groin vault in shaking table testing**

Supervisor:

Prof. Ing. Stefano SILVESTRI

Candidate:

Beatrice RAGNUCCI

Student number:

Co-supervisor:

Dr. Ing. Simonetta BARACCANI

892064

Third Graduation Session

Academic Year 2019/2020

Table of contents

Abstract.....	3
1. Introduction.....	5
1.1 Context.....	5
1.2 Masonry vaults: an overview	6
1.3 Collapse mechanisms.....	8
1.3.1 Arches	8
1.3.2 Barrel vaults.....	9
1.3.3 Groin vaults	10
1.4 Testing on groin vaults.....	13
2. The SEBESMOVA3D Project.....	21
2.1 Geometrical model.....	21
2.2 Material properties.....	23
2.3 Construction phases	25
2.4 The experimental campaign	26
3. Objectives and methodology	34
3.1 Selection of the reference system	36
3.2 Initial time of the input signal	39
3.3 Cleaning of the initial window	40
4. Collapse mechanisms	44
4.1 Comparison among configurations.....	45
5. Collapse displacements	57
5.1 Dynamic properties of the vault	57
5.2 Fixed configuration.....	59
5.3 Moveable configuration	65
6. Critical arch elongation	72
Conclusions.....	82
References.....	83
Acknowledgments.....	85

Abstract

Why preserve historical buildings?

All the reasons to explain the importance of preservation are based on common concepts: the lesson from the past, the awareness of the present and the basis for the future. It is a matter of human identity preservation, and as such must be protected.

In this regard, it is known that the assessment of seismic events is of great importance, given the vulnerability of historical buildings to earthquakes. Several studies have been conducted along this line, to investigate the complex response and predict the behaviour of vulnerable structures in masonry historic buildings. Moreover, innovative ways have been used to capture and read the data, like the definition and calibration of FEM and DEM models. In this context, the “SEBESMOVA3D” project (SEismic BEhavior of Scaled MOdels of groin VAults made by 3D printers) finds its way, granted by the Seismology and Earthquake Engineering Research Infrastructure Alliance for Europe SERA.

The aim of the “SEBESMOVA3D” project is to investigate the behaviour of a 2m x 2m model of a masonry groin vault, which was built by the assembly of blocks made of a 3D-printed plastic skin filled with mortar. The choice of the groin vault is due to the large presence of this vulnerable roofing system in historical churches. The purpose is not to study a particular vault, but to create a suitable model to explore different boundary conditions and configurations. Experimental tests on the shaking table are carried out to study the vault response on two support boundary conditions, involving four lateral confinement modes. The data processing of markers displacement allow to examine the collapse mechanisms of the vault, based on the arches deformed shapes. There then follows a numerical evaluation, to provide the orders of magnitude of the displacements associated to the previous mechanisms. Given that these displacements are related to the arch shortening and elongation, the last objective is the definition of a critical elongation between two diagonal bricks and consequently of a diagonal portion. This study aims to continue the previous work and to take another step forward in the research of ground motion effects on masonry structures.

And that is because, research means to understand the past, to know the present and to be prepared for the future. Therefore, research is the way to preservation.

1. Introduction

1.1 Context

The seismic impact on the historical heritage is a threat to its preservation, and the most effective way to face it, is research, that means knowledge. Knowledge of the dynamic behaviour of the most vulnerable structural elements is the key to understand and take interventions. Among these, masonry vaults deserve a deeper attention. Given the limited information in literature about the seismic assessment of masonry groin vaults, the SEBESMOVA 3D project reveals its innovation.

The project consists of a shaking table experimental campaign on a scaled model of a groin pointed vault, held at the EQUALS Laboratory at the University of Bristol (UK). The 2m x 2m in-plan vault model considers dry joints (unilateral joints with an interposed elastic gum layer) between the voussoirs and is built in an innovative way, with blocks made of a 3D-printed plastic skin filled with mortar, to permit quick repetition of tests, carried out until collapse [1]. Indeed, the advantage of this technology is that the blocks are more resistant to the excitations than the clay bricks, and they are meant to be reused after each test.

Since masonry can be considered as an assembly of rigid particles that are bricks, each block plays an essential role in the stability and equilibrium of the vault. The shape of the blocks is therefore studied and clearly designed. Then the inner core is filled up with mortar to provide the proper mass for the dynamic tests. A specific formwork is designed and used to facilitate the assembly at the beginning and after each collapse. Once the vault is built, it is subjected to horizontal seismic excitations, with different supporting conditions, in order to determine the seismic behaviour of the structure.

The data acquisition system is composed by accelerometers and a system of image capture, relying on light-reflecting markers. After a work on data processing of the markers displacements, comparisons among the results of the tests are carried out, in terms of collapse mechanisms and critical values.

The purpose is to expand knowledge of masonry behaviour affected by ground motions, by taking advantage from the innovative 3D printing technology and an efficient operational background.

1.2 Masonry vaults: an overview

Masonry is defined as the building of structures from individual units, which are often bound together by mortar. The main assumptions on masonry were formulated by Heyman (1966) with the “Rigid No-Tension Model”, that considers masonry as a rigid material and without tensile strength:

- 1) Masonry cannot withstand tension, because the adhesion between mortar and bricks is very low and can be neglected.
- 2) Masonry has infinite compressive strength, considering that failure is generally due to a loss of equilibrium rather than a material failure.
- 3) Masonry has infinite shear strength.
- 4) Elastic deformations are negligible, because in the majority of cases strains are very small and the focus is on the collapse analysis [1].

It follows that a masonry structure behaves as composed by rigid blocks, that can move with rigid displacements generating a so called “mechanism”.

Among masonry structures, the vault is one of the most used to cover a space with a ceiling or roof. It is a structural member consisting of an arrangement of arches. The basic barrel form (**Figure 1**), that first appeared in ancient Egypt and the Middle East, is in effect a continuous series of arches deep enough to cover a three-dimensional space. The static behavior of the barrel vault can be viewed as that of a series of side-by-side arches. Indeed, it exerts the same kind of thrust as the circular arch and must be buttressed along its entire length by heavy walls with limited openings [2].

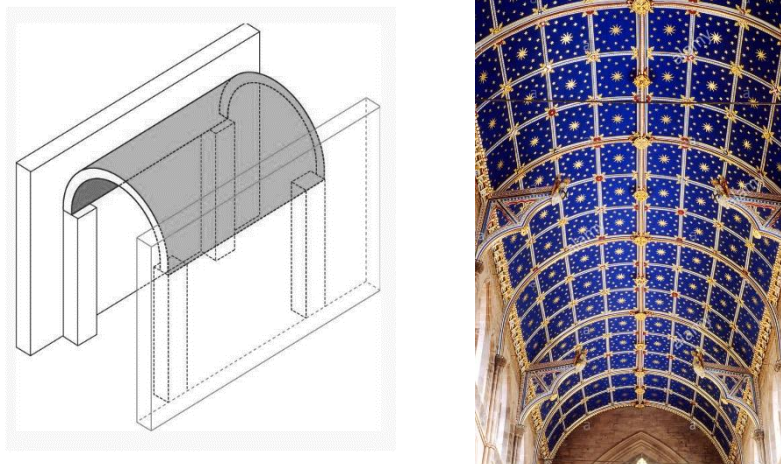


Figure 1: Barrel vault: scheme and example.

Roman architects discovered that two-barrel vaults that intersected at right angles formed a groin vault (also named cross vault), which, when repeated in series, could span rectangular areas of unlimited length (**Figure 2**) [2]. Because thrusts are concentrated at all four corners, the groin vault is supported by four pillars or columns placed in the angles and the supporting walls need not be massive. The word “groin” refers to the edge between the intersecting vaults [3]. This vault was widely used in the architecture of the ancient Romans and in the churches of the early Middle Ages.

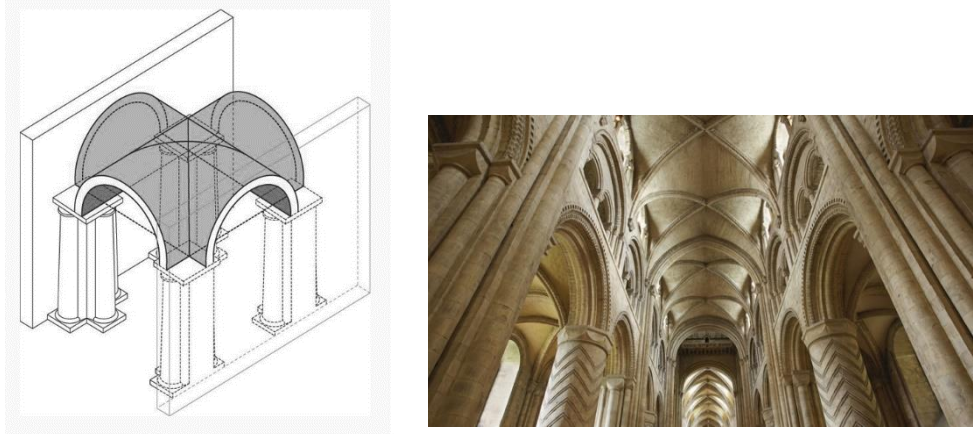


Figure 2: Groin vault: scheme and example.

During the gothic period, the groin vault was replaced by the more advanced rib vault (**Figure 3**). The rib vault is composed of a framework of crossed or diagonal arched ribs. It is easier to construct, stronger and more flexible than the previous ones. The round arches of the barrel vault are replaced by pointed arches [2], in such a way that ribs transmit the load downward and outward to specific points, usually rows of columns or piers. This allows the construction of higher and thinner walls and much larger windows.

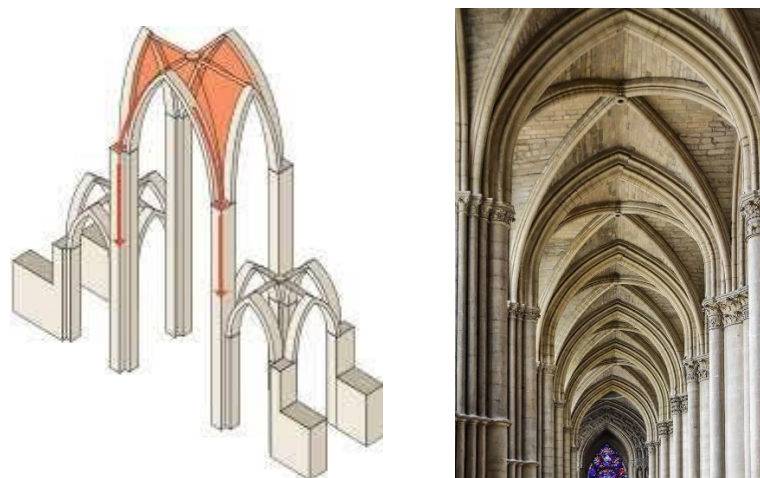


Figure 3: Rib vault: scheme and example.

1.3 Collapse mechanisms

1.3.1 Arches

Since a vault is an arrangement of arches, first of all their collapse mechanism should be studied. A masonry arch is able to sustain loads solely by virtue of compressions [slides]. For a circular arch under its own weight, the shape of the Line Of Thrust (LOT), that is a theoretical line representing the path of the resultants of the compressive forces through the structure, is a catenary. If the LOT lies entirely within the thickness of the arch, the arch is safe and there won't be the collapse. In fact, the mechanism activates only when the axial force touches the edge of arch in four points, generating four hinges. This situation is more likely to happen as the arch is reduced in thickness and the LOT is no more completely contained within the thickness of the arch. Therefore, a minimum thickness was determined by Couplet (1731) for the circular arch, being t the thickness and r_i its internal radius:

$$t/r_i = 0.108$$

According to the theory of Limit Analysis proposed by Heyman, it can be demonstrated that if it is possible to draw a line of thrust within an arch, then this arch is safe (corollary of the Safe Theorem of Limit Analysis) [4]. **Figure 4** summarizes these considerations.

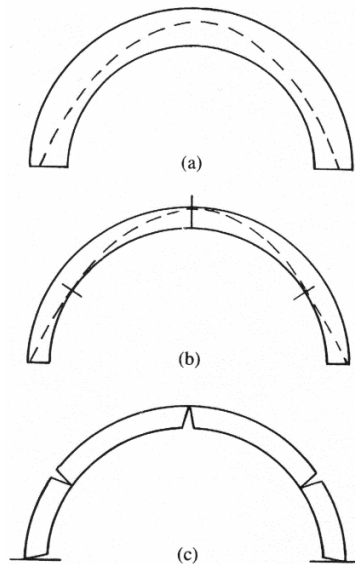


Figure 4: (a) An arch of sufficient thickness can contain infinite LOT; only one is drawn. (b) Limit thickness, where only one LOT can be drawn within the arch. (c) Formation of hinges at the contact points of LOT with the masonry limit.

The next step of the analysis consists in computing a factor capable of stating the degree of safety of the structure.

Heyman suggested to reduce the arch in thickness by shifting both the extrados and intrados profiles in a homothetic manner until they touch the line of thrust. The outcome is an ideal arch, of reduced thickness, contained within the real one (**Figure 5**). The ratio between the thickness of the real arch and the thickness of the ideal arch is defined to be “*the geometrical factor of safety*” of the structure [1].

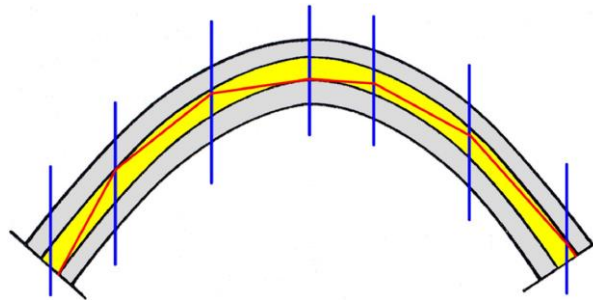


Figure 5: Real and ideal arch.

1.3.2 Barrel vaults

For a barrel vault, a set of parallel arches is a realistic assumption for its load-bearing action under self-weight. If the imposed load must be carried by a single load, the load capacity of the vault will be limited by the capacity of that one arch. If the point load is at midspan, a possible load path could bring down the forces to the line supports [1]. Therefore, the better interpretation is a superposition of these two networks (**Figure 6**). The vault can be imagined as divided in a series of arches working separately, each one with its respective line of thrust.

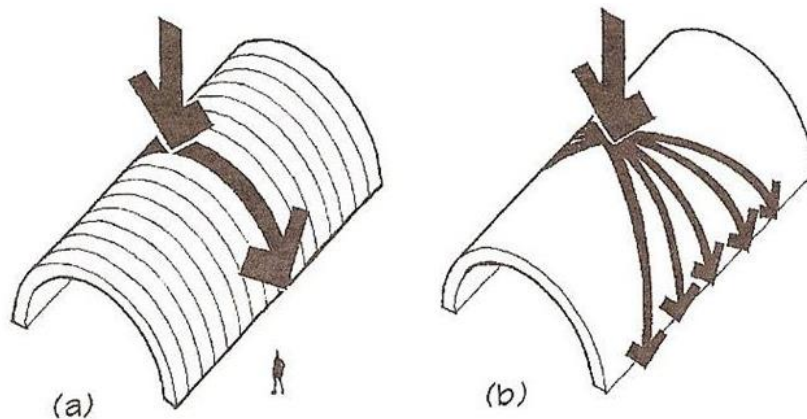


Figure 6: Load distribution in: (a) independent arches and (b) the vault.

1.3.3 Groin vaults

In case of a groin vault, the diagonals can be assumed as two main arches, subjected to the alternate horizontal and vertical load of the two adjacent webs. For this reason, the LOT does not remain coincident with the shape of arches and the ribs, pushing out the head of columns, will generate thrust at the supports. Therefore, the load will concentrate at the intersection of the two barrel vaults, and the action along the diagonals.

An overview of the main steps in the comprehension of the structural behaviour of groin vaults is presented below.

- 1) The first to write a scientific contribution for damage understanding in masonry construction was Mastrodicasa [5] in 1943. According to his theoretical model, masonry is assumed as absolutely brittle, homogeneous, isotropic and linearly elastic. Whatever the causes of vault damages, the crack opening (due to small tensile strength) allows the structure to find a new equilibrium state (**Figure 7**).

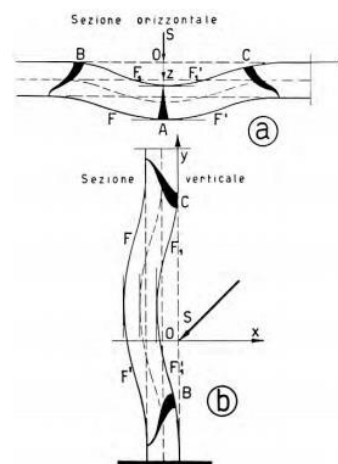


Figure 7: Crack pattern in a wall in case of an inclined point load (Mastrodicasa, 1943).

- 2) The two collapse mechanisms for cross vaults are indicated in the Recovery manual for the historical centre of Città di Castello [6], reported in **Figure 8**:
 - the first mechanism is in good agreement with Mastrodicasa and it is characterized by the outward movement of the abutment with the consequent detachment of one of the webs and hinges formation at the springings and at the crown.

- the second mechanism is mostly a shear failure caused by the relative movement of the two opposite sides of the vault; it is characterized by the typical diagonal crack occurrence.

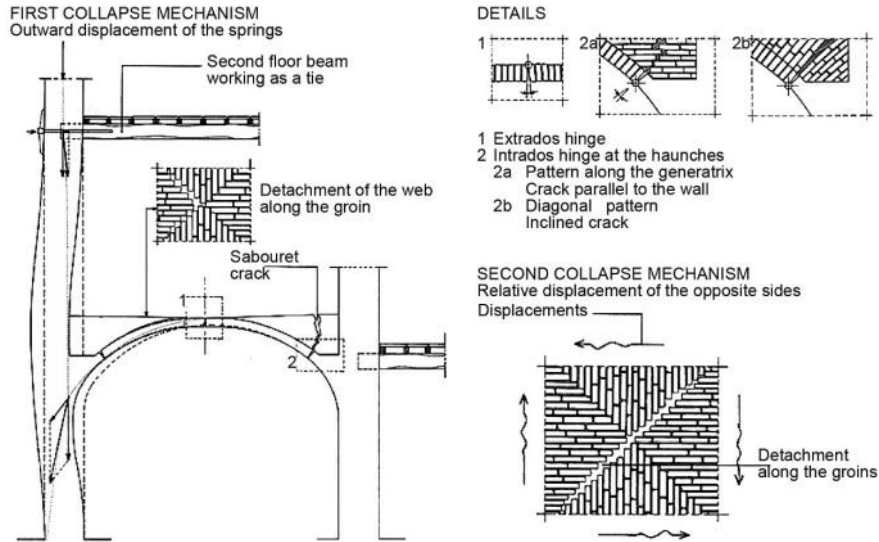


Figure 8: Collapse mechanisms for a cross vault (Giovannetti, 2000).

3) It appears that the first study of gothic vault cracks was made by the French engineer Sabouret, for which cracks are the result of the external deformation, imposed by the environment, on the structure. Sabouret cracks form parallel to the edges if the ribs have a more pronounced cross section, by marking two different regions of the vault: band *a* and band *b* (Figure 9).

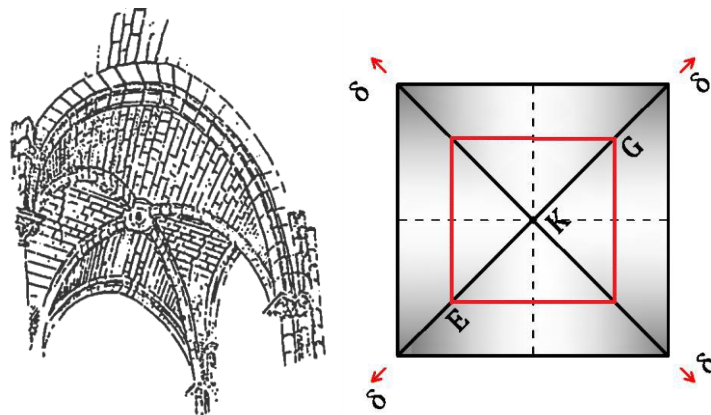


Figure 9: Typical Sabouret cracks (red lines).

The webs behave as a series of arch strips. In band b [1], as the ribs move out, the span of the little arch increases as if there was a settle, so central hinges form at the extrados and two additional hinges form at the intrados (**Figure 10**).

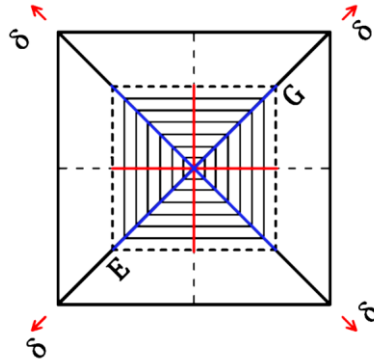


Figure 10: Behaviour in band b : extrados hinges (red line), intrados hinges (blue line).

In band a [1], the situation is similar to band b , but because the two external parts move as a rigid motion, the two hinges at the intrados form at the same location, even if the arches are longer and longer (**Figure 11**).

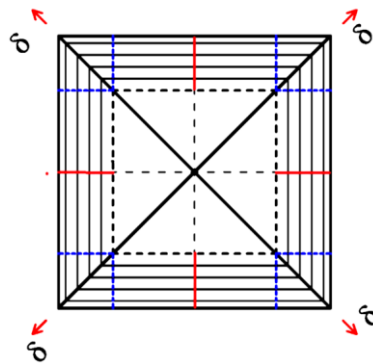


Figure 11: Behaviour in band a : extrados hinges (red line), intrados hinges (blue line).

- 4) A graphical explanation of the collapse mechanism is given by Holzer [7] in 2011 (**Figure 12**). In the analysis of the collapse mechanism of a simple barrel vault with lunettes on spreading supports, the lunettes may or not move together with the main vault depending on masonry bond. Considering the groin vault as a generalization of the vault with lunettes, the same approach can be followed but, in this case, the Sabouret cracks represent the most frequent mechanism [8].

5) Moreover, Como [9] in 2013 analyzed a semi-circular shaped cross vault on a square plan, undergoing uniform diagonal widening. **Figure 13** shows the possible crack pattern at the intrados and extrados.

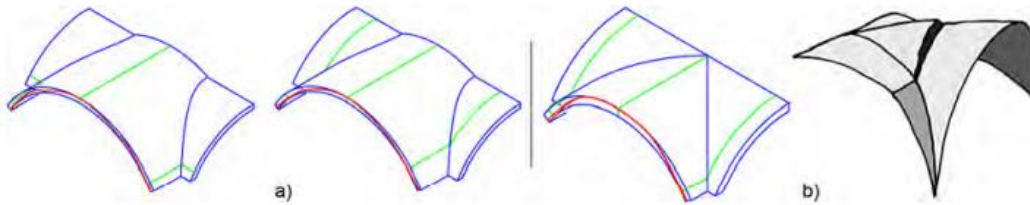


Figure 12: Collapse mechanisms (Holzer, 2011): (a) barrel vaults with lunettes and (b) failure mechanism for cross vaults.

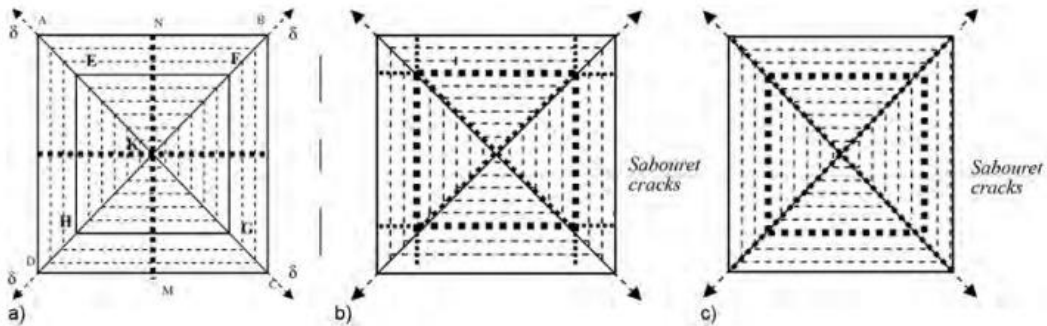


Figure 13: Sabouret crack pattern (Holzer, 2011): (a) intrados, (b) and (c) extrados.

1.4 Testing on groin vaults

To follow, a brief digression on the experimental activities performed over the years on groin/cross vaults.

- One of the first experiments on cross vaults was performed by Mark et al. in 1973 [10], who applied the photo-elastic technique to experimentally determine the stresses in two bays of the 13th century choir vaults of Cologne Cathedral. A few years later in 1982, Mark performed the in-plane analysis of the cross-section of Mallorca Cathedral in comparison with the FEM elastic analysis [11].

- In 1996, Ceradini [12] investigated the effect of imposed deformations in a full-scale brickwork cross vault having a 7.36 m span without ribs. The outward movement of all the supports caused a fracture equal to 2.5% of the span.
- Faccio et al. in 1999 [13] analyzed the action of a monotonic point load to a rib cross vault (**Figure 14**).

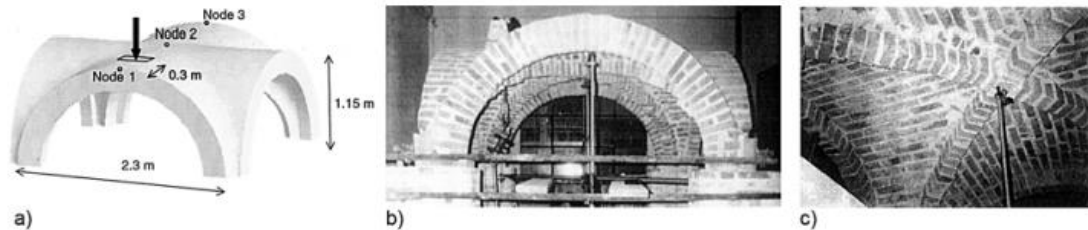


Figure 14: Test by Faccio et al.: (a) geometry and load condition, (b) experimental setup, (c) central transducer.

- Later, in 2002, Theodossopoulos et al. [14] studied the effect of dead loads and horizontal displacement of the abutments, on a wooden 1:4 scale model, that represented an aisle vault of the partially collapsed Abbey Church of Holyrood in Edinburgh (**Figure 15**).

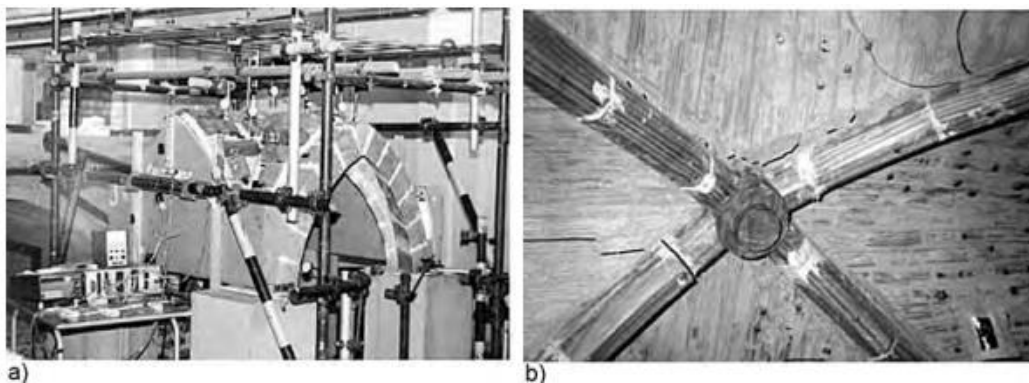


Figure 15: Test by Theodossopoulos et al.: (a) loading arrangement, (b) crack formation at the intrados around the keystone.

- Then, Foraboschi et al. in 2004 [15] considered an isolated brickwork cross vault on four pillars under an incremental load applied to the centre of a web (**Figure 16**), in which failure was dictated by the insufficient buttressing action of the webs adjacent to the loaded web.



Figure 16: Test setup by Foraboschi.

- Van Mele et al. [16] examined in 2012 the collapse of a 3D-printed scale model of a groin vault under large support displacement and compared the results with DEM analysis (3DEC). The vault had a span of 150 mm and a thickness of about 24.4 mm. Only one support was subjected to three different displacements, namely transverse, diagonal and vertical (all applied quasi-statically). While the diagonal displacement showed similar results, the comparison between transverse displacement and DEM output revealed a great discrepancy, probably due to the premature sliding and twisting movements in the physical model [8] (**Figure 17**).



Figure 17: Comparison of (a) diagonal and (b) transverse support displacement.

- As regards the seismic performance of masonry cross vaults, in 2014 Rossi et al. [17] performed three monotonic and one cyclic tests on a 1:5 scale model of a groin vault made by 3D printed plastic blocks with dry joints, reproducing the typical condition of a cross vault in a lateral aisle undergoing longitudinal seismic action.

The damaged mechanism was characterized by the presence of plastic hinges as well as the diagonal crack (**Figure 18**). Small sliding occurrences were observed close to the springings [8]. The ultimate displacement capacity resulted to be equal to 4%.

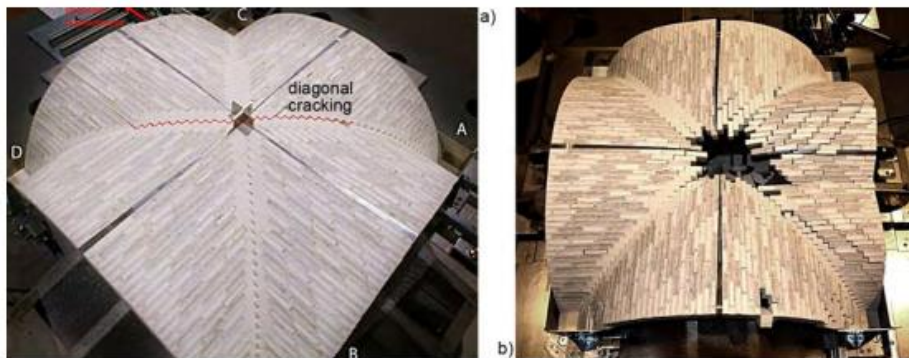


Figure 18: Diagonal cracking of a scaled model of a groin vault made by 3D printed plastic blocks with dry joints.

- Shapiro [18] performed several tests in 2012 on a barrel and a groin vault considering: i) spreading supports, ii) vertical point loads applied on the extrados, iii) point loads applied to the initially deformed vault, and iv) horizontal acceleration through tilting. The vault was tested according to two directions, namely parallel and rotated by 45° with respect to one of the web generatrix, exhibiting a capacity of 0.67 g and 0.80 g respectively [8] (**Figure 19**).

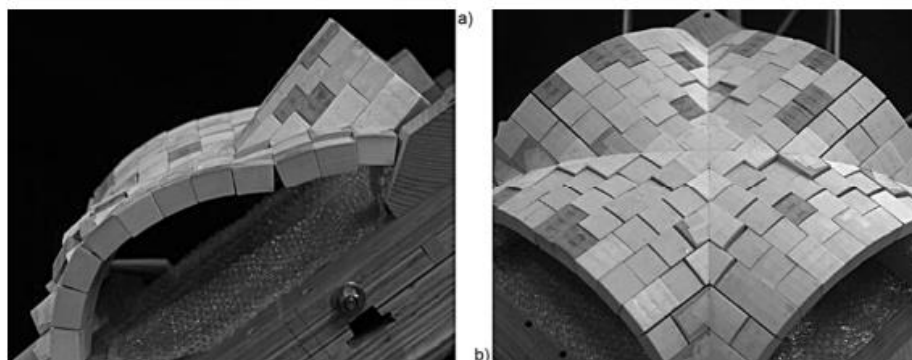


Figure 19: Collapse mechanism of a tilted groin vault: a) parallel and b) rotate by 45°.

- Focusing on shaking table experiments from now on, two masonry cross vaults were tested in 2012 within the European Programme NIKER (in NTUA, Athens) and PERPETUATE (in ENEA Casaccia Research Center) [19].

The first test is performed on a 2.705m x 2.60m cross vault of the monument of Katholikon of Dafni Monastery made of Byzantine type bricks, supported by two masonry piers 0.45 m thick and 2.60 m tall. The model was subjected to increased scaled motions in x direction (parallel to the piers) up to damage and tests were performed using the first 40 s of the signals recorded at Calitri during the earthquake in Irpinia (Southern Italy). The damage was severe and characterized by detachment from the piers, cracks and sliding at the frontal arches and by horizontal cracks at the piers. A permanent deformation of 15 mm with respect to the vertical axis was registered [8]. The tested cross vault is shown in **Figure 20**.



Figure 20: Tested cross vault in NTUA: a) interior view; b), (c), (d) damages at the end of the test.

The second test, reported in **Figure 21**, investigates a full-scale 3m x 3m masonry cross vault of the Mosque of Dey in Algiers, presenting wooden ties along the longitudinal direction, probably used as an ancient seismic technique. To simulate the drift in its horizontal plane in real boundary conditions, the wall was fully fixed whereas the columns were free to horizontally move and rotate. The signal

input was the Keddara (Algeria) accelerogram normalised and rescaled to the site of Kasbah of Algiers where the mosque is located. After a first campaign of tests with tie rods, the specimen was tested without them according to four assigned nominal Peak Ground Accelerations (PGAs), specifically 0.10g, 0.15g, 0.20g and 0.25g [11].

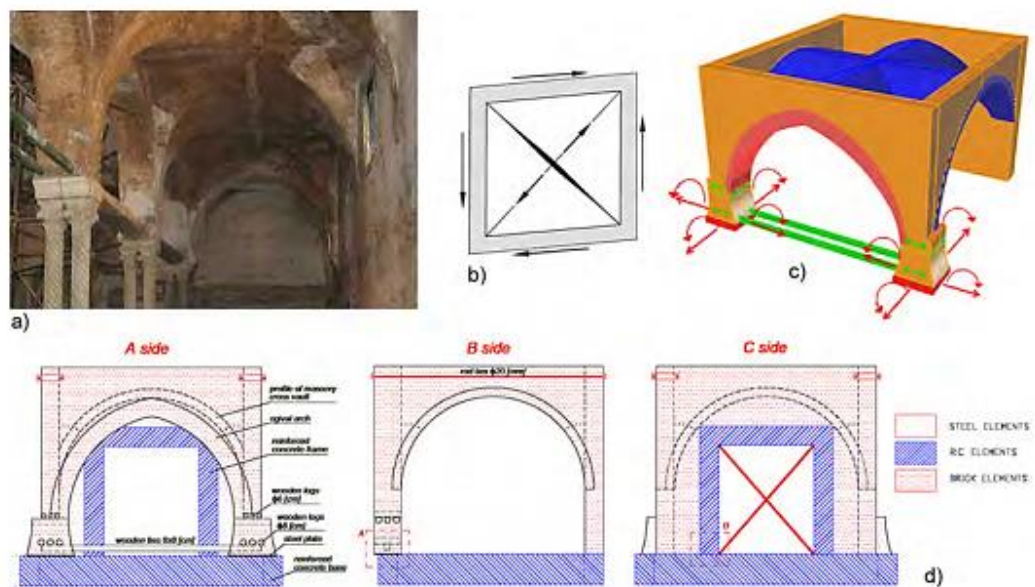


Figure 21: Tested cross vault in ENEA: a) vaulted structure of the Mosque, b) damage mode of the vault, (c) allowed displacement, (d) vault geometry.

- In 2016, Gaetani [8] performed different experimental tests on the 1:5 scaled groin vault made by dry-joint 3D printed plastic blocks, which was adopted by Rossi et al. in 2014. The groin vault was tested under two different conditions, namely:
 - (a) two displacement settings, representing damage mechanisms recurrently observed during post-earthquake surveys, i.e. in-plane horizontal shear distortion and longitudinal opening/closing of the abutments (**Figure 22**);
 - (b) horizontal inertial forces proportional to the mass of the structure (**Figure 23**).
 In the shear test, the maximum force was attained at about 3% of the shear displacement-to-span ratio, a little more than half of its collapse value. As regards the tilting tests, the ultimate angle of tilting was evaluated in the range $18^\circ \div 19.2^\circ$, to which corresponds a value for the ultimate horizontal load multiplier in the range $0.32 \div 0.35$.

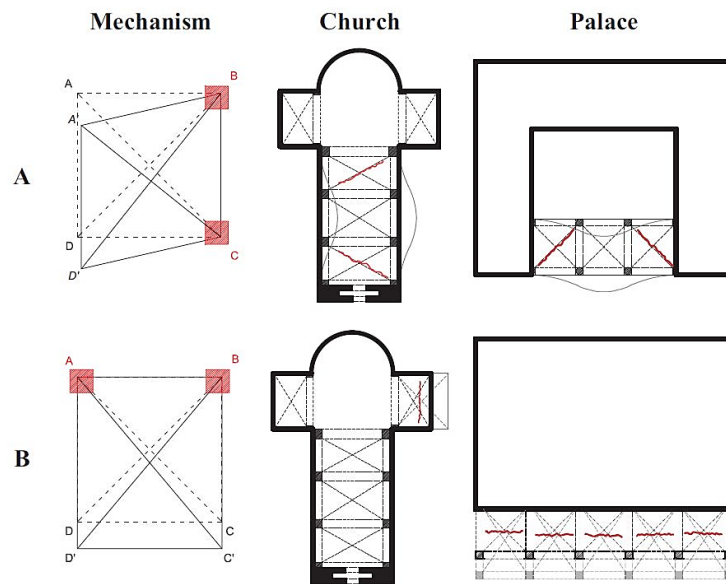


Figure 22: Displacement settings: A) in-plane horizontal shear distortion, b) longitudinal opening/closing of the abutments.

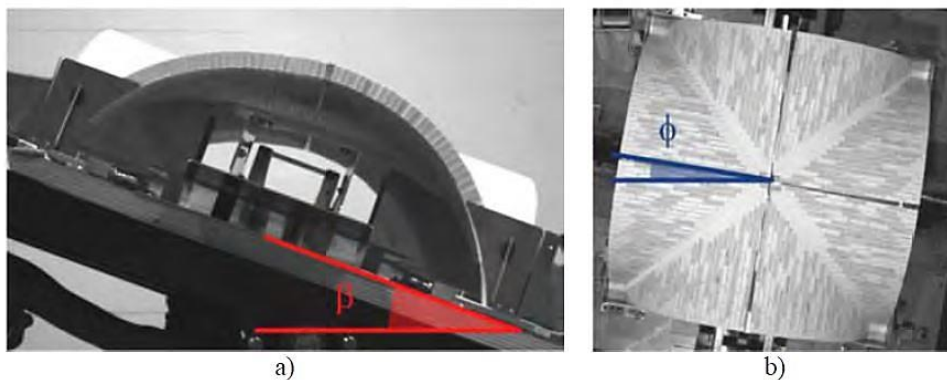


Figure 23: Tilting tests: a) tilting angle, b) rotation around its orthogonal axis.

- In 2018, Carfagnini et al. [20] investigated a 1:4 scaled model of a typical quadripartite square Gothic cross vault, from the aisle of the Holyrood Abbey in Edinburgh. The model was built with timber blocks and lime mortar, and the shear displacement was applied by moving two abutments in the longitudinal axis until failure. The crack pattern evolution and the ridge displacements were then recorded, identifying the diagonal cracks normal to the shear displacement that cause the damage and collapse in the vault. Regarding crack pattern stages, failure resulted to happen essentially at 3% spread of the longitudinal span (**Figure 24**). Linear and non-linear numerical models validated the crack pattern and confirmed

the uplift of the ridges and the concentration of the damage along the shear diagonal.

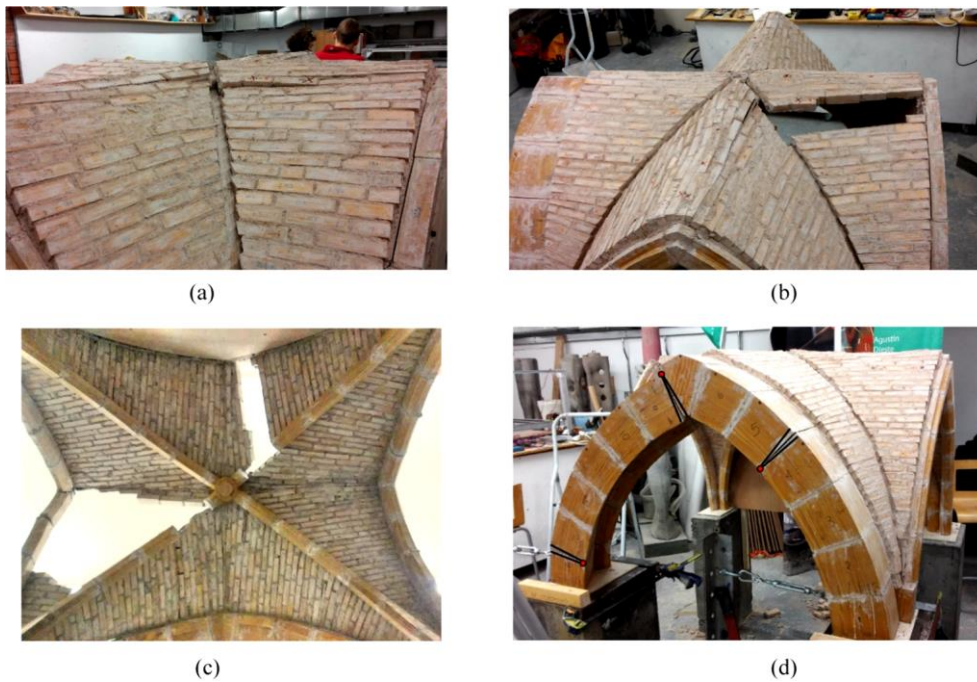


Figure 24: a) Crack pattern at shear displacement of 30 mm (around 3%), (b) collapse at shear displacement of 35 mm, (c) partial collapse at 50 mm, (d) hinges on the nave arch at 45 mm.

Coming to the end of this overview, the SEBESMOVA3D Project, on which the present work is focused, takes place. The aim is to take another step forward in the experimental field research of ground motion effects on masonry cross vaults, by performing shaking table tests on a 3D printed scaled model of a groin vault.

2. The SEBESMOVA3D Project

2.1 Geometrical model

The model represents a groin vault that can be found in many historical buildings. The vault has been truncated at its base, because generally collapse affects its free height rather than the base level. This is due to the fact that in historical churches, vaults are embedded in walls or pillars, as can be seen in **Figure 25**. The model of the 2m x 2m tested groin vault is visible in **Figure 26**.

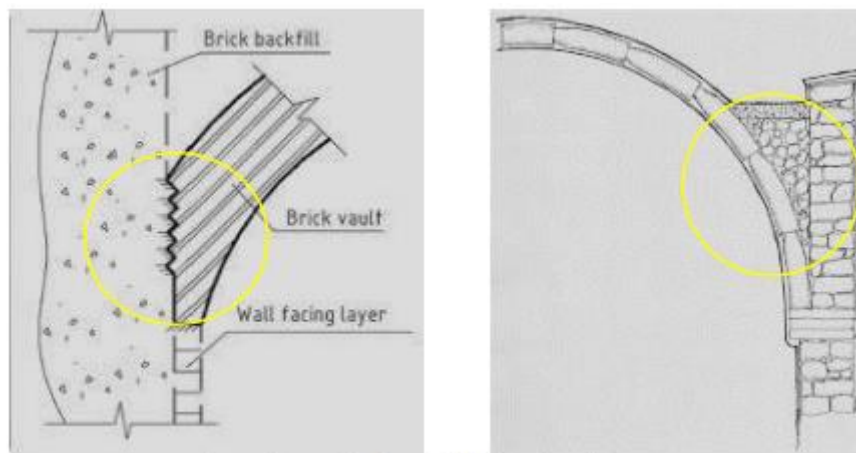


Figure 25: Vault embedding at the base.

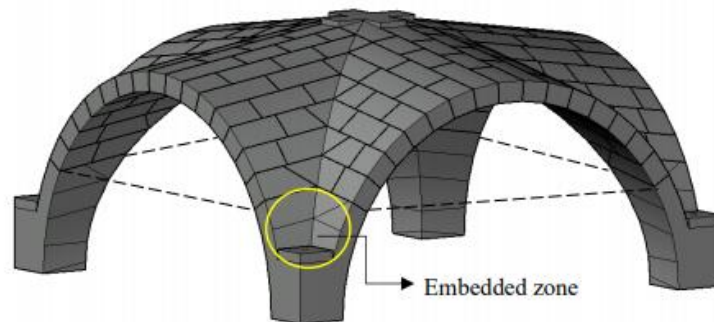


Figure 26: Model of the vault.

To represent in a proper way the boundary conditions at the embedded zone, the geometry of the base bricks has been specifically designed, as shown in **Figure 27**.

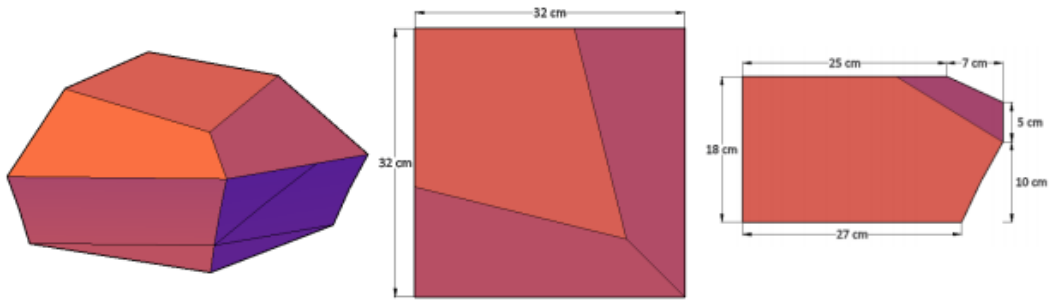
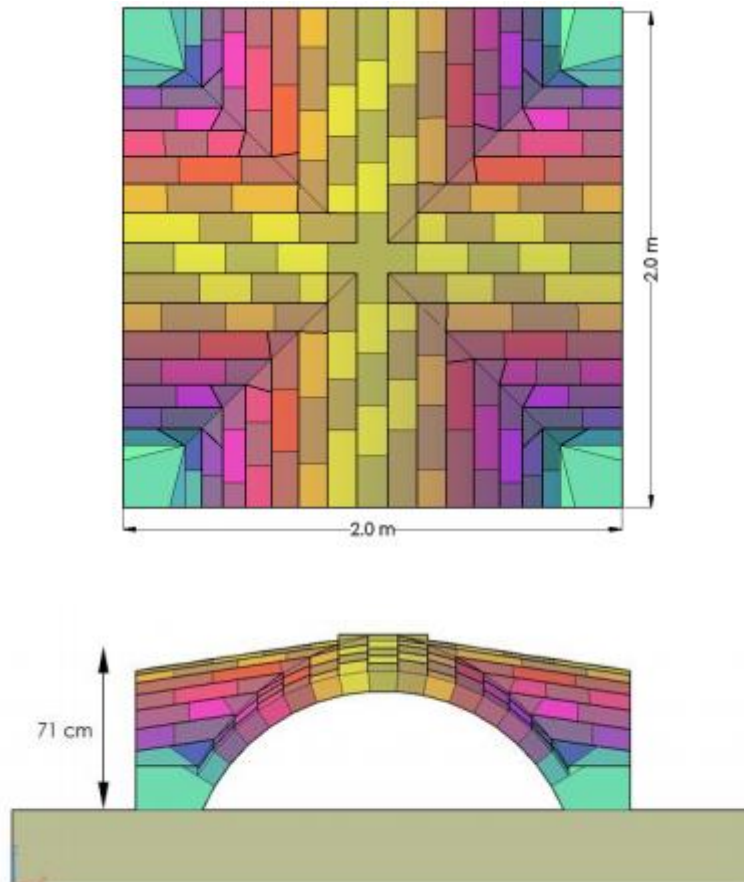


Figure 27: Base bricks geometry.

The shape and dimensions of the 173 plastic-mortar bricks, including the four blocks at the bases and the keystone at the top, have been studied with the help of an expert on Stereotomy, so that each of them is essential in the equilibrium of the vault. Their dimensions vary within a range of 20-25 cm in length, 10-15 cm in depth and 8 cm in thickness. The final design of the vault is shown in **Figure 28**.



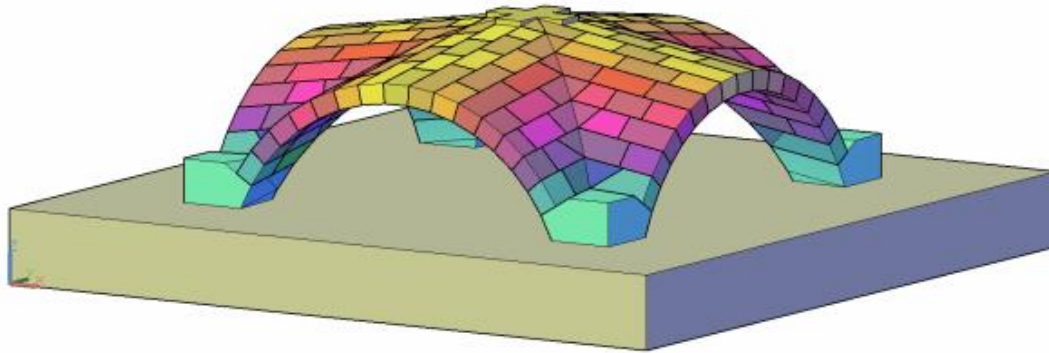


Figure 28: Plant, prospect and perspective view of the model.

As regards the shaking table, it is a 3m x 3m platform, able to carry up to 15 tonnes and to reach an acceleration up to 5g with peak displacements of ± 150 mm. Steel plates 2 cm thick are attached to the table to ensure a fixed condition at the base, by preventing the movement of the four corner blocks.

2.2 Material properties

The 173 3D printed blocks that compose the vault are made of PLA, polylactic acid, that is a completely compostable and biodegradable polymer obtained from the processing of plants rich in dextrose. The choice of the 3D printing technique is due to the low level of damage of plastic-mortar bricks, that allows an easy repeatability of the tests. The thickness of the plastic covering of the blocks is 2.5-3 mm. They are characterised by a hollow section and filled with a coat plaster for low to medium suction and smooth backgrounds (**Figure 29**).



Figure 29: Bonding Coat by British Gypsum used in the experimental campaign.

It was necessary to ensure an acceptable friction at the interfaces of blocks, especially because there is not a bonding contact material among bricks. Therefore, a thin gum layer is added to verify whether the slippage is reduced or not, and three cases are examined with the respective friction angle in **Table 1**.

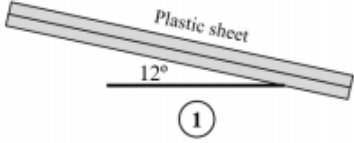
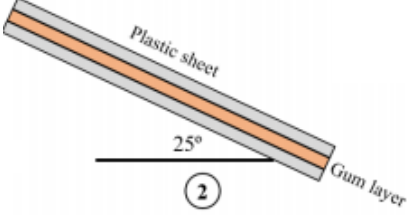
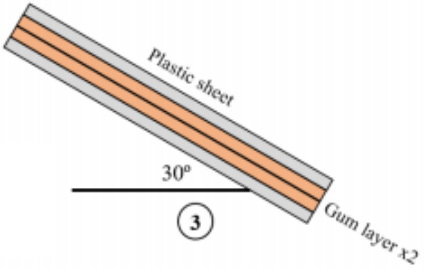
Configuration	Friction angle	Layout
(1) <i>Plastic-plastic</i>	12°	
(2) <i>Plastic-gum-plastic</i>	25°	
(3) <i>Plastic-gum-gum-plastic</i>	30°	

Table 1: Gum-plastic configurations.

The less effective solution results to be the plastic-plastic contact, due to the risk run even from the assembly process. On the contrary, the other two configurations show a similar behaviour. In the end, the third solution is preferred in order to achieve the least possible slippage.

2.3 Construction phases

The 3D printed plastic-mortar blocks have been produced in Bari and then moved to the laboratory of Bristol, where shaking table tests have been performed.

The construction is made up of several steps:

- Positioning of the four steel plates at the four corners of the shaking table to prevent the base blocks to move (**Figure 30**).



Figure 30: Corner steel plates.

- Assembly (only once at the beginning) of the skeleton and subsequent removal in order to fill up the plastic blocks with mortar (**Figure 31**).



Figure 31: Pre-assembly of the vault with empty blocks.

- Installation of a formwork specifically designed for the project, as a help to assemble and rebuild the vault after each collapse, by minimizing time and construction issues. The blocks positioning starts from the corners to complete firstly the perimetral arches. After that, webs and ribs are assembled, and keystone is placed (**Figure 32**).

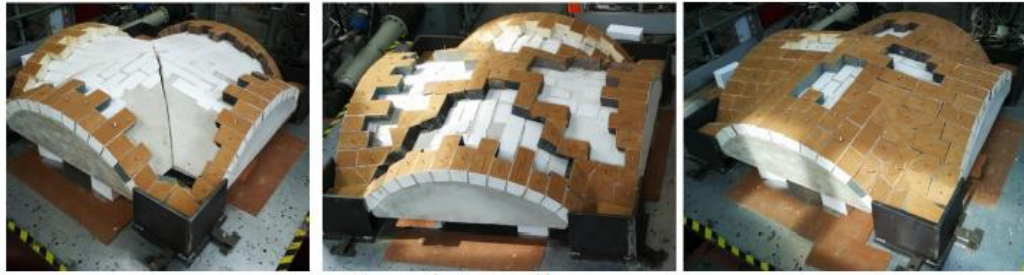


Figure 32: Assembly phases.

- Once the assembly is completed, the formwork is removed with the help of a jack and some little settlements are expected. To support the vault and simulate the presence of other structural systems on the perimeter, wooden or plexiglass panels are used during the testing phase (**Figure 33**).



Figure 33: Formwork removal.

2.4 The experimental campaign

Several configurations were tested depending on two base boundary conditions and four different types of lateral confinement.

The two base boundary conditions in question are:

1. Fixed (**Figure 34**): the vault was placed on four steel plates that were fixed on the shaking table.
2. Moveable (**Figure 35**): the vault was placed on two fixed steel plates and on two moveable carriages running in the Y direction on bearings along a pair of 40mm-diameter rails regulated by horizontal springs to give a combined stiffness of 16 kN/m.

The configurations of fixed base and moveable springings will be referred to as Configurations 1 and 2, respectively [1].

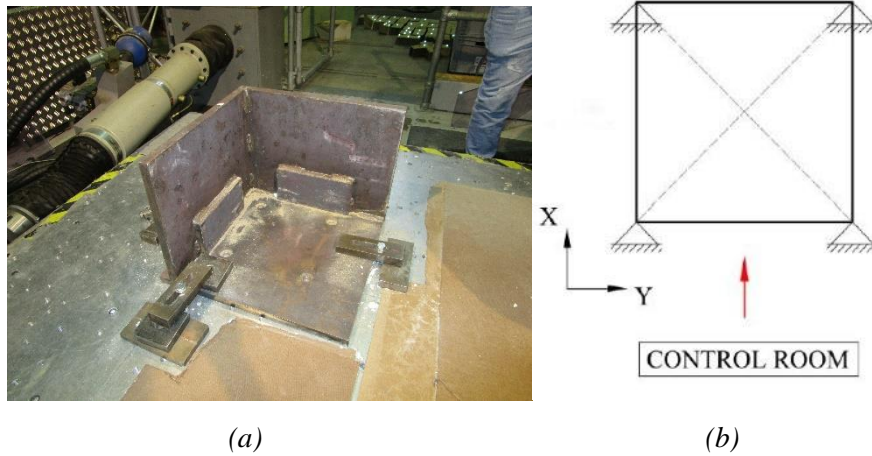


Figure 34: (a) Steel plates firmly clamped to the table to realise the fixed restraints. (b) Scheme of Configuration 1: fixed.

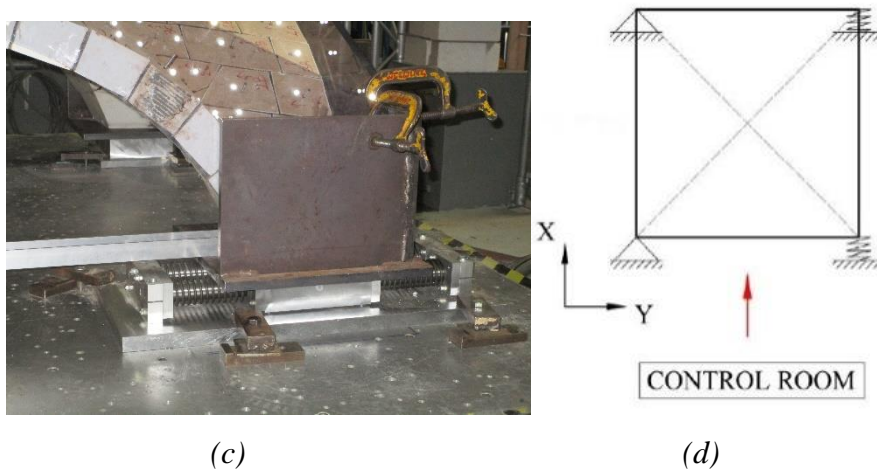


Figure 35: (c) Steel plates mounted on a moveable carriage running on bearings controlled by horizontal springing to realize two flexible springings. (d) Scheme of Configuration 2: moveable.

Four different lateral confinements were provided along the lateral arches (**Figure 36**):

- A. Four 2 cm-thick wooden panels.
- B. Four 2 cm-thick plexiglass panels.
- C. Four 2 cm-thick plexiglass panels, with two of them (the ones along the Y-direction, orthogonal to the direction of the movements allowed by the carriages) cut in the middle.
- D. No panels but only spandrel confinement.

Table 2 illustrates the properties of each tested configuration and specifies the numbers of the corresponding tests.

Configurations	Boundary condition	Lateral Confinement	Tests carried out
1A	1 fixed	A: Wooden panels	1-72
1B	1 fixed	B: Plexiglas panels	73-145, 147, 176, 196, 200
1C	1 fixed	C: Cut Plexiglas panels	205, 207, 209, 211, 213
1D	1 fixed	D: No panels	237, 239, 241, 243, 245, 247, 249, 251, 253, 255, 257, 259
2A	2 moveable	A: Wooden panels	Not tested
2B	2 moveable	B: Plexiglas panels	146, 148-175, 177-195, 197-199, 201-203
2C	2 moveable	C: Cut Plexiglas panels	204, 206, 208, 210, 212, 214-236
2D	2 moveable	D: No panels	238, 240, 242, 244, 246, 248, 250, 252, 254, 256, 258, 260-266

Table 2: Tested Configurations.

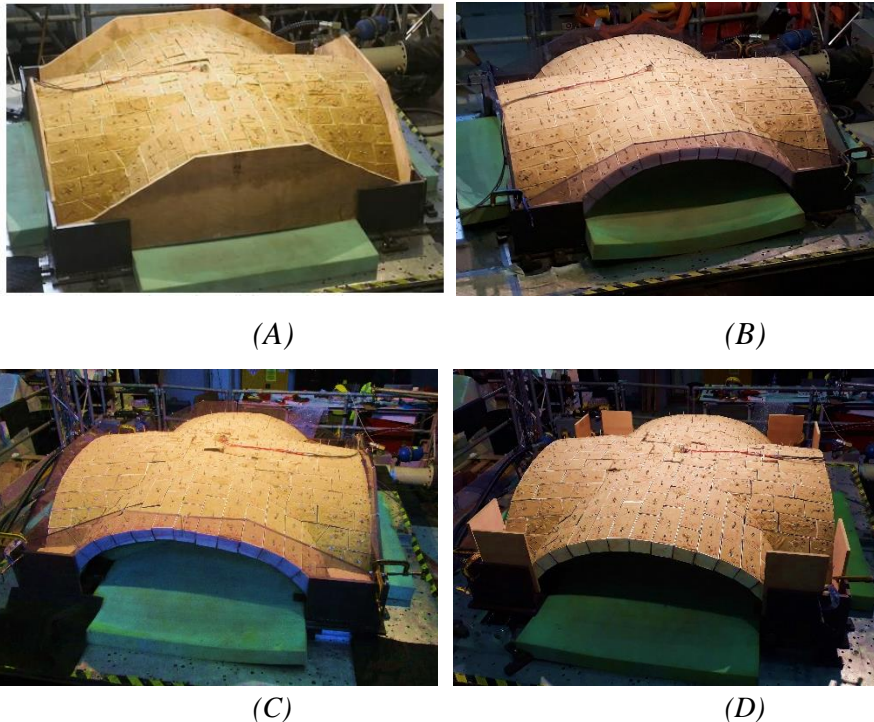


Figure 36: Confinement types: (A) wooden panels, (B) plexiglass panels, (C) cut plexiglass panels, (D) no panels.

The experimental campaign consisted of 266 tests, that were carried out in two separate sessions, August 2019 and January/February 2020:

- In the first session (tests 1 to 63), the vault was maintained in Configuration 1A and sinusoidal tests at constant amplitude with varying frequencies were explored,

with special emphasis on the X direction and on the range 2-15 Hz, where most of the damage was observed. The vault was also exposed to white noise tests, to recover the natural frequency of the vault, and to six seismic tests, without showing significant damage. After each collapse, the vault was rebuilt.

Collapse occurred three times for low frequencies:

- Test 31: $a = 1 \text{ g}$; $f = 2 \text{ Hz}$;
 - Test 52: $a = 0.95 \text{ g}$; $f = 2 \text{ Hz}$;
 - Test 63: $a = 1.4 \text{ g}$; $f = 5 \text{ Hz}$.
- In the second session (tests 64 to 266), all configurations were tested through random tests of increasing acceleration and several series of sinusoidal tests on the X direction, at constant amplitude and decreasing frequency. It turned out that collapse depended on the input frequency rather than on the input duration, for lower acceleration levels. As before, the vault was rebuilt after each collapse, that occurred in the second campaign for the following tests:
- Test 118: $a = 0.75 \text{ g}$; $f = 5 \text{ Hz}$;
 - Test 139: $a = 1.0 \text{ g}$; $f = 3 \text{ Hz}$;
 - Test 174: $a = 0.25 \text{ g}$; $f = 2 \text{ Hz}$;
 - Test 194: $a = 1.0 \text{ g}$; $f = 3 \text{ Hz}$;
 - Test 236: $a = 0.25 \text{ g}$; $f = 2 \text{ Hz}$;
 - Test 266: $a = 0.40 \text{ g}$; $f = 3 \text{ Hz}$.

The complete list of tests performed in the two campaigns is provided in **Table 3** and **Table 4**.

Test n.	Description:	PTA [g]	Direction	Input frequency
1	White noise test		x-direction	
2	White noise test		y-direction	
3	White noise test		z-direction	
4	Harmonic test	0.10g	x-direction	1 Hz
5	Harmonic test	0.10g	x-direction	5 Hz
6	Harmonic test	0.10g	x-direction	8 Hz
7	Harmonic test	0.10g	x-direction	10 Hz
8	Harmonic test	0.10g	x-direction	15 Hz
9	Harmonic test	0.10g	x-direction	20 Hz
10	Harmonic test	0.10g	x-direction	50 Hz
11	Harmonic test	0.25g	x-direction	1 Hz
12	Harmonic test	0.25g	x-direction	5 Hz
13	Harmonic test	0.25g	x-direction	8 Hz
14	Harmonic test	0.25g	x-direction	10 Hz
15	Harmonic test	0.25g	x-direction	15 Hz
16	Harmonic test	0.25g	x-direction	20 Hz
17	Harmonic test	0.25g	x-direction	50 Hz
18	Harmonic test	0.50g	x-direction	1 Hz
19	Harmonic test	0.50g	x-direction	5 Hz
20	Harmonic test	0.50g	x-direction	8 Hz
21	Harmonic test	0.50g	x-direction	10 Hz
22	Harmonic test	0.50g	x-direction	15 Hz
23	Harmonic test	0.50g	x-direction	20 Hz
24	Harmonic test	0.50g	x-direction	50 Hz
25	Harmonic test	0.75g	x-direction	2 Hz
26	Harmonic test	0.75g	x-direction	5 Hz
27	Harmonic test	0.75g	x-direction	8 Hz
28	Harmonic test	0.75g	x-direction	10 Hz
29	Harmonic test	0.75g	x-direction	15 Hz
30	Harmonic test	0.75g	x-direction	20 Hz
31	Harmonic test	1g	x-direction	2 Hz
32	White noise test		x-direction	
33	Harmonic test	0.80g	x-direction	15 Hz
34	Harmonic test	0.80g	x-direction	10 Hz
35	Harmonic test	0.80g	x-direction	8 Hz
36	Harmonic test	0.80g	x-direction	5 Hz
37	Harmonic test	0.80g	x-direction	2 Hz
38	Harmonic test	0.85g	x-direction	15 Hz
39	Harmonic test	0.85g	x-direction	10 Hz
40	Harmonic test	0.85g	x-direction	8 Hz
41	Harmonic test	0.85g	x-direction	5 Hz
42	Harmonic test	0.85g	x-direction	2 Hz
43	Harmonic test	0.90g	x-direction	15 Hz
44	Harmonic test	0.90g	x-direction	10 Hz
45	Harmonic test	0.90g	x-direction	8 Hz
46-2	Harmonic test	0.90g	x-direction	5 Hz
46	Harmonic test	0.90g	x-direction	5 Hz
47	Harmonic test	0.90g	x-direction	2 Hz
48	Harmonic test	0.95g	x-direction	15 Hz
49	Harmonic test	0.95g	x-direction	10 Hz
50	Harmonic test	0.95g	x-direction	8 Hz
51	Harmonic test	0.95g	x-direction	5 Hz
52	Harmonic test	0.95g	x-direction	2 Hz
53	White noise test		x-direction	
54	Seismic test 1		x-direction	
55	White noise test		y-direction	
56	Seismic test 2		x-direction	
57	Seismic test 3		y-direction	
58	Seismic test 4		x-direction	
59	Seismic test 5		x-direction	
60	Seismic test 6		x-direction	
61	Harmonic test	1g	y-direction	5 Hz
62	Harmonic test	1.2g	y-direction	5 Hz
63	Harmonic test	1.4g	y-direction	5 Hz

Table 3: Tests performed during the first campaign.

Test n.	Description:	PTA [g]	Direction	Input frequency	Recorded frequency
64	Random test	0.03g	x-direction	17 Hz	
65	Random test	0.03g	y-direction	17 Hz	
66	Random test	0.05g	x-direction	15 Hz	
67	Random test	0.10g	x-direction		12.4 Hz
68	Random test	0.20g	x-direction		10.4 Hz
69	Random test	0.30g	x-direction		9.5 Hz
70	Random test	0.40g	x-direction		8.8 Hz
71	Random test	0.5g	x-direction		7.7 Hz
72	Random test	0.6g	x-direction		6.9 Hz
73	Random test	0.03g	x-direction		14.95 Hz
74	Random test	0.03g	y-direction		14.84 Hz
75	Random test	0.05g	x-direction		13.57 Hz
76	Random test	0.10g	x-direction		11.58 Hz
77	Random test	0.20g	x-direction		10.13 Hz
78	Random test	0.03g	x-direction		14.8 Hz
79	Sinusoidal test-10 cycles	0.25g	x-direction	50 Hz	
80	Sinusoidal test-10 cycles	0.25g	x-direction	20 Hz	
81	Sinusoidal test-10 cycles	0.25g	x-direction	15 Hz	
82	Sinusoidal test-10 cycles	0.25g	x-direction	10 Hz	
83	Sinusoidal test-10 cycles	0.25g	x-direction	8 Hz	
84	Sinusoidal test-10 cycles	0.25g	x-direction	5 Hz	
85	Sinusoidal test-10 cycles	0.25g	x-direction	3 Hz	
86	Sinusoidal test-10 cycles	0.25g	x-direction	2 Hz	
87	Sinusoidal test-10 cycles	0.25g	x-direction	1 Hz	
88	Random test	0.03g	x-direction		14.02 Hz
89	Sinusoidal test-10 cycles	0.50g	x-direction	50 Hz	
90	Sinusoidal test-10 cycles	0.50g	x-direction	20 Hz	
91	Sinusoidal test-10 cycles	0.50g	x-direction	15 Hz	
92	Sinusoidal test-10 cycles	0.50g	x-direction	10 Hz	
93	Sinusoidal test-10 cycles	0.50g	x-direction	8 Hz	
94	Sinusoidal test-10 cycles	0.50g	x-direction	5 Hz	
95	Sinusoidal test-10 cycles	0.50g	x-direction	3 Hz	
96	Sinusoidal test-10 cycles	0.50g	x-direction	2 Hz	
97	Sinusoidal test-10 cycles	0.50g	x-direction	1 Hz	
98	Random test	0.03g	x-direction		14.5 Hz
99	Sinusoidal test-10 cycles	0.75g	x-direction	50 Hz	
100	Sinusoidal test-10 cycles	0.75g	x-direction	20 Hz	
101	Sinusoidal test-10 cycles	0.75g	x-direction	15 Hz	
102	Sinusoidal test-10 cycles	0.75g	x-direction	10 Hz	
103	Sinusoidal test-10 cycles	0.75g	x-direction	8 Hz	
104	Sinusoidal test-10 cycles	0.75g	x-direction	5 Hz	
105	Sinusoidal test-10 cycles	0.75g	x-direction	3 Hz	
106	Sinusoidal test-10 cycles	0.75g	x-direction	2 Hz	
107	Random test	0.03g	x-direction		13.83 Hz
108	Sinusoidal test-100 cycles	0.75g	x-direction	5 Hz	
109	Sinusoidal test-100 cycles	0.75g	x-direction	3 Hz	
110	Random test	0.03g	x-direction		15.16 Hz
111	Random test	0.20g	x-direction		10.5 Hz
112	Sinusoidal test-100 cycles	0.75g	x-direction	5 Hz	
113	Sinusoidal test-100 cycles	0.75g	x-direction	5 Hz	
114	Sinusoidal test-100 cycles	0.75g	x-direction	5 Hz	
115	Sinusoidal test-100 cycles	0.75g	x-direction	5 Hz	
116	Sinusoidal test-100 cycles	0.75g	x-direction	5 Hz	
117	Sinusoidal test-100 cycles	0.75g	x-direction	5 Hz	
118	Sinusoidal test-100 cycles	0.75g	x-direction	5 Hz	
119	Random test	0.03g	x-direction		14.77 Hz
120	Random test	0.03g	y-direction		14.2 Hz
121	Sinusoidal test-10 cycles	0.10g	x-direction	3 Hz	
122	Random test	0.03g	x-direction		14.9 Hz
123	Sinusoidal test-10 cycles	0.20g	x-direction	3 Hz	
124	Random test	0.03g	x-direction		14.85 Hz
125	Sinusoidal test-10 cycles	0.30g	x-direction	3 Hz	
126	Random test	0.03g	x-direction		14.87 Hz
127	Sinusoidal test-10 cycles	0.40g	x-direction	3 Hz	

128	Random test	0.03g	x-direction		14.62 Hz
129	Sinusoidal test-10 cycles	0.50g	x-direction	3 Hz	
130	Random test	0.03g	x-direction		14.4 Hz
131	Sinusoidal test-10 cycles	0.60g	x-direction	3 Hz	
132	Random test	0.03g	x-direction		14.22 Hz
133	Sinusoidal test-10 cycles	0.70g	x-direction	3 Hz	
134	Random test	0.03g	x-direction		14.23 Hz
135	Sinusoidal test-10 cycles	0.80g	x-direction	3 Hz	
136	Random test	0.03g	x-direction		13.84 Hz
137	Sinusoidal test-10 cycles	0.90g	x-direction	3 Hz	
138	Random test	0.03g	x-direction		12.63 Hz
139	Sinusoidal test-10 cycles	1.0 g	x-direction	3 Hz	
140	Random test	0.03g	x-direction		14.37 Hz
141	Random test	0.03g	y-direction		13.88 Hz
142	Sinusoidal test-10 cycles	0.90g	x-direction	3 Hz	
143	Sinusoidal test-10 cycles	1.0 g	x-direction	3 Hz	
144	Random test-Fixed Conf.	0.03g	x-direction		11.99 Hz
145	Random test-Fixed Conf.	0.03g	y-direction		13.34 Hz
146	Random test-Mov. Conf.	0.03g	x-direction		7.4 Hz
147	Random test- Mov. Conf.	0.03g	y-direction		13.29 Hz
148	Random test- Mov .Conf.	0.05g	x-direction		6.0Hz
149	Random test- Mov. Conf.	0.10g	x-direction		5.2 Hz
150	Random test- Mov. Conf.	0.15g	x-direction		4.87 Hz
151	Random test- Mov. Conf.	0.03g	x-direction		6.88 Hz
152	Sinusoidal test-10 cycles	0.10g	x-direction	50 Hz	
153	Sinusoidal test-10 cycles	0.10g	x-direction	20 Hz	
154	Sinusoidal test-10 cycles	0.10g	x-direction	15 Hz	
155	Sinusoidal test-10 cycles	0.10g	x-direction	10 Hz	
156	Sinusoidal test-10 cycles	0.10g	x-direction	8 Hz	
157	Sinusoidal test-10 cycles	0.10g	x-direction	6 Hz	
158	Sinusoidal test-10 cycles	0.10g	x-direction	5 Hz	
159	Sinusoidal test-10 cycles	0.10g	x-direction	4 Hz	
160	Sinusoidal test-10 cycles	0.10g	x-direction	3 Hz	
161	Sinusoidal test-10 cycles	0.10g	x-direction	2 Hz	
162	Sinusoidal test-10 cycles	0.10g	x-direction	1 Hz	
163	Random test	0.03g	x-direction		6.48 Hz
164	Sinusoidal test-10 cycles	0.25g	x-direction	50 Hz	
165	Sinusoidal test-10 cycles	0.25g	x-direction	20 Hz	
166	Sinusoidal test-10 cycles	0.25g	x-direction	15 Hz	
167	Sinusoidal test-10 cycles	0.25g	x-direction	10 Hz	
168	Sinusoidal test-10 cycles	0.25g	x-direction	8 Hz	
169	Sinusoidal test-10 cycles	0.25g	x-direction	6 Hz	
170	Sinusoidal test-10 cycles	0.25g	x-direction	5 Hz	
171	Sinusoidal test-10 cycles	0.25g	x-direction	4 Hz	
172	Sinusoidal test-10 cycles	0.25g	x-direction	3 Hz	
173	Sinusoidal test-10 cycles	0.25g	x-direction	2 Hz	
174	Sinusoidal test-30 cycles	0.25g	x-direction	2 Hz	
175	Random test	0.03g	x-direction		7.07 Hz
176	Random test	0.03g	y-direction		13.86 Hz
177	Sinusoidal test-10 cycles	0.05g	x-direction	3 Hz	
178	Random test	0.03g	x-direction		7.04 Hz
179	Sinusoidal test-10 cycles	0.10g	x-direction	3 Hz	
180	Random test	0.03g	x-direction		6.87 Hz
181	Sinusoidal test-10 cycles	0.15g	x-direction	3 Hz	
182	Random test	0.03g	x-direction		5.66 Hz
183	Sinusoidal test-10 cycles	0.20g	x-direction	3 Hz	
184	Random test	0.03g	x-direction		6.42 Hz
185	Sinusoidal test-10 cycles	0.25g	x-direction	3 Hz	
186	Random test	0.03g	x-direction		6.23 Hz
187	Sinusoidal test-10 cycles	0.30g	x-direction	3 Hz	
188	Sinusoidal test-10 cycles	0.35g	x-direction	3 Hz	
189	Sinusoidal test-10 cycles	0.4g	x-direction	3 Hz	
190	Sinusoidal test-10 cycles	0.45g	x-direction	3 Hz	
191	Sinusoidal test-10 cycles	0.50g	x-direction	3 Hz	
192	Sinusoidal test-10 cycles	0.60g	x-direction	3 Hz	
193	Sinusoidal test-10 cycles	0.75g	x-direction	3 Hz	
194	Sinusoidal test-100 cycles	1.0g	x-direction	3 Hz	

195	Random test	0.03g	x-direction		7.24 Hz
196	Random test	0.20g	y-direction		12.69 Hz
197	Sinusoidal test-500 cycles	0.20g	x-direction	3 Hz	
198	Sinusoidal test-500 cycles	0.20g	x-direction	3 Hz	
199	Sinusoidal test-500 cycles	0.20g	x-direction	3 Hz	
200	Sinusoidal test-500 cycles	0.20g	x-direction	3 Hz	
201	Sinusoidal test-500 cycles	0.20g	x-direction	3 Hz	
202	Sinusoidal test-500 cycles	0.20g	x-direction	3 Hz	
203	Sinusoidal test-500 cycles	0.20g	x-direction	3 Hz	
204	Random test.	0.03g	x-direction		6.3 Hz
205	Random test.	0.03g	y-direction		10.5 Hz
206	Random test.	0.05g	x-direction		5.4 Hz
207	Random test.	0.05g	y-direction		9.97 Hz
208	Random test.	0.10g	x-direction		4.75 Hz
209	Random test.	0.10g	y-direction		8.8 Hz
210	Random test.	0.15g	x-direction		3.9 Hz
211	Random test.	0.15g	y-direction		8.3 Hz
212	Random test.	0.03g	x-direction		6.47 Hz
213	Random test.	0.03g	y-direction		10.8 Hz
214	Sinusoidal test-10 cycles	0.10g	x-direction	50 Hz	
215	Sinusoidal test-10 cycles	0.10g	x-direction	20 Hz	
216	Sinusoidal test-10 cycles	0.10g	x-direction	15 Hz	
217	Sinusoidal test-10 cycles	0.10g	x-direction	10 Hz	
218	Sinusoidal test-10 cycles	0.10g	x-direction	8 Hz	
219	Sinusoidal test-10 cycles	0.10g	x-direction	6 Hz	
220	Sinusoidal test-10 cycles	0.10g	x-direction	5 Hz	
221	Sinusoidal test-10 cycles	0.10g	x-direction	4 Hz	
222	Sinusoidal test-10 cycles	0.10g	x-direction	3 Hz	
223	Sinusoidal test-10 cycles	0.10g	x-direction	2 Hz	
224	Sinusoidal test-30 cycles	0.10g	x-direction	1 Hz	
225	Random test	0.03g	x-direction		6.45 Hz
226	Sinusoidal test-10 cycles	0.25g	x-direction	50 Hz	
227	Sinusoidal test-10 cycles	0.25g	x-direction	20 Hz	
228	Sinusoidal test-10 cycles	0.25g	x-direction	15 Hz	
229	Sinusoidal test-10 cycles	0.25g	x-direction	10 Hz	
230	Sinusoidal test-10 cycles	0.25g	x-direction	8 Hz	
231	Sinusoidal test-10 cycles	0.25g	x-direction	6 Hz	
232	Sinusoidal test-10 cycles	0.25g	x-direction	5 Hz	
233	Sinusoidal test-10 cycles	0.25g	x-direction	4 Hz	
234	Sinusoidal test-10 cycles	0.25g	x-direction	3 Hz	
235	Sinusoidal test-10 cycles	0.25g	x-direction	2 Hz	
236	Sinusoidal test-30 cycles	0.25g	x-direction	2 Hz	
237	Random test.	0.03g	y-direction		9.40 Hz
238	Random test.	0.03g	x-direction		4.8 Hz
239	Random test.	0.05g	y-direction		8.7 Hz
240	Random test.	0.05g	x-direction		4.6 Hz
241	Random test.	0.10g	y-direction		7.6 Hz
242	Random test.	0.10g	x-direction		3.71 Hz
243	Random test.	0.15g	y-direction		6.65 Hz
244	Random test.	0.15g	x-direction		3.98 Hz
245	Sinusoidal test-10 cycles	0.10g	y-direction	5 Hz	
246	Sinusoidal test-10 cycles	0.10g	x-direction	5 Hz	
247	Sinusoidal test-10 cycles	0.10g	y-direction	3 Hz	
248	Sinusoidal test-10 cycles	0.10g	x-direction	3 Hz	
249	Sinusoidal test-10 cycles	0.10g	y-direction	2 Hz	
250	Sinusoidal test-10 cycles	0.10g	x-direction	2 Hz	
251	Random test	0.03g	y-direction		10.12 Hz
252	Random test	0.03g	x-direction		5.27 Hz
253	Sinusoidal test-10 cycles	0.05g	y-direction	3 Hz	
254	Sinusoidal test-10 cycles	0.05g	x-direction	3 Hz	
255	Random test	0.03g	y-direction		10.16 Hz
256	Random test	0.03g	x-direction		5.4 Hz
257	Sinusoidal test-10 cycles	0.10g	y-direction	3 Hz	
258	Sinusoidal test-10 cycles	0.10g	x-direction	3 Hz	
259	Random test	0.03g	y-direction		9.78 Hz

260	Random test	0.03g	x-direction		5.6 Hz
261	Sinusoidal test-10 cycles	0.15g	x-direction	3 Hz	
262	Sinusoidal test-10 cycles	0.20g	x-direction	3 Hz	
263	Sinusoidal test-10 cycles	0.25g	x-direction	3 Hz	
264	Sinusoidal test-10 cycles	0.30g	x-direction	3 Hz	
265	Sinusoidal test-10 cycles	0.35g	x-direction	3 Hz	
266	Sinusoidal test-10 cycles	0.40g	x-direction	3 Hz	

Table 4: Tests performed during the second campaign.

3. Objectives and methodology

The main objective of the project is to evaluate the crack patterns and the collapse mechanism of groin vaults with two base boundary conditions: on four walls (fixed) and on two columns and a wall (moveable). This is a key issue to plan and take correct strengthening interventions.

Two measuring systems were used to get accelerations and displacements:

1. Fridge System, composed by triaxial Setra accelerometers situated on the shaking table and the keystone of the vault, at a frequency rate of 5000 Hz (**Figure 37**).

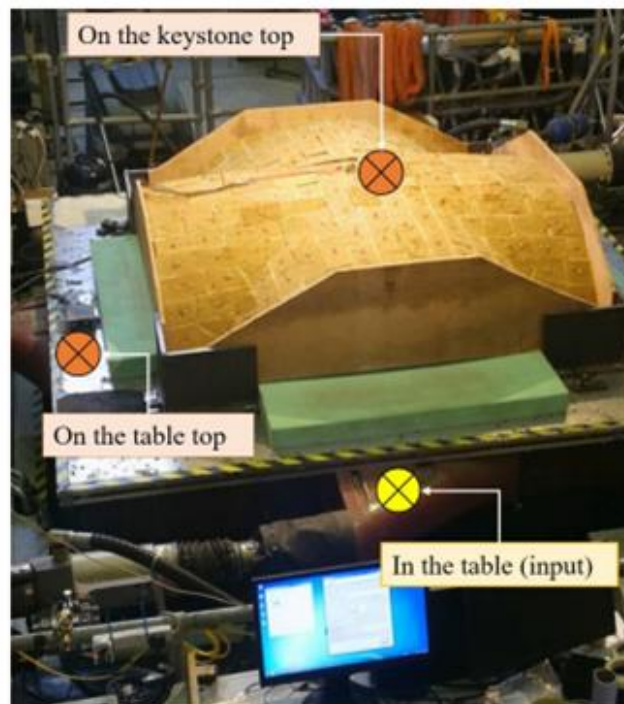
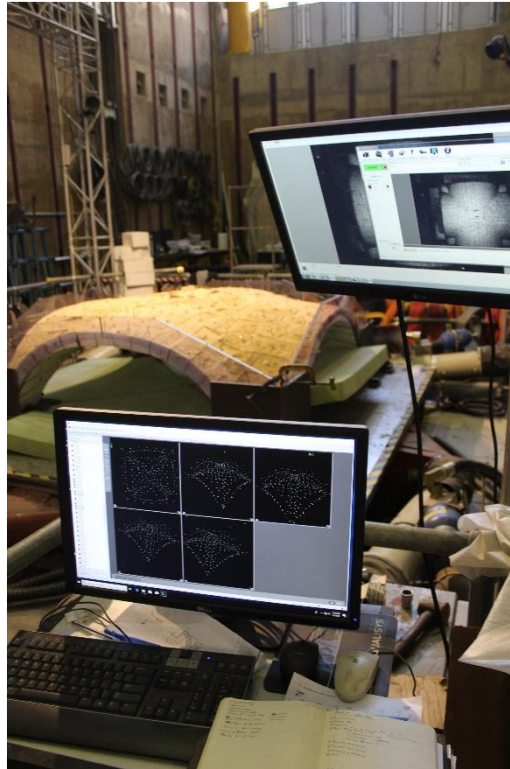


Figure 37: Position of the triaxial accelerometers.

2. Vision Data, consisting of motion capture cameras that record the position over time of reflective markers placed on each block, on the panels and on the shaking table, at a frequency rate of 100 Hz (**Figure 38**).



(a)



(b)



(c)

Figure 38: Data capture system: (a) point cloud of markers position, (b) light-reflecting markers, (c) capture camera.

An example of data recording classification, concerning the second campaign, is displayed in **Figure 39**.

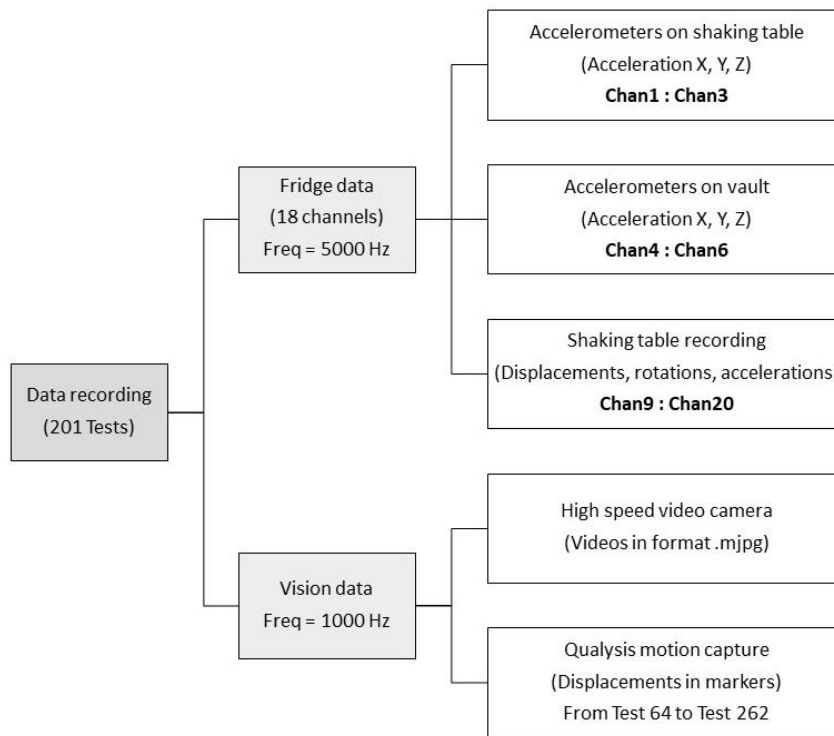


Figure 39: Data recording classification for the second campaign.

The data related to accelerations and displacements were stored in a Matlab file to be processed. To obtain the most approximate initial position of each marker, it was necessary to “clean” the vision data. This procedure follows some steps, given below.

3.1 Selection of the reference system

The first point is the determination of a unique reference system. The origin is chosen among the markers attached on the steel plates (“Springing”) and on the shaking table (“Table”), whose labels indicate the respective name in the layout:

- Springing.SE (SE), Springing.SW (SW), Springing.NE (NE), Springing.NW (NW) for the steel corners;
- Table.E (STE) and Table.W (STW) for the shaking table.

Figure 40 shows the location of the six considered markers and **Figure 41** displays them into the layout of all the markers.

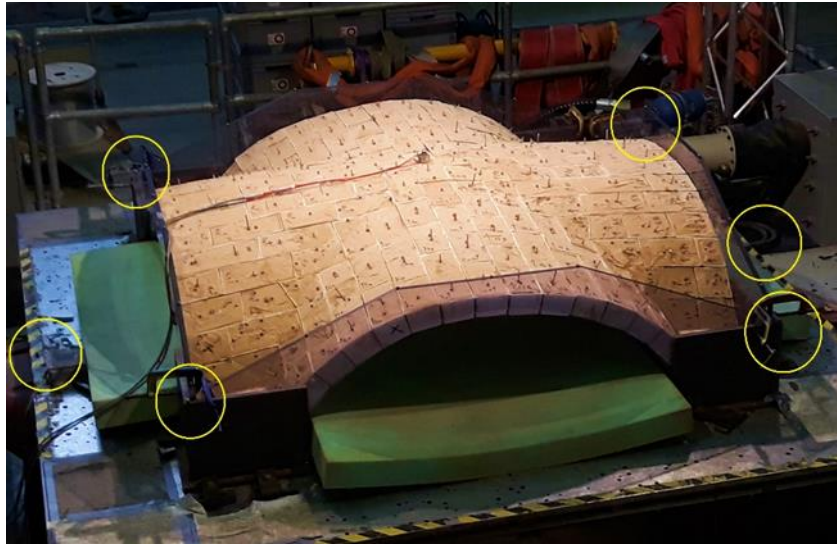


Figure 40: Location of the markers on the steel plates and on the shaking table.

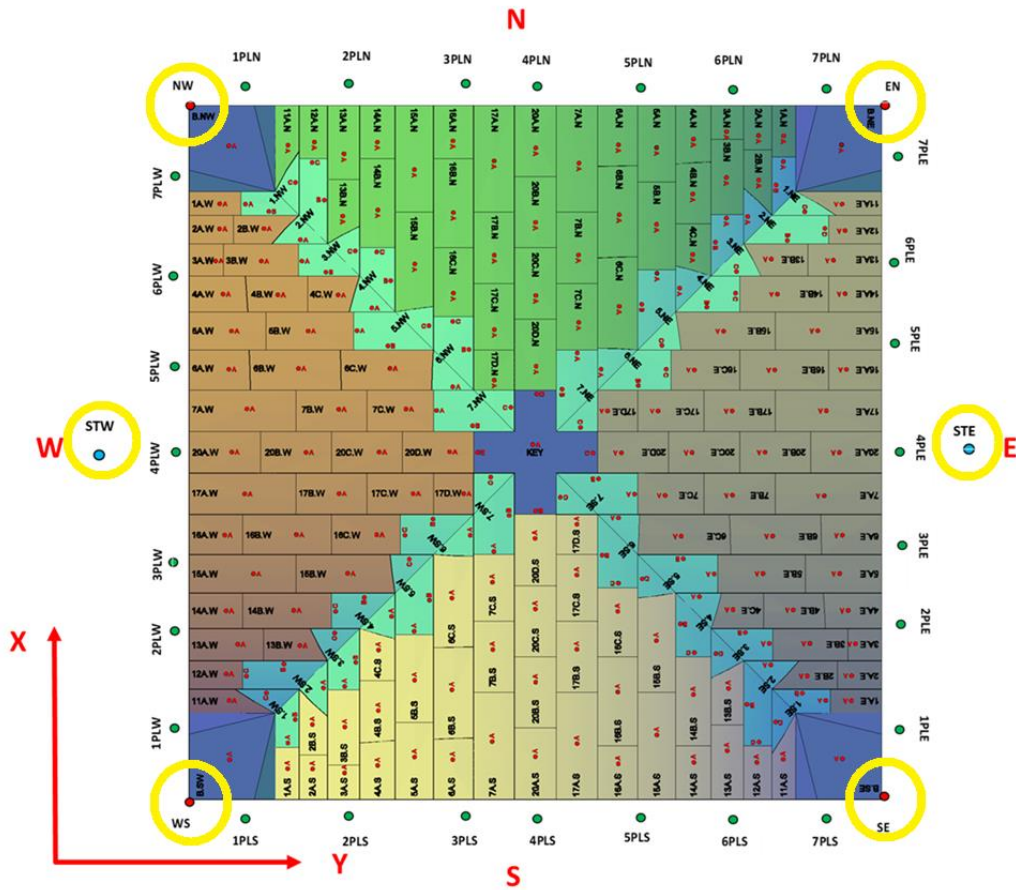


Figure 41: Markers layout.

The displacement time history of the markers for a given test is reported in Figure 42: as regards the fixed configuration (test 85), the trend of the six markers results to be very

similar, so it is possible to choose any of them as origin. Differently, in the moveable configuration (test 172), the markers placed on the translating steel corners (Springing.SE and Springing.NE) show greater displacement than the others and cannot represent a suitable reference point. Therefore, the selected marker as origin is Table.E (STE).

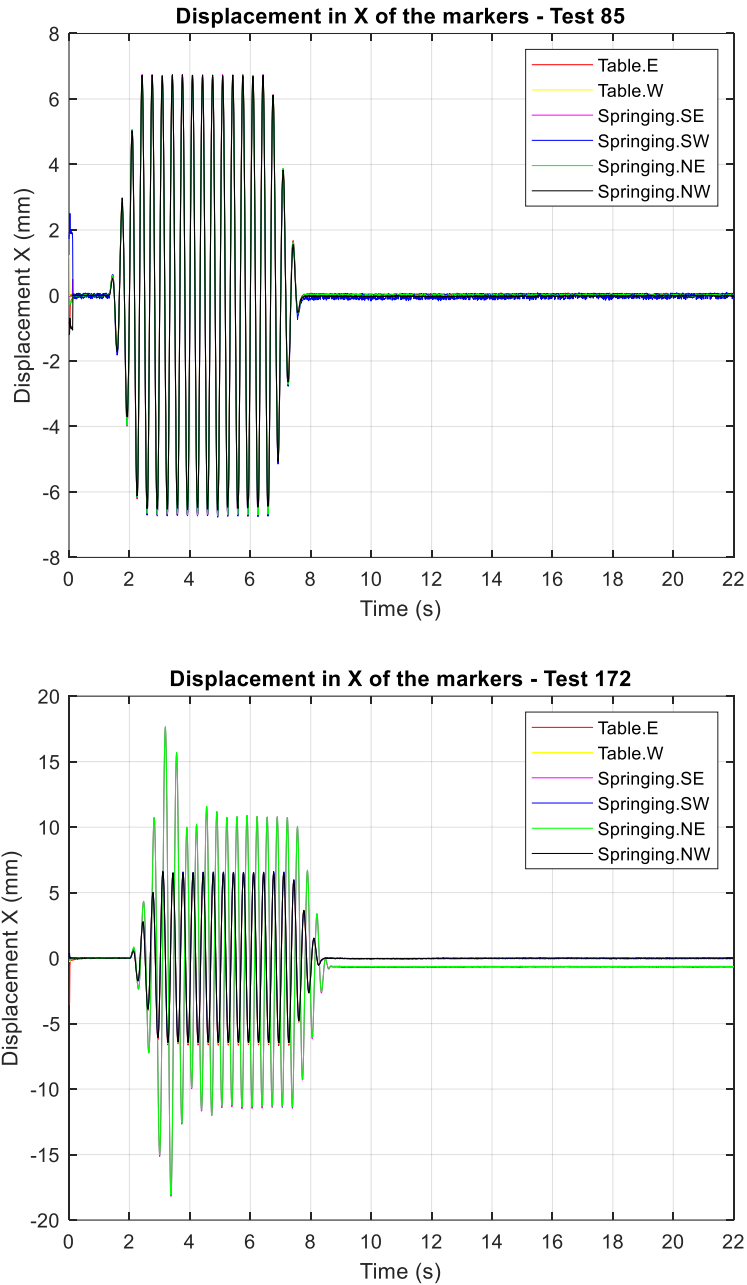


Figure 42: Comparison among markers on steel plates and shaking table, for tests 85 and 172.

3.2 Initial time of the input signal

A one-second window was selected manually before each test input signal, relative to the Table.E (STE) marker, in order to clean the window to get the most approximate initial configuration of the vault (**Figure 43**).

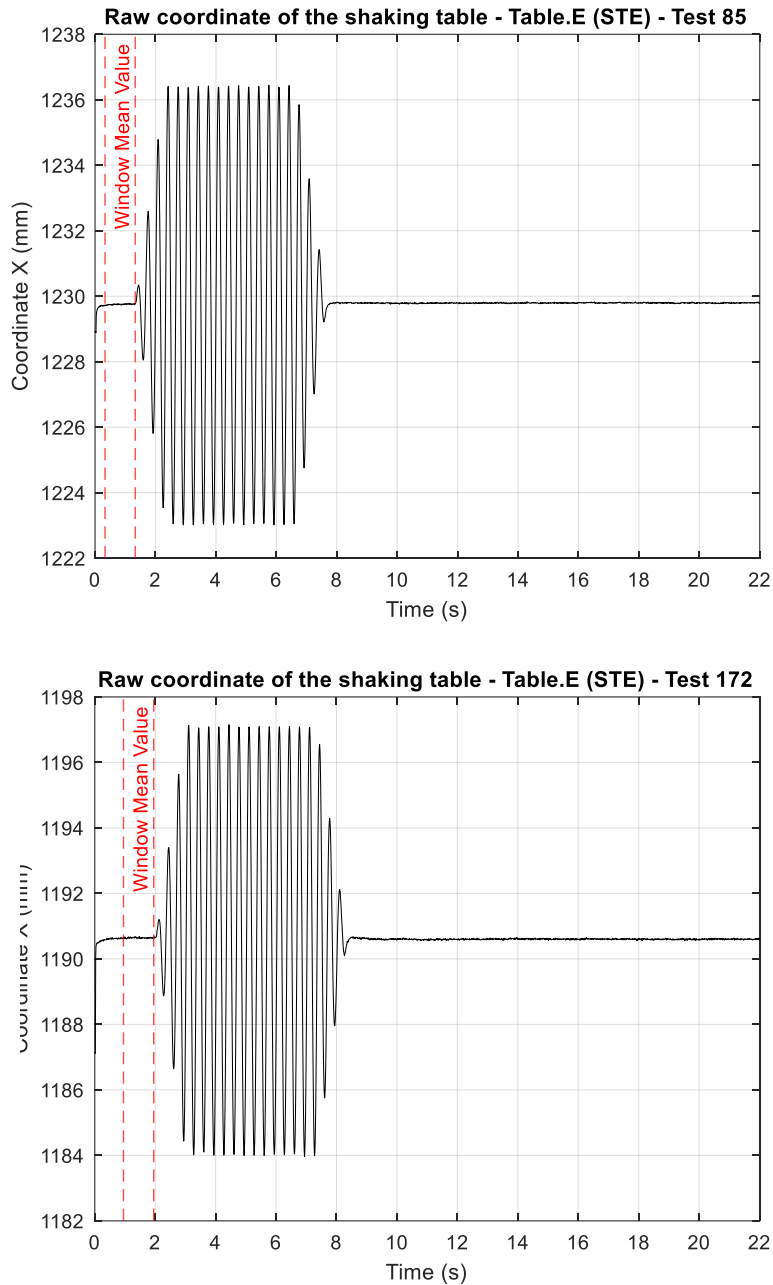


Figure 43: One-second window before the input signal, for tests 85 and 172.

3.3 Cleaning of the initial window

To remove the spikes, the mean value of the initial window is calculated; then values are selected in the range of $\pm 0.01\%$ of the first mean value. Based on this selection, the mean value is calculated again, by obtaining the initial position of the marker.

The cleaning procedure is shown in **Figure 44**. The remaining part of signal at the beginning is discarded to ensure the exact initial position.

The process to obtain and classify the different displacements is summarized in **Table 5**, including the cleaning of the initial data. An example of this procedure is then proposed in **Figures 45-48**, relative to the displacements of the keystone with respect to the chosen origin.

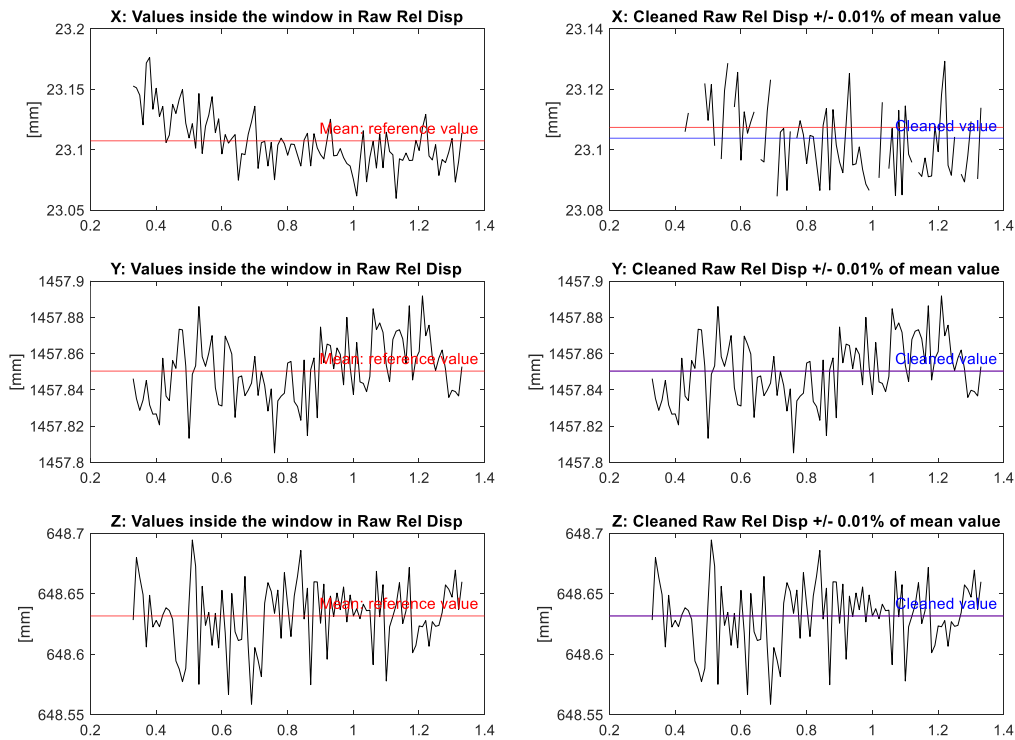


Figure 44: Cleaning of the one-second window in x, y and z directions, for test 85.

Step	Displacement	Description
1.	RAW ABSOLUTE DISPLACEMENT	Position of markers in terms of coordinates linked to an arbitrary global reference system. Original data stored in “Trajectories”.
2.	RAW RELATIVE DISPLACEMENT	Relative displacement of each marker with respect to the table, obtained through: Raw data – Raw data STE
3.	CLEANED RELATIVE DISPLACEMENT	<p>The signals have perturbations at the beginning, so it is necessary to purge the data before the input to get the most approximate initial configuration.</p> <p><u>Procedure to clean the initial part of the Raw relative displacement:</u></p> <ul style="list-style-type: none"> • The time just before the input is fixed manually for each test (t_0), then a 1-second window can be defined as in the next figure: <div style="text-align: center;"> <p style="text-align: center;">t_{-1} t_0</p> </div> <ul style="list-style-type: none"> • The mean of the window is calculated. • Spikes (atypical values with respect to the mean) are removed from the window. • The mean is calculated again, and it becomes the initial configuration before the input. <p>The raw relative displacement is reset to a series that starts at time t_{-1}. Raw relative displacement(t_{-1} : end), with a cleaned start.</p>
4.	LOCAL DISPLACEMENT	Displacement of each marker with reference to their own local reference system (first coordinate of the marker). Raw relative displacement(1:end) – Raw relative displacement(1)

Table 5: Steps for cleaning the data.

The tests in question are test 85, which is far from collapse for the fixed configuration, and test 173 for the moveable configuration, in which a partial collapse occurs and can be assumed by the shorter time interval in the displacement plots.

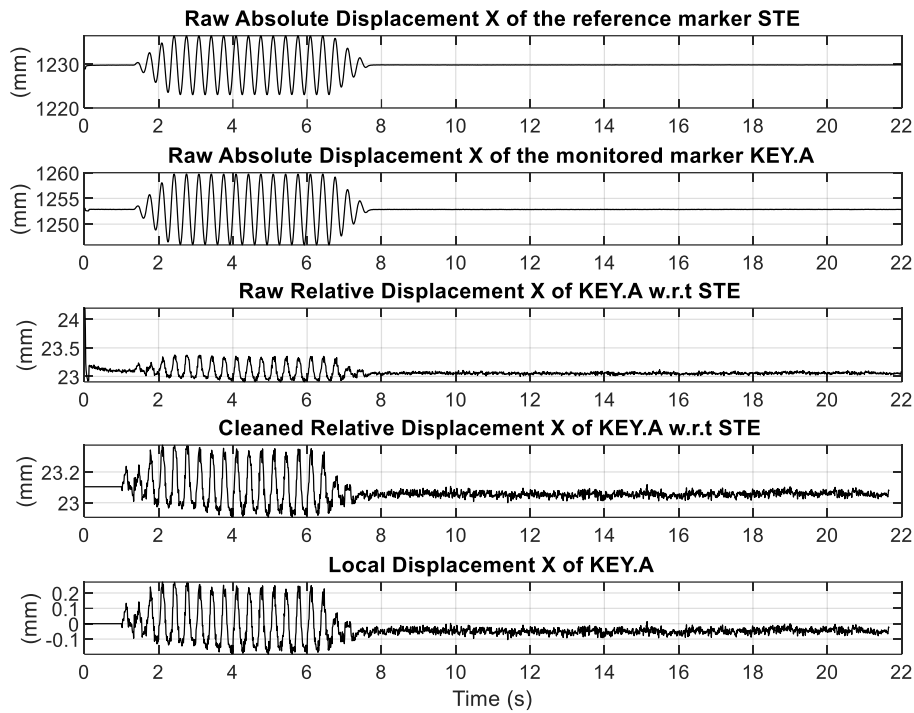


Figure 45: X displacement of the keystone, test 85.

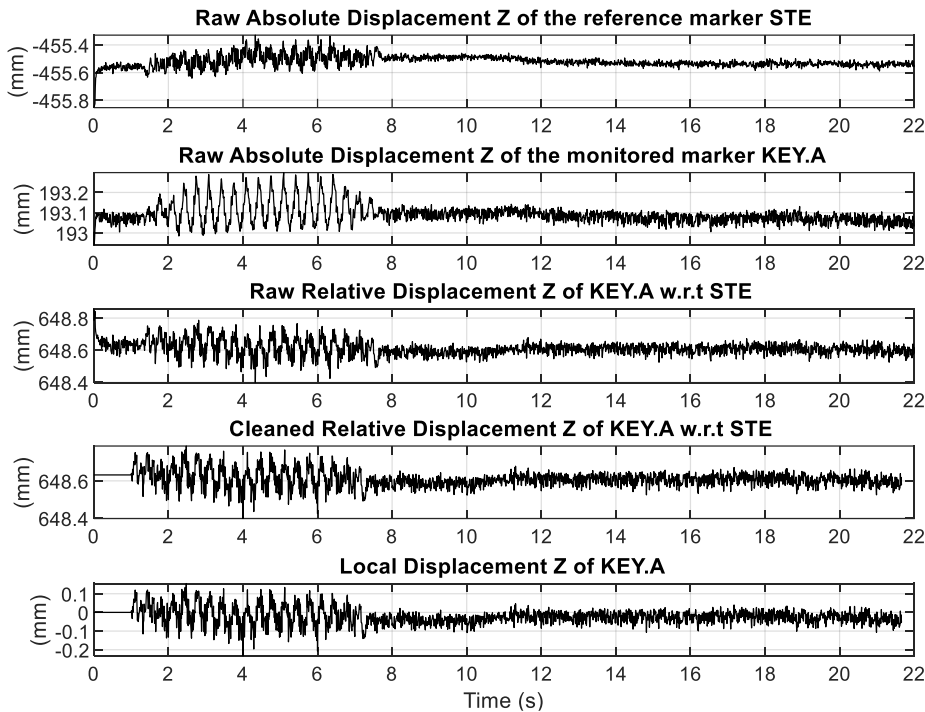


Figure 46: Z displacement of the keystone, test 85.

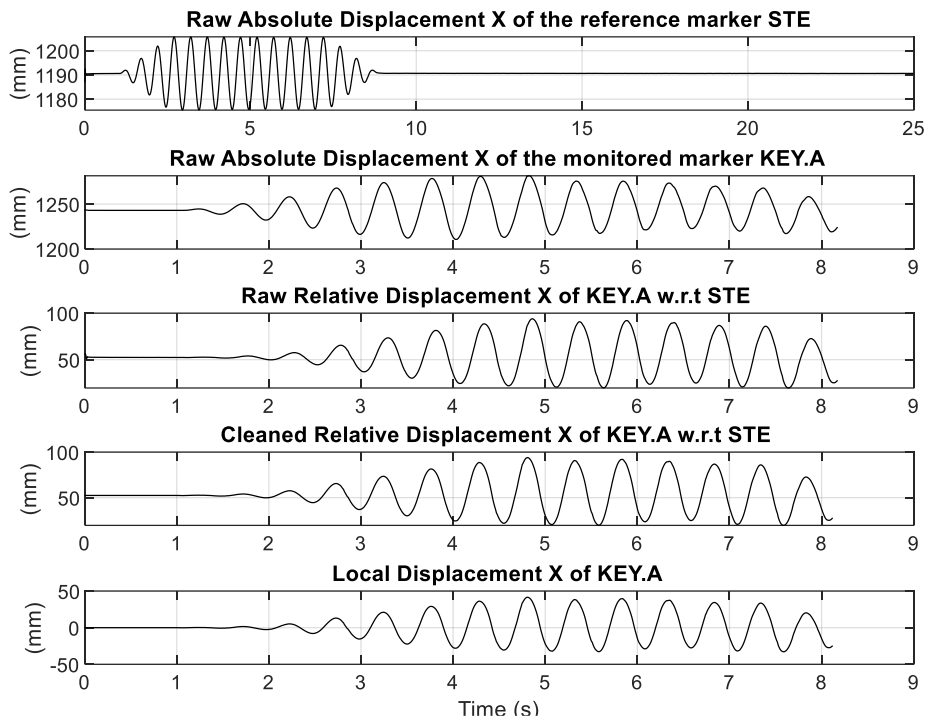


Figure 47: X displacement of the keystone, test 173.

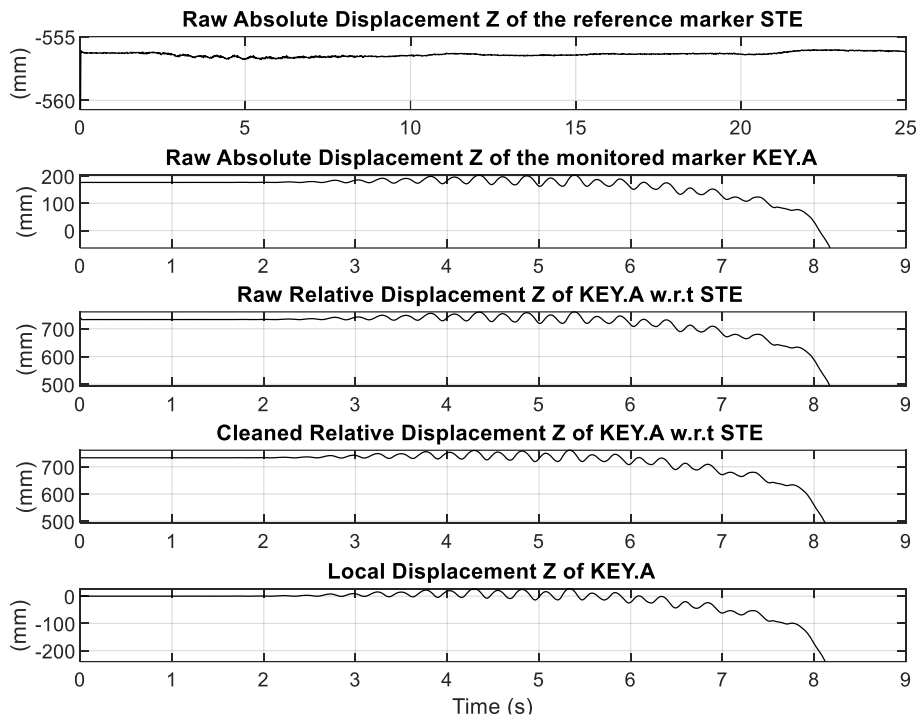


Figure 48: Z displacement of the keystone, test 173.

4. Collapse mechanisms

The objective of this section is to compare in a qualitative way the deformed shapes of the main arches of the vault (laterals and diagonals arches) for the configurations of concern, and to investigate their evolution up to the collapse mechanism. For this purpose, a Matlab script has been written to process the data referred to the displacements of the markers during the entire test duration. The resulting plot of the script is a dynamic plot, in which five different lines are visible:

- the grey curve represents the initial shape of the arch as it is rebuilt after the collapse;
- the dotted red line represents the deformed shape at the moment of collapse;
- the dotted black line stands for the deformed shape just before the collapse;
- the blue curve is the maximum deformed shape of the arch, which corresponds to the configuration in which the largest positive displacement of the top brick of the arch is observed (in the direction of interest, that is always the one on the vertical axis of the plot);
- the cyan curve is the minimum deformed shape of the arch, which corresponds to the largest negative displacement, in the direction of concern, of the top brick of the relative arch.

The values of the largest displacements of the top brick of the arch in question are plotted, where relevant. **Figure 49** displays the groin vault and the scheme adopted to better understand the resulting plots.

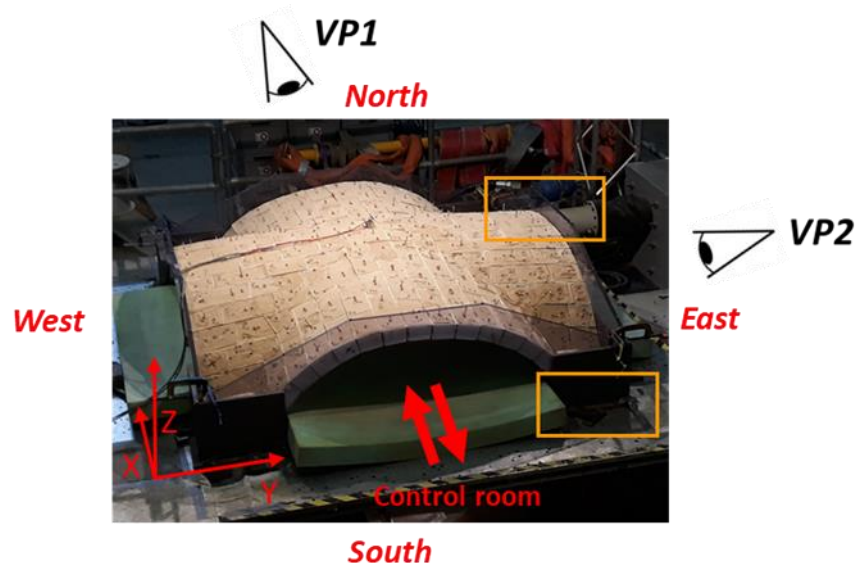


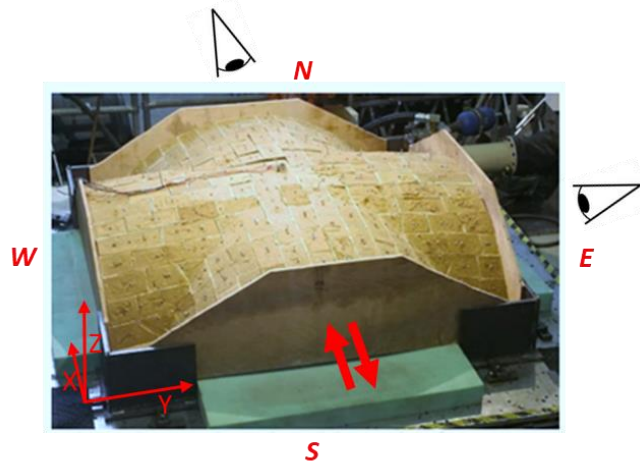
Figure 49: Groin vault layout and viewpoints.

The vault picture highlights in red the arches and the reference system. The double red arrow refers to the direction in the x axes of the shaking table motion. The springs location is evidenced by two orange squares. Two are the viewpoints VP1 and VP2 by which the corresponding plots in XY, YZ, XZ planes should be examined. The analysis involves collapse tests for Configurations 1A, 1B, 2B and 2D.

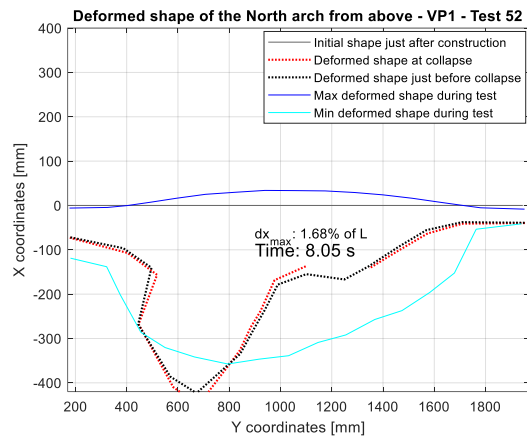
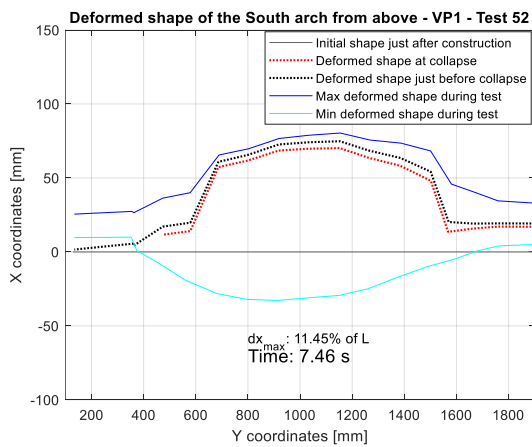
4.1 Comparison among configurations

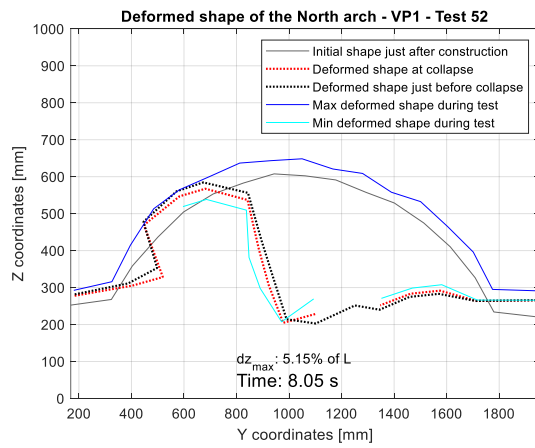
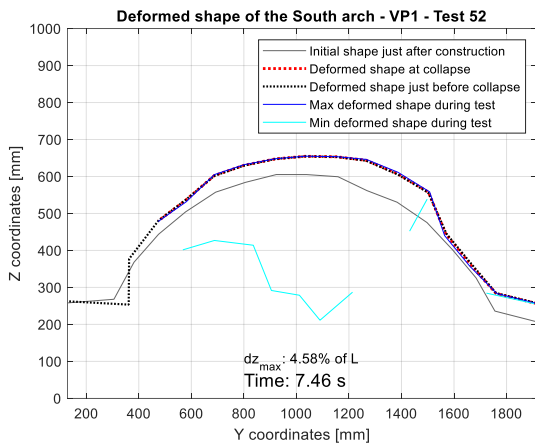
Configuration 1A: Test 52 at $f=2$ Hz and $PTA=0.95$ g

The deformed shapes for the main arches in the planes of concern are shown below.

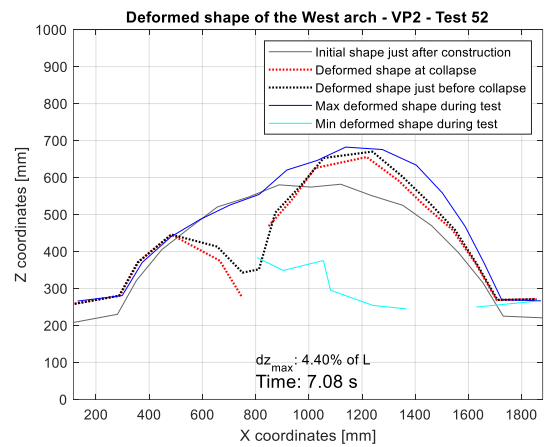
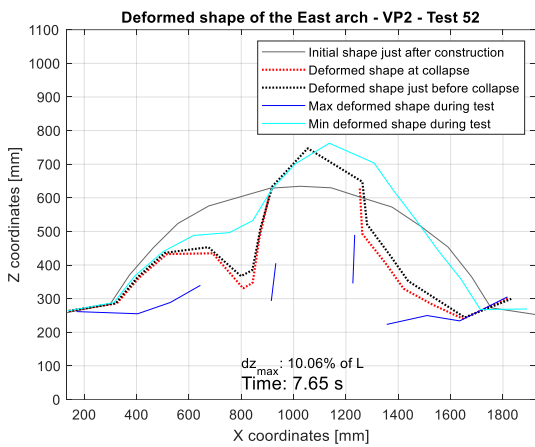
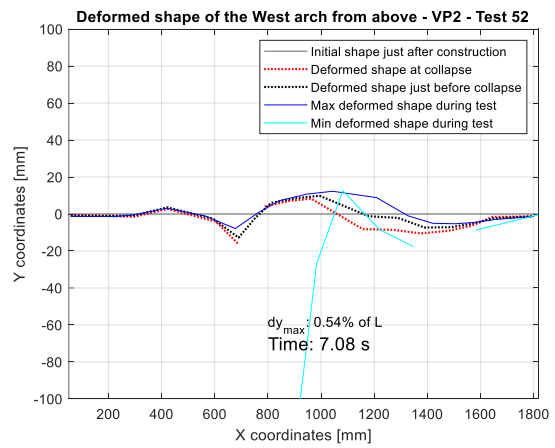
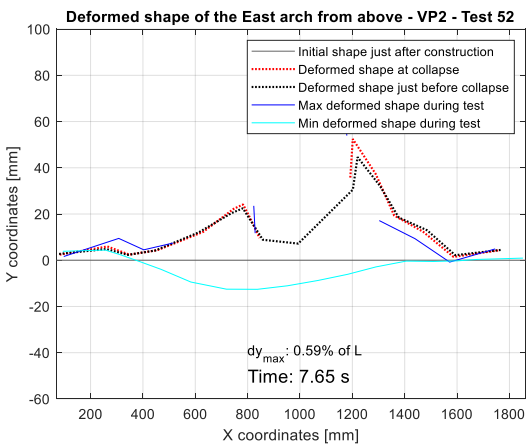


South and North arches in YX and YZ planes

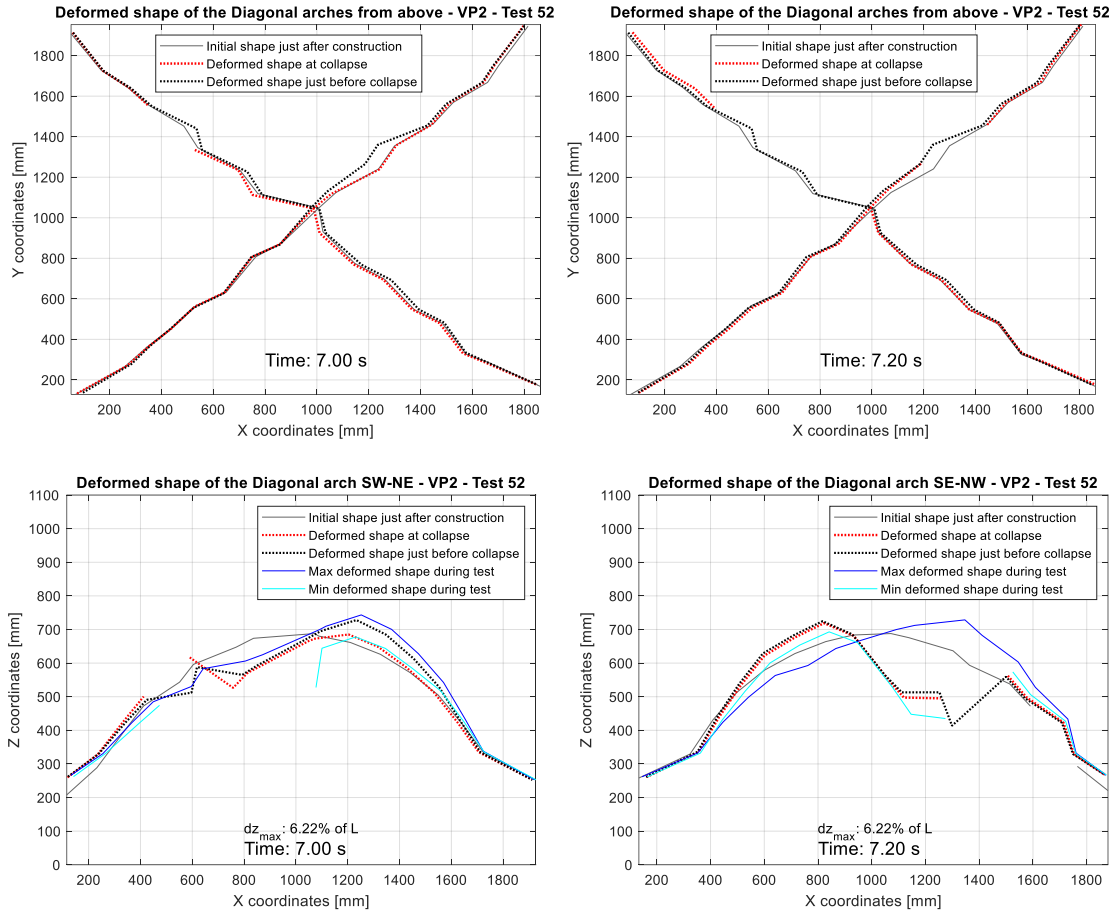




East and West arches in XY and XZ planes.



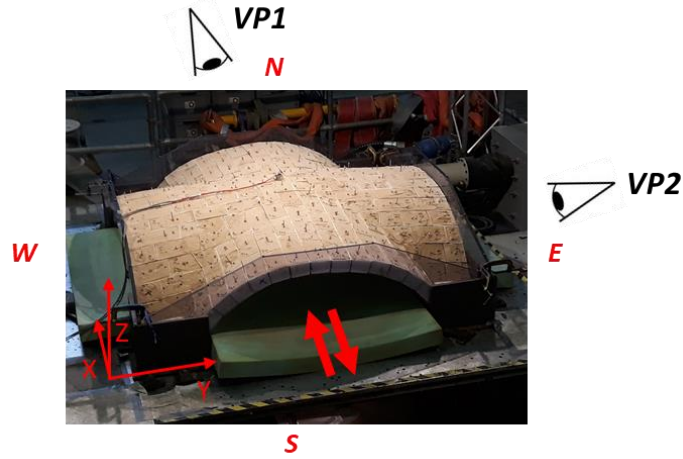
Southeast-Northwest (SE-NW) and Southwest-Northeast (SW-NE) arches in XY and XZ planes.



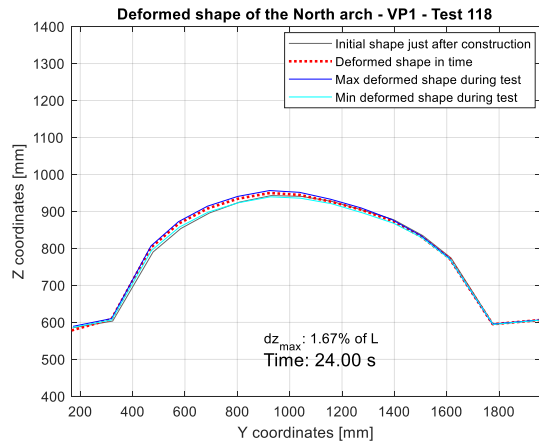
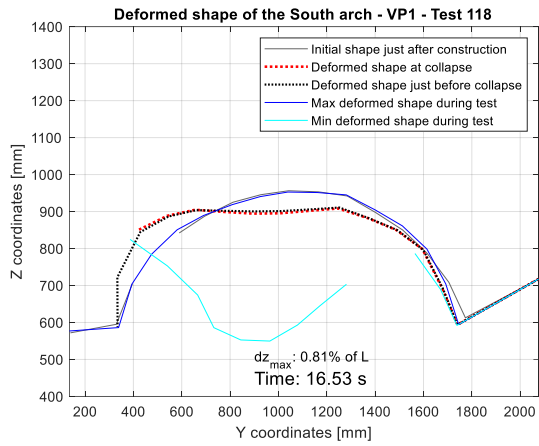
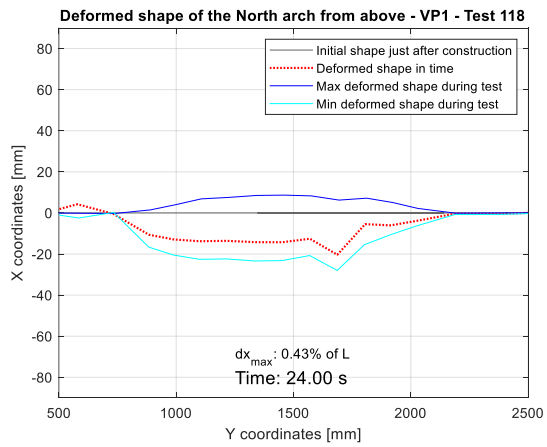
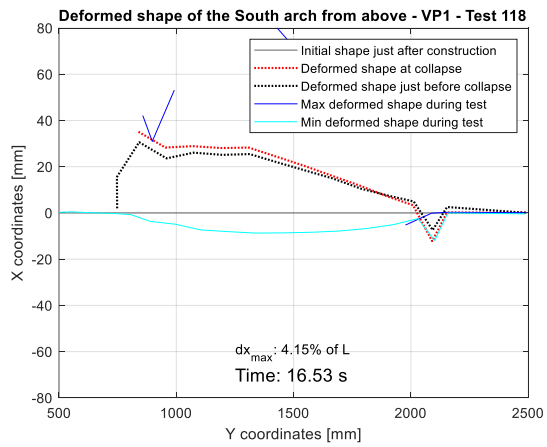
Collapse occurs almost at the same time (between 7 and 8 seconds) for all the arches, starting from the central-west portion. From the diagonal plots, it results that the most vulnerable regions, where the first detachment occurs, are the Northwest and the Southwest webs.

Configuration 1B: Test 118 at $f=5$ Hz and $PTA=0.75$ g

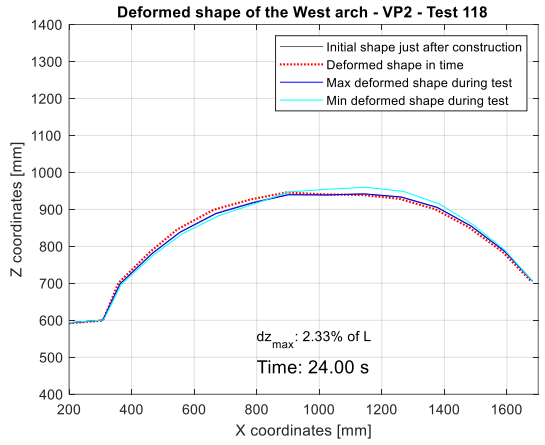
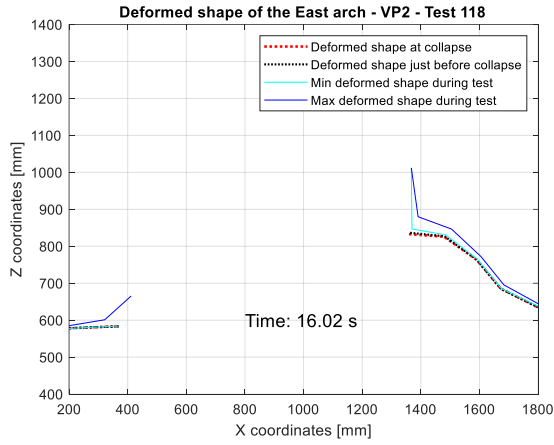
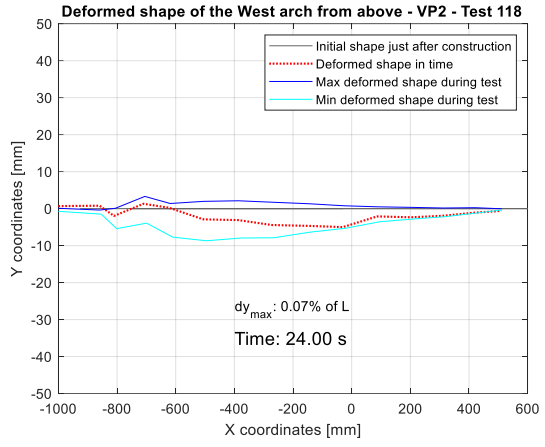
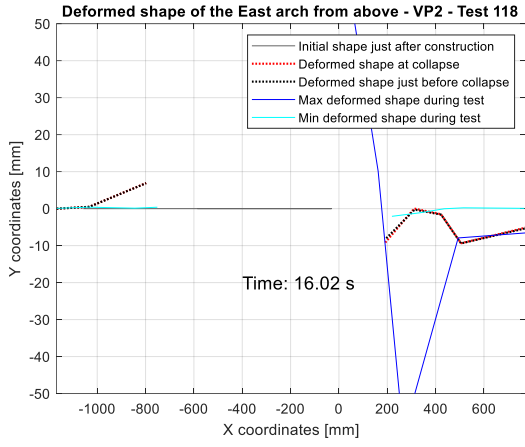
The deformed shapes for the main arches in the planes of concern are shown below.



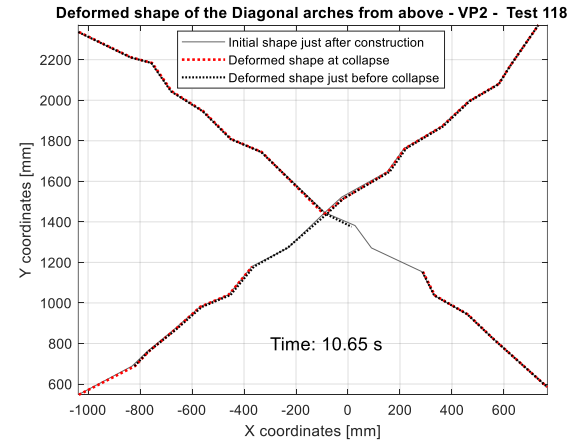
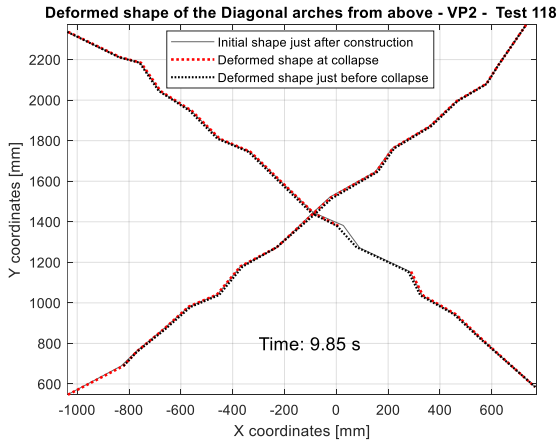
South and North arches in YX and YZ planes.

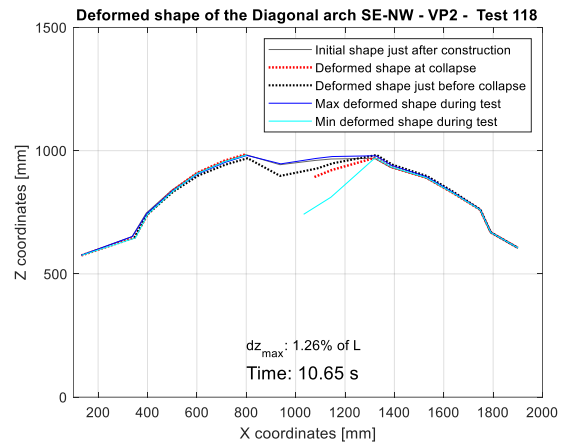
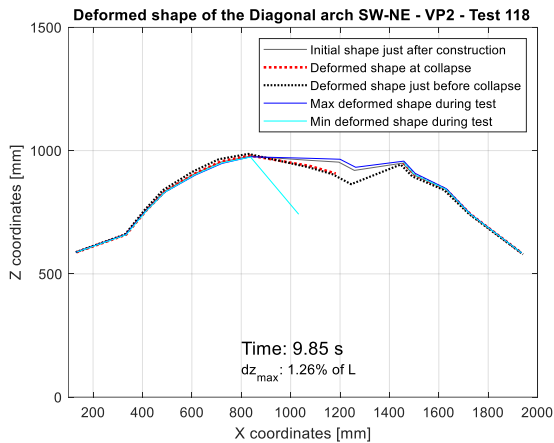


East and West arches in XY and XZ planes.



Southeast-Northwest (SE-NW) and Southwest-Northeast (SW-NE) arches in XY and XZ planes.

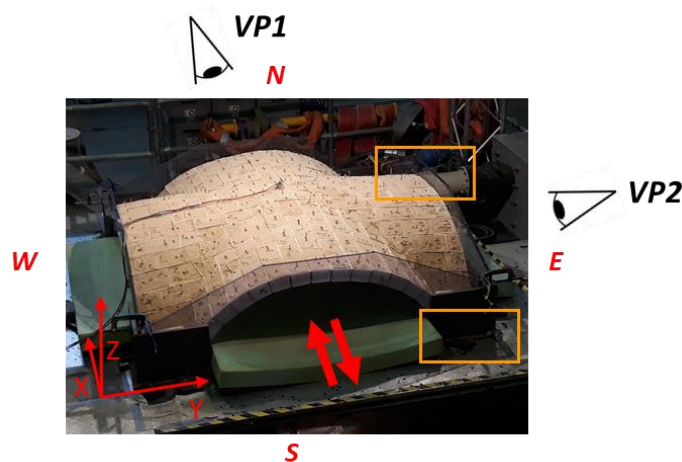




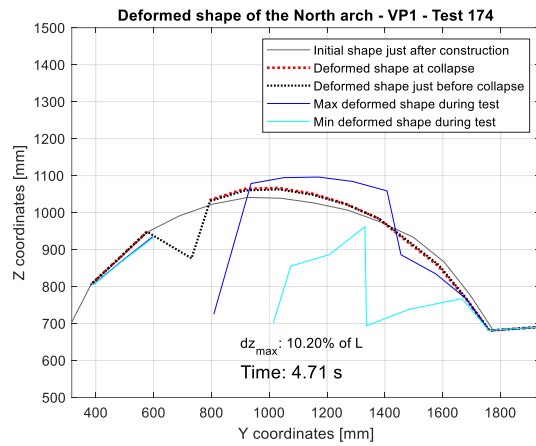
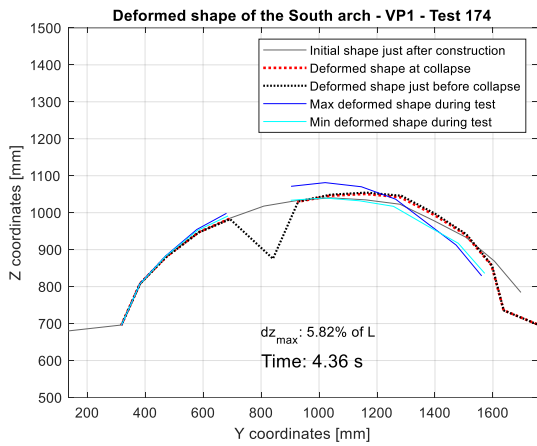
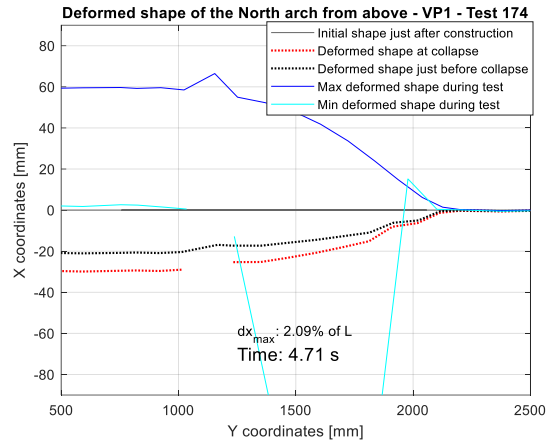
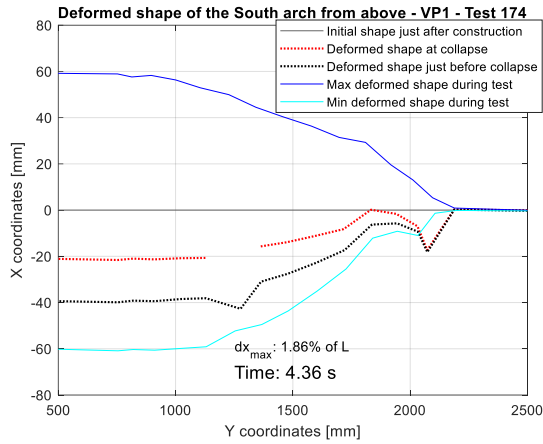
Here, failure does not involve the entire vault. Indeed, the North and West arches are the only ones to remain undamaged at the end of the test. The collapse starts in the central eastern region of the diagonals (around 10 seconds) and then spreads to the South and East arches, that definitely start to fail at the same time.

Configuration 2B: Test 174 at $f=2$ Hz and $PTA=0.25$ g

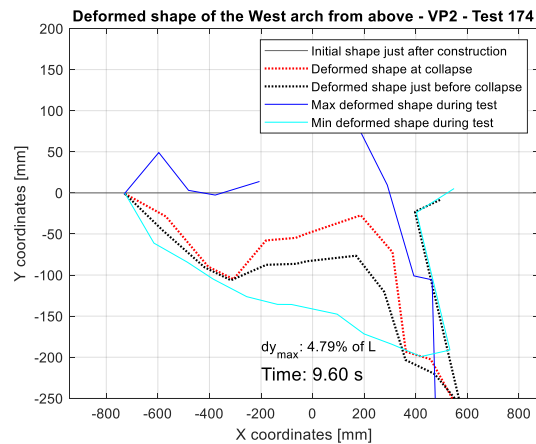
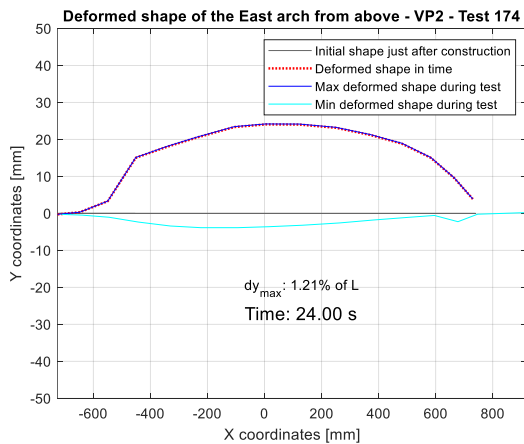
The deformed shapes for the main arches in the planes of concern are shown below.

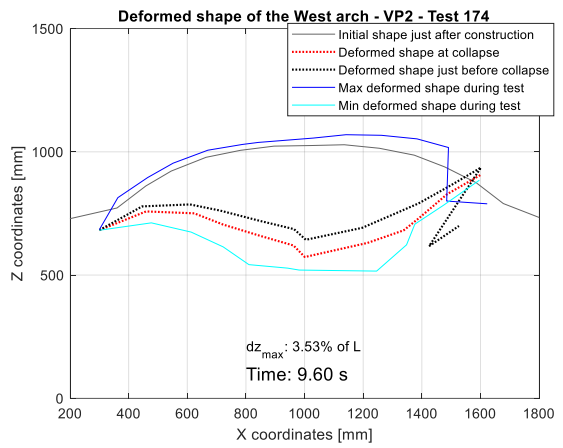
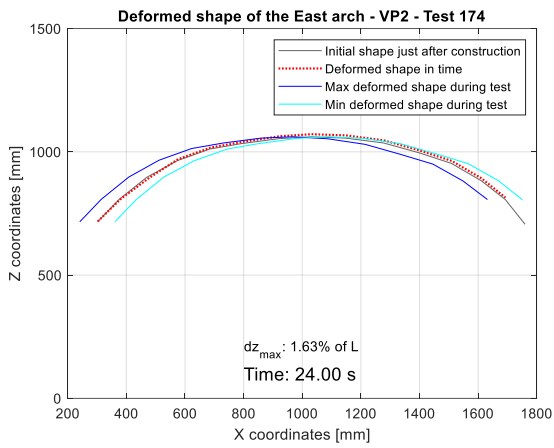


South and North arches in YX and YZ planes.

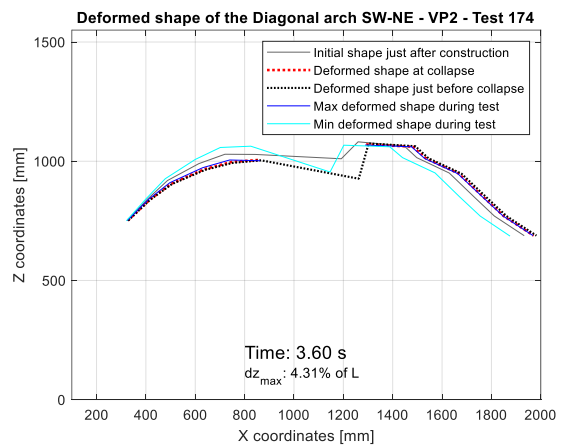
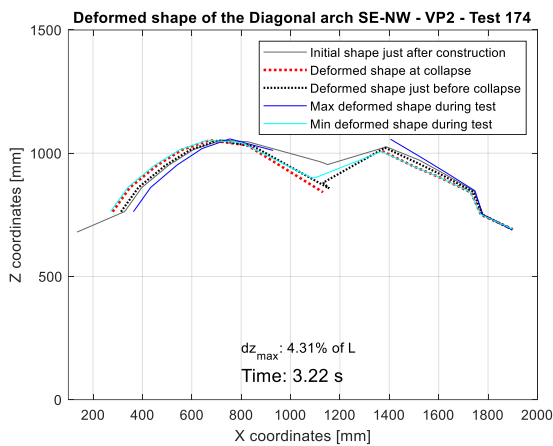
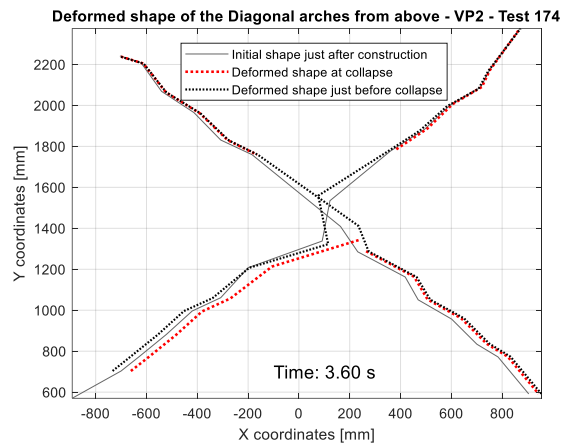
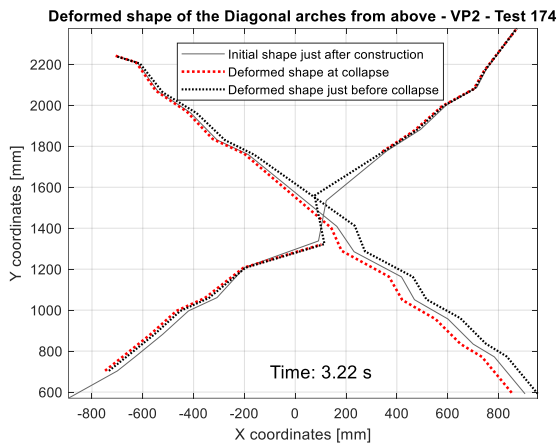


East and West arches in XY and XZ planes.





Southeast-Northwest (SE-NW) and Southwest-Northeast (SW-NE) arches in XY and XZ planes.

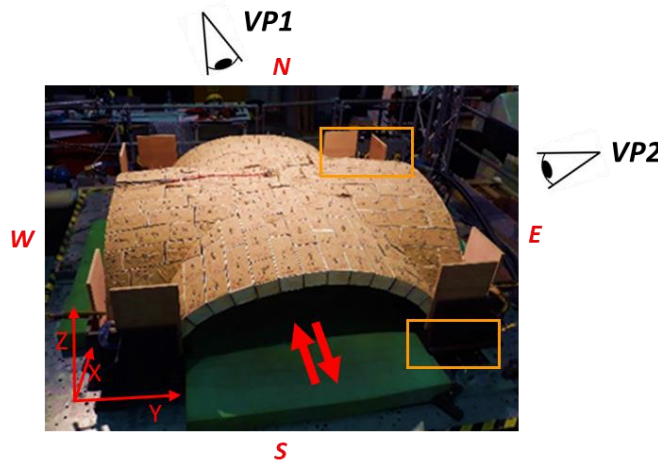


The collapse for this configuration takes place soon, by beginning from the central area at the same moment for both diagonals (around 3 seconds), then involving the South and North arch (around 4 seconds) and the West arch (10 seconds).

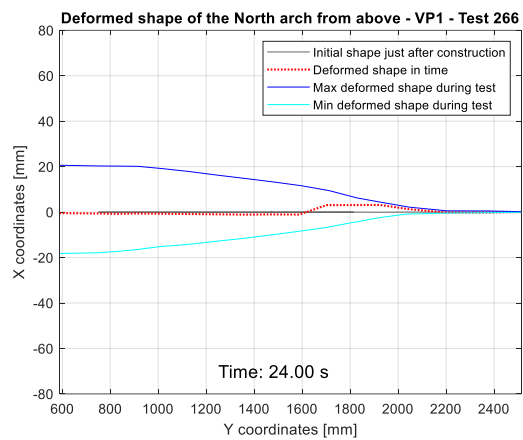
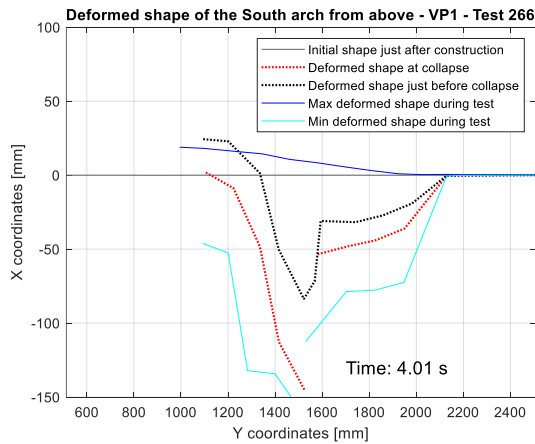
At the end of the test, the South arch is still pretty much intact, and the East arch, which just bends of 2 cm towards the center, is entirely safe.

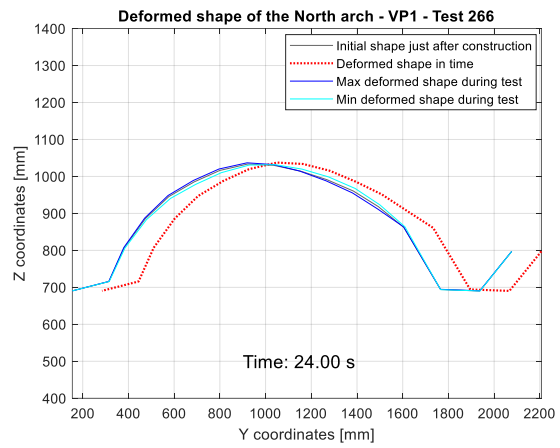
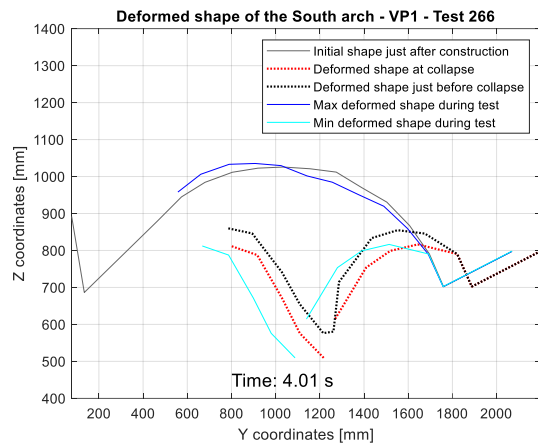
Test 266: $f=3$ Hz; PTA=0.40 g; Configuration 2D

The deformed shapes for the main arches in the planes of concern are shown below.

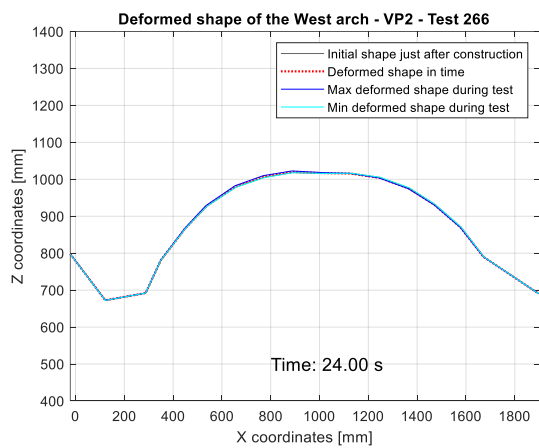
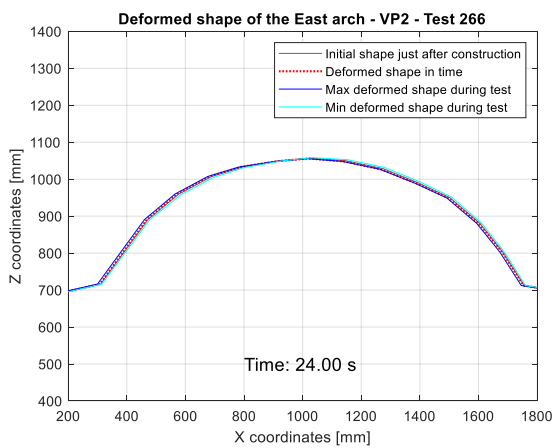
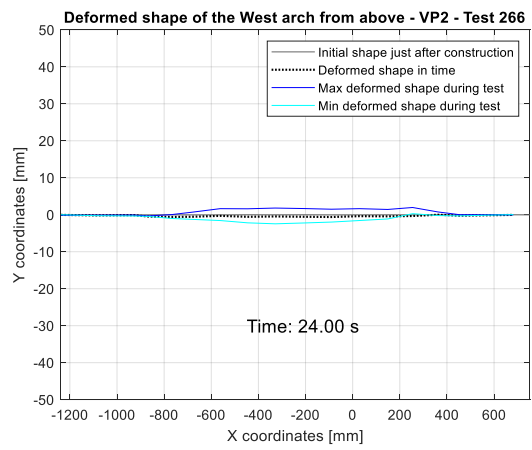
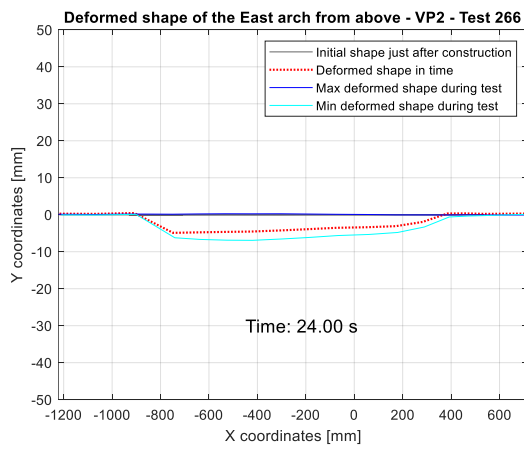


South and North arches in YX and YZ planes.

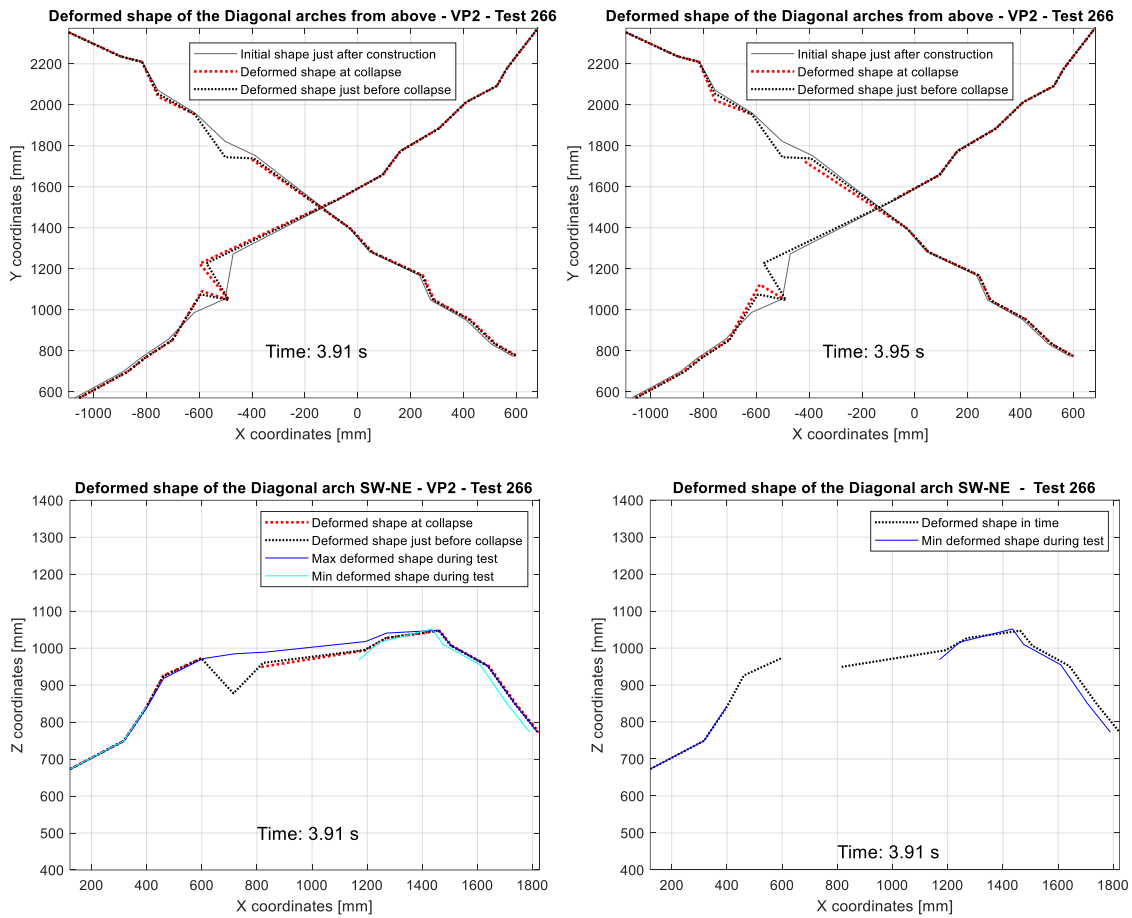




East and West arches in XY and XZ planes.



Southeast-Northwest (SE-NW) and Southwest-Northeast (SW-NE) arches in XY and XZ planes.



In this case, the failure is localized. It starts from the central portion (around 4 seconds) simultaneously for the diagonal arches and affecting the South arch, too. The remaining arches result undamaged in the end.

To sum up, a first comparison regards the two base boundary conditions, namely the fixed and moveable settings. As already tested in previous studies, it is clear that the moveable condition leads to greater displacements and to a faster instability than the fixed one. As a matter of fact, test 52, on fixed base, goes to collapse for a greater Peak Table Acceleration than test 174 on moveable base and supported by plexiglass panels, for the same Frequency value.

However, what catches the attention is the collapse mechanism for the various configurations, where failure can be monitored by the stepwise missing segments in the deformed-shape lines.

In this regard, collapse begins from the central part for each configuration, as expected. Generally, in the fixed configurations, the “opposite” arches seem to behave in a quite symmetrical way just before collapse. According to previous research, this fact can be explained by the formation of a failure line, which corresponds to the development of a cylindrical hinge in the upper central part of the vault, orthogonal to the input direction.

Instead, as regards the moveable configurations, a simultaneous collapse of the central portions of both diagonals can be noticed. This fact suggests that the failure is mainly due to the elongation and respective shortening of the two diagonal arches, caused by the imposed shear displacements.

5. Collapse displacements

The two different collapse behaviors, previously identified, require a quantitative analysis to define the orders of magnitude and to better understand the mechanisms.

5.1 Dynamic properties of the vault

To define the dynamic properties of the vault, white noise tests are carried out. These tests permit to check, after each reconstruction, the equivalence with the previous configuration, in terms of fundamental frequency and damping ratio.

The relationship between the fundamental frequency and the Root Mean Square (RMS) is highlighted in **Figure 50** for all the configurations. It can be observed that the fundamental frequency decreases as acceleration increases. Turning from Configuration 1 (fixed) to Configuration 2 (moveable), the decreasing in stiffness results in reduced frequency values.

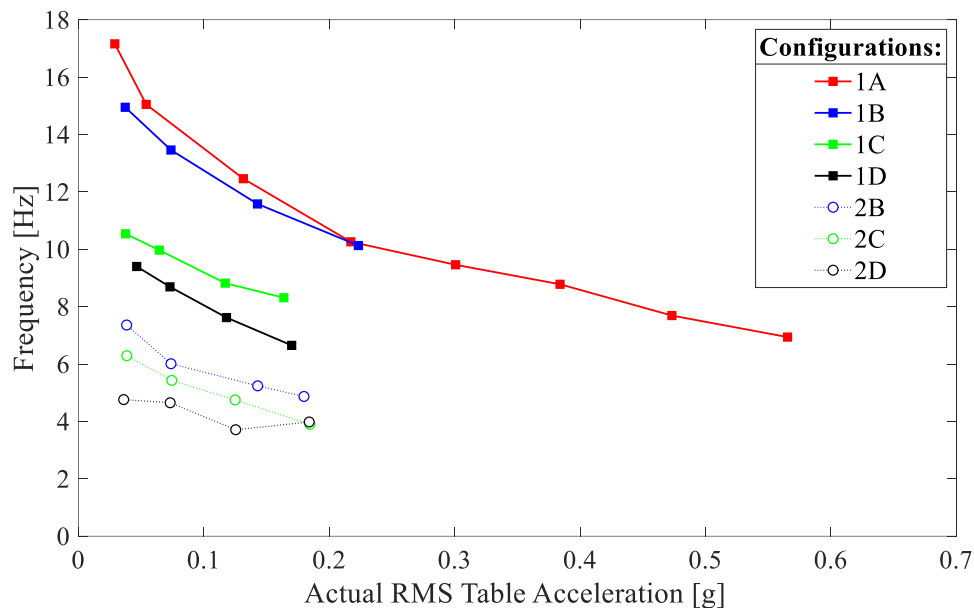


Figure 50: Fundamental frequency as a function of acceleration.

Figure 51 investigates the damping ratio as a function of the input RMS table acceleration for all the configurations. Due to the dissipative properties of the gum layer, the initial values of damping ratio turn out to be very high. As acceleration increases, damping ratio increases because of the large movements.

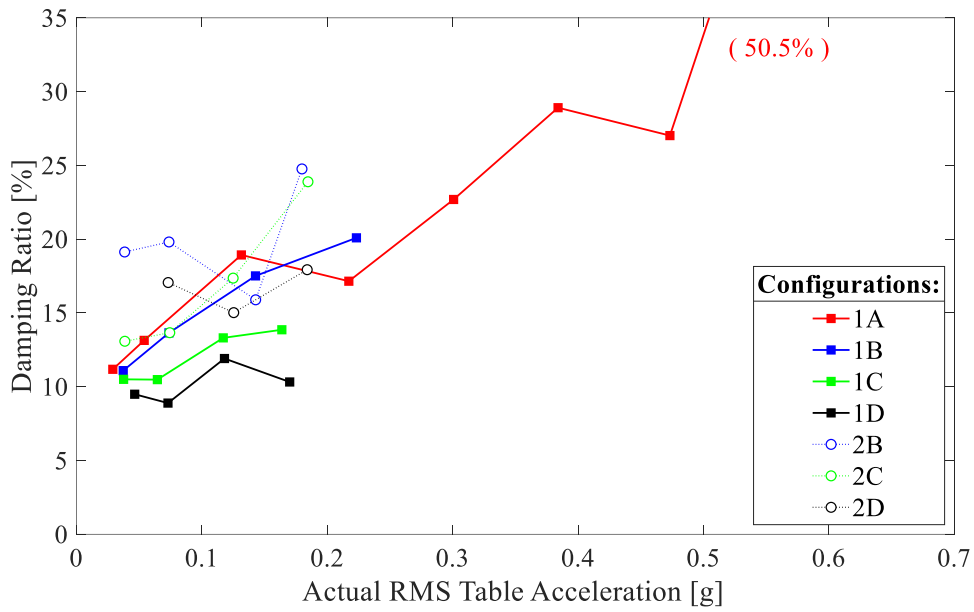


Figure 51: Damping ratio as a function of acceleration.

The amplification factor is then computed as the ratio between the RMS acceleration recorded by the accelerometers on the keystone and on the table. As can be seen in **Figure 52**, the amplification factor decreases as acceleration increases (and damping ratio increases).

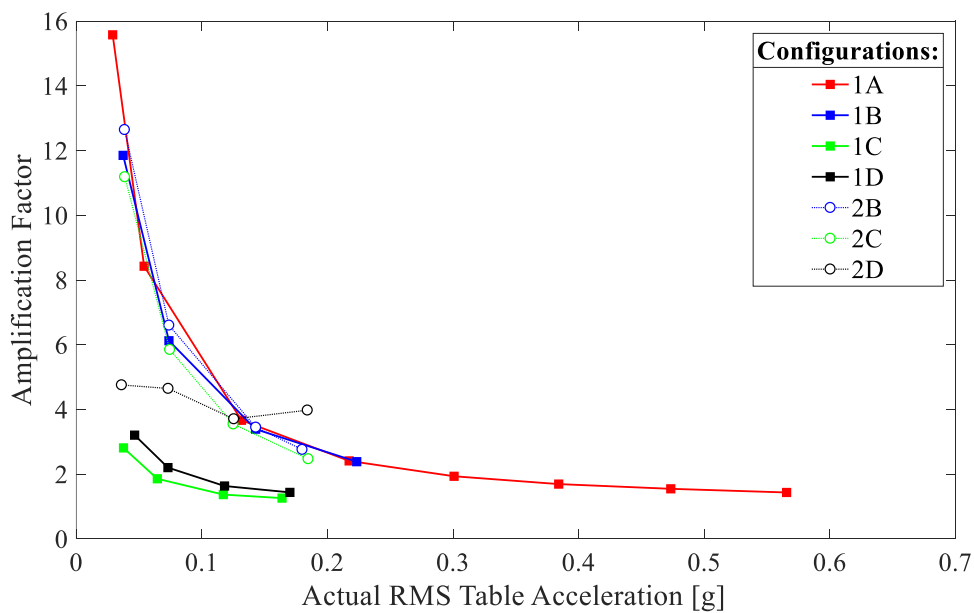


Figure 52: Amplification factor as a function of acceleration.

The effect of the lateral confinement is pointed out by the difference between Configurations 1A and 1B with continuous panels, and Configurations 1C and 1D with interrupted panels or no panels. Indeed, the stronger the confinement is, the larger results being the amplification factor.

5.2 Fixed configuration

The failure mechanism observed for the vault in the fixed configuration suggests the formation of a linear opening, that is orthogonal to the input direction, as it is shown by **Figure 53**.



Figure 53: Crack opening leading to collapse in test 52.

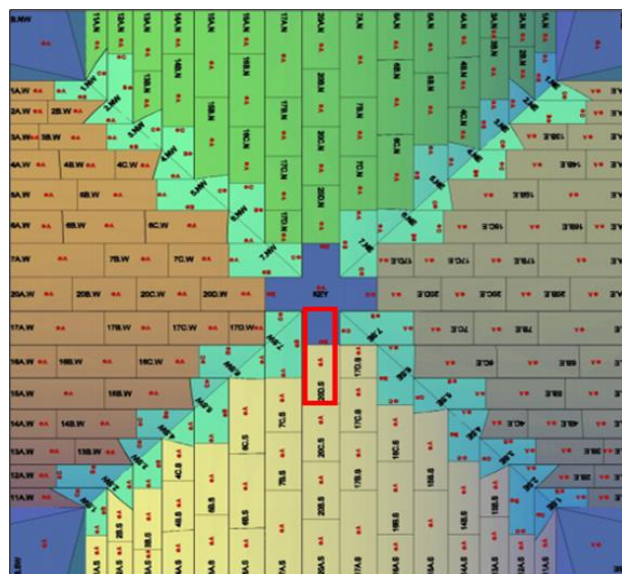


Figure 54: Crack opening of interest.

The most critical area to investigate is the opening between the keystone and the adjacent brick, highlighted in **Figure 54**. The aim is to find the maximum space, in x and y direction, recorded just before and at collapse, to get a damage limit of the failure line width in x and y. Therefore, tests near collapse for Configurations 1A and 1B are examined and the various measures of this opening are reported in **Tables 6** and **7**.

Test Number and Configuration	PTA and Frequency	X Displacement between keystone and brick of interest	Y Displacement between keystone and brick of interest
38 (1A-no collapse)	0.85g, 15Hz	0.2 mm	0.2 mm
39 (1A-no collapse)	0.85g, 10Hz	0.6 mm	0.5 mm
40 (1A-no collapse)	0.85g, 8Hz	1.2 mm	1.0 mm
41 (1A-no collapse)	0.85g, 5Hz	3.2 mm	1.5 mm
42 (1A-no collapse)	0.85g, 2Hz	1.7 mm	1.5 mm
48 (1A-no collapse)	0.95g, 15Hz	0.6 mm	0.2 mm
49 (1A-no collapse)	0.95g, 10Hz	0.8 mm	0.2 mm
50 (1A-no collapse)	0.95g, 8Hz	1.4 mm	0.5 mm
51 (1A-no collapse)	0.95g, 5Hz	4.1 mm	1.1 mm
52 (1A-collapse)	0.95g, 2Hz	25.3 mm	10.3 mm
37 (1A-no collapse)	0.80g, 2Hz	1.5 mm	1.1 mm
42 (1A-no collapse)	0.85g, 2Hz	1.7 mm	1.5 mm
47 (1A-no collapse)	0.90g, 2Hz	2.7 mm	2.3 mm
52 (1A-collapse)	0.95g, 2Hz	25.3 mm	10.3 mm

Table 6: Failure line width for Configuration 1A.

Test Number and Configuration	PTA and Frequency	X Displacement between keystone and brick of interest	Y Displacement between keystone and brick of interest
89 (1B-no collapse)	0.50g, 50Hz	0.1 mm	0.1 mm
90 (1B-no collapse)	0.50g, 20Hz	0.1 mm	0.1 mm
91 (1B-no collapse)	0.50g, 15Hz	0.2 mm	0.1 mm
92 (1B-no collapse)	0.50g, 10Hz	0.3 mm	0.4 mm
93 (1B-no collapse)	0.50g, 8Hz	0.5 mm	0.4 mm

94 (1B-no collapse)	0.50g, 5Hz	0.2 mm	0.2 mm
95 (1B-no collapse)	0.50g, 3Hz	0.2 mm	0.2 mm
96 (1B-no collapse)	0.50g, 2Hz	0.2 mm	0.2 mm
99 (1B-no collapse)	0.75g, 50Hz	0.1 mm	0.1 mm
100 (1B-no collapse)	0.75g, 20Hz	0.2 mm	0.1 mm
101 (1B-no collapse)	0.75g, 15Hz	0.2 mm	0.2 mm
102 (1B-no collapse)	0.75g, 10Hz	0.5 mm	0.4 mm
103 (1B-no collapse)	0.75g, 8Hz	0.7 mm	0.6 mm
104 (1B-no collapse)	0.75g, 5Hz	2.1 mm	1.1 mm
105 (1B-no collapse)	0.75g, 3Hz	1.1 mm	0.6 mm
106 (1B-no collapse)	0.75g, 2Hz	0.9 mm	0.5 mm
121 (1B-no collapse)	0.10g, 3Hz	0.1 mm	0.1 mm
123 (1B-no collapse)	0.20g, 3Hz	0.1 mm	0.1 mm
125 (1B-no collapse)	0.30g, 3Hz	0.1 mm	0.1 mm
127 (1B-no collapse)	0.40g, 3Hz	0.1 mm	0.1 mm
129 (1B-no collapse)	0.50g, 3Hz	0.1 mm	0.2 mm
131 (1B-no collapse)	0.60g, 3Hz	0.3 mm	0.3 mm
133 (1B-no collapse)	0.70g, 3Hz	0.5 mm	0.3 mm
135 (1B-no collapse)	0.80g, 3Hz	4.6 mm	1.7 mm
137 (1B-no collapse)	0.90g, 3Hz	13.0 mm	4.7 mm
139 (1B-collapse)	1.00g, 3Hz	56.5 mm	8.2 mm

Table 7: Failure line width for Configuration 1B.

The failure line values are obtained by plotting the X displacement-time history between the closest keystone marker to the opening KEY.D and the one relative to the brick 20D.S.A. Two graphs to collapse are reported as an example in **Figure 55**.

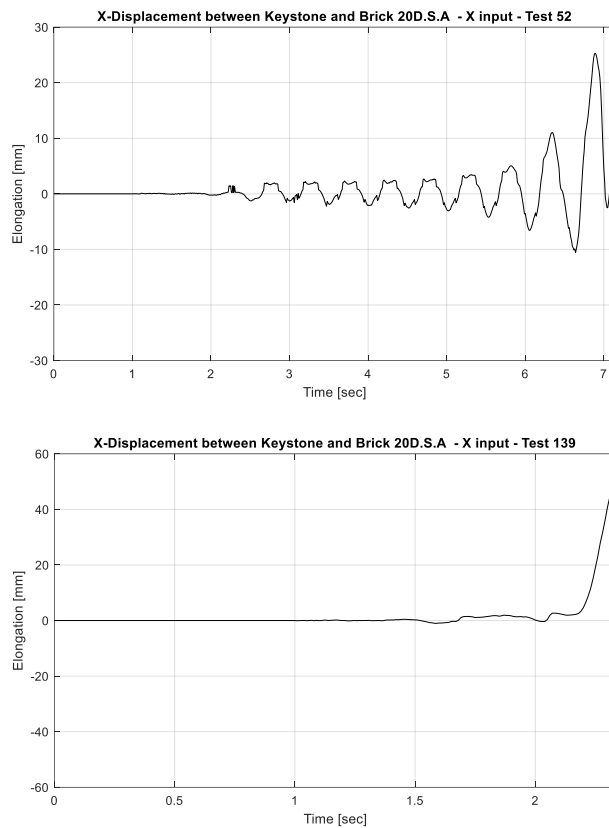


Figure 55: Elongation values between keystone and brick.

The relationship between the different variables is better investigated by the graphs in **Figures 56-59**, which are referred to Configurations 1A (wooden panels) and 1B (plexiglass panels). The graphs show the cumulative displacement in a series of test with respect to the Frequency (for a fixed PTA) and the PTA (for a fixed frequency). An additional Y axis on the right indicates the percentage of displacement with respect to the arch span of 2 m.

On average, it can be observed that as frequency decreases or PTA increases, displacement in each direction increases. Approaching small frequencies, this difference in displacement becomes bigger. Moreover, displacements in X are greater than the Y displacements, as expected due to the X direction of the seismic action.

As regards Configuration 1A with wooden panels, the X displacement value at collapse can be assumed equal to around 1.7% spread of the longitudinal span and the Y displacement equal to 0.8%.

As to Configuration 1B with plexiglass panels, the displacements at collapse are equal or bigger than in 1A, being 4% in X and 0.8% in Y; this suggests the possibility of a more flexible behaviour.

In the end, considering wooden panels confinement, the overcome of a displacement in X and Y between keystone and brick equal to around 30 mm and 15 mm respectively, can lead to instability and to the subsequent collapse. By moving to a plexiglass panels confinement, the Y limit value remains similar, while the X value at collapse increases to 75 mm.

Therefore, as concerns the fixed configuration, the change in confinement more than doubles the failure line limit in X, showing a safer behaviour.

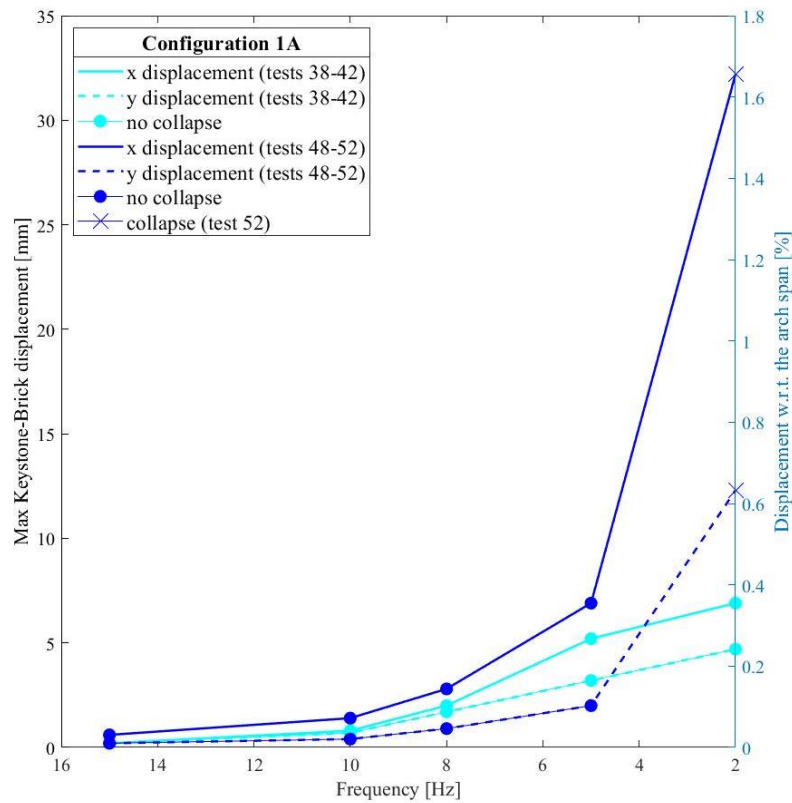


Figure 56: Displacement as a function of frequency for Configuration 1A.

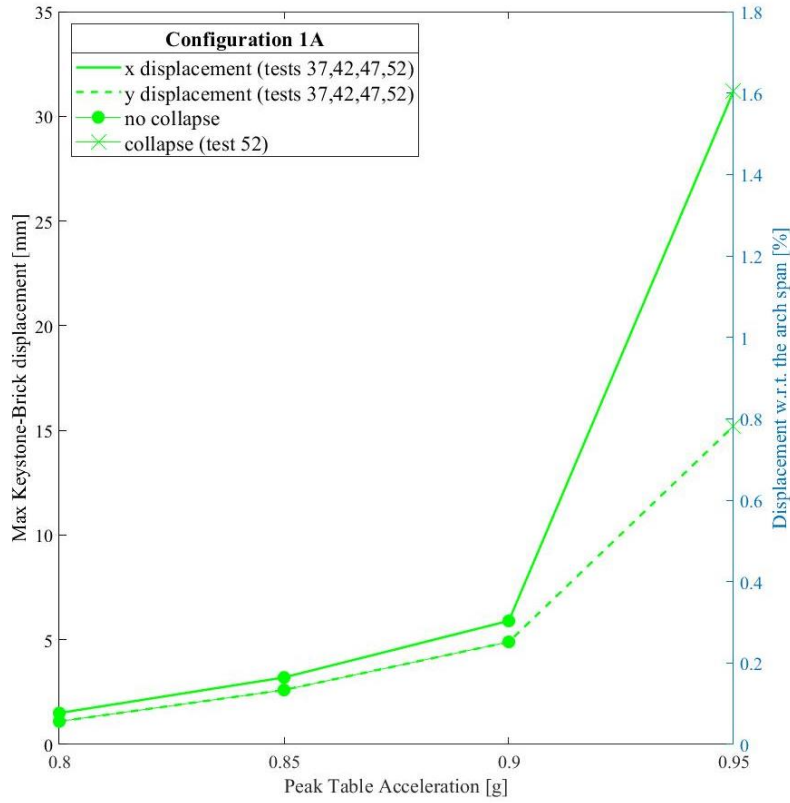


Figure 57: Displacement as a function of PTA for Configuration 1A.

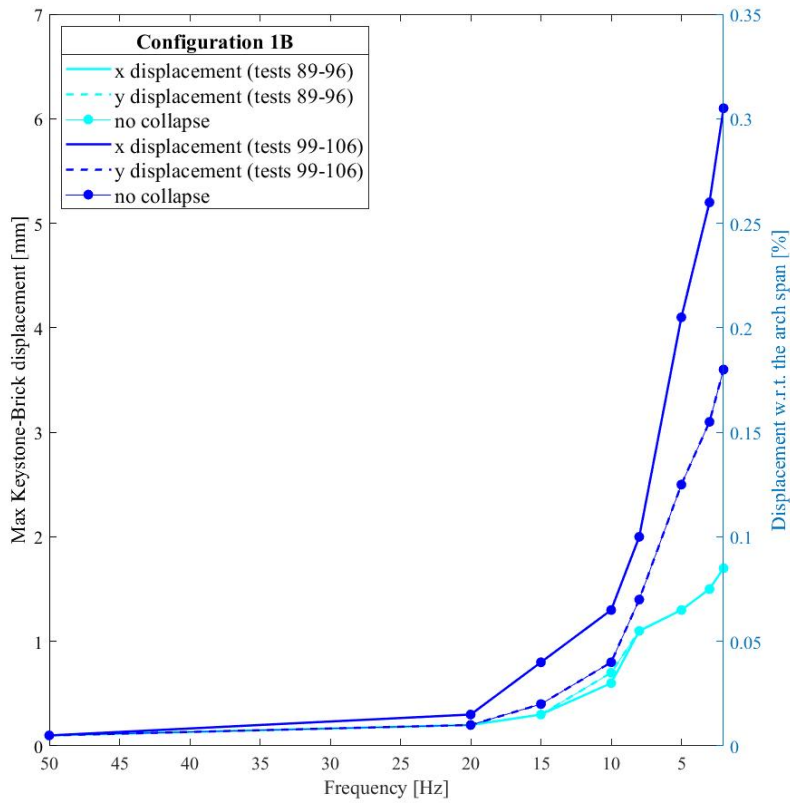


Figure 58: Displacement as a function of PTA for Configuration 1B.

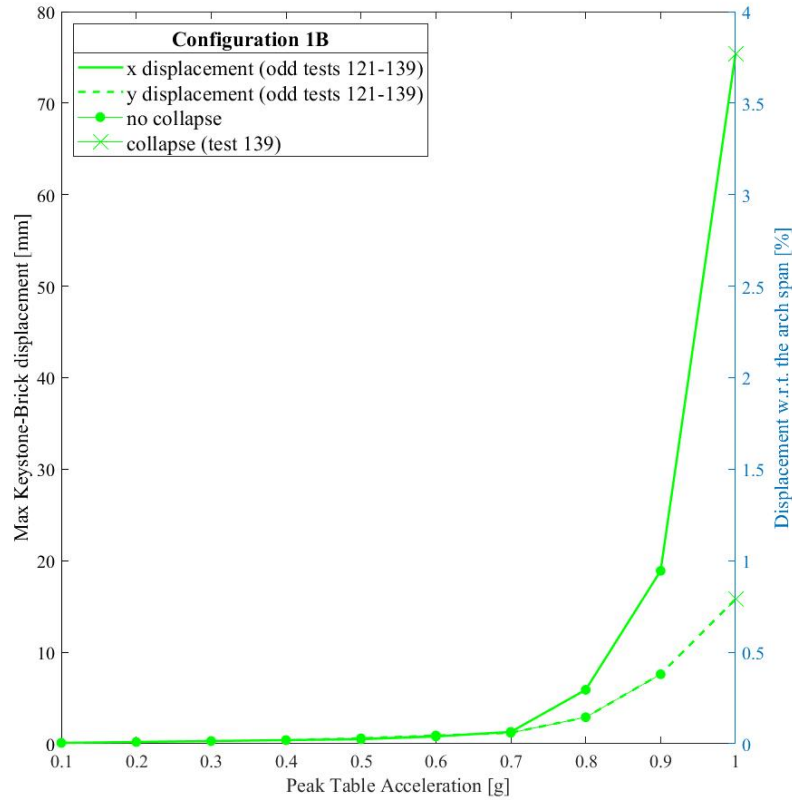


Figure 59: Displacement as a function of PTA for Configuration 1B.

5.3 Moveable configuration

The response of the groin vault model has then been investigated in the moveable configurations, to validate the shear displacement and to find the value of the spring deformation leading to failure.

The maximum absolute space displacements of the markers SE and NE (on the east side in **Figure 60**), corresponding to the moving corners, are recorded for each test. Then, the percentage shear values, with respect to the arch span of 2 m, are computed as a rough indication of damage limits of similar vaults.

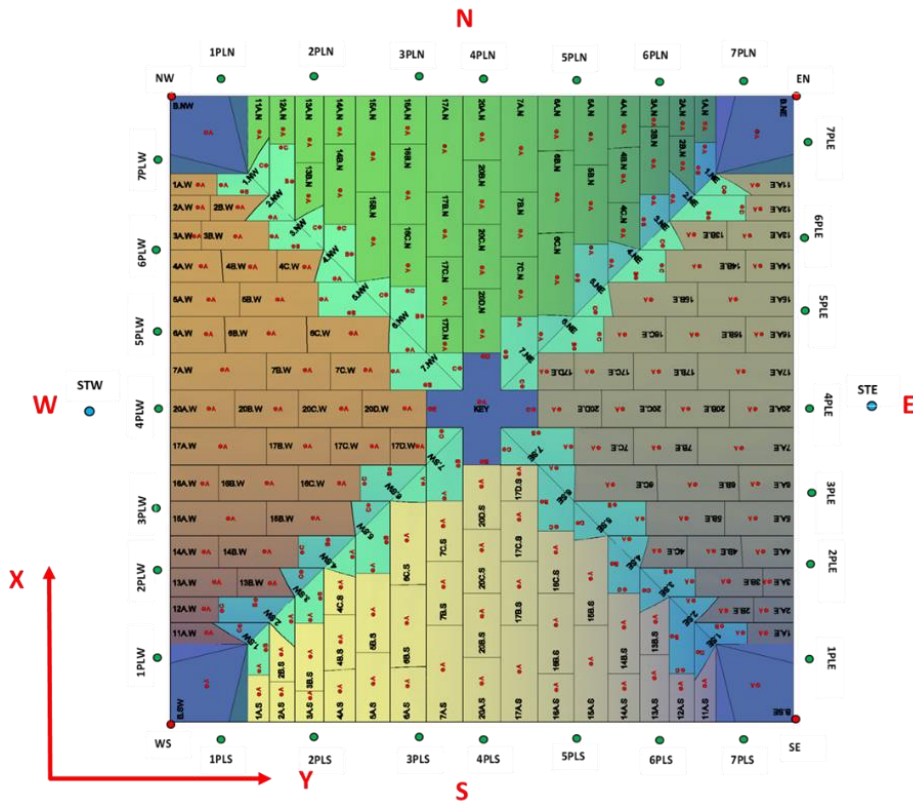


Figure 60: Markers layout.

It is worth pointing out that the markers SE and NE show almost the same displacement-time history in X, as can be seen in **Figure 61**. Therefore, the absolute maximum displacement was selected in a range of similar values.

At first, for the same PTA, Configurations 2B (plexiglass panels) and 2C (cut plexiglass panels) are compared in terms of displacement with respect to the Frequency. A detail of the cut panels in configuration 2C is visible in **Figure 62**. After that, displacements with respect to PTA are analyzed for Configurations 2B and 2D (no panels), under the same Frequency.

Tables 8 and **9** summarize all the results.

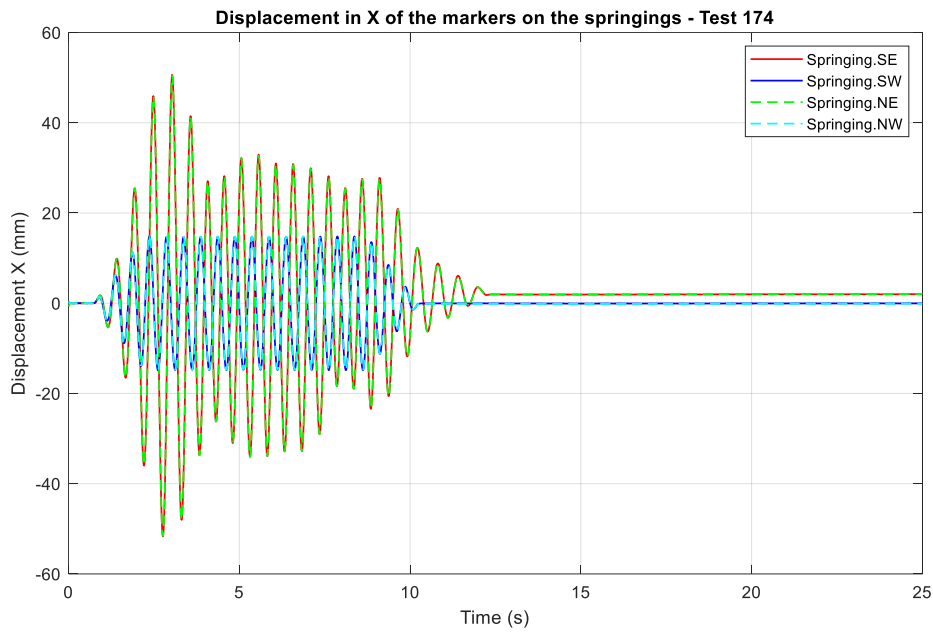


Figure 61: Displacement-time history of the markers on the corners in test 174.



Figure 62: Detail of a cut plexiglass panel.

Test Number and Configuration	PTA and Frequency	Shear Displacement	% Dimensionless Shear Displacement (w.r.t. the arch span of 2 m)
152 (2B-no collapse)	0.10g, 50Hz	0.1 mm	0.01%
153 (2B-no collapse)	0.10g, 20Hz	0.1 mm	0.01%
154 (2B-no collapse)	0.10g, 15Hz	0.3 mm	0.02%
155 (2B-no collapse)	0.10g, 10Hz	0.5 mm	0.03%
156 (2B-no collapse)	0.10g, 8Hz	0.9 mm	0.05%
157 (2B-no collapse)	0.10g, 6Hz	2.1 mm	0.11%

158 (2B-no collapse)	0.10g, 5Hz	3.4 mm	0.17%
159 (2B-no collapse)	0.10g, 4Hz	5.1 mm	0.26%
160 (2B-no collapse)	0.10g, 3Hz	4.0 mm	0.20%
161 (2B-no collapse)	0.10g, 2Hz	1.6 mm	0.08%
162 (2B-no collapse)	0.10g, 1Hz	1.1 mm	0.20%
164 (2B-no collapse)	0.25g, 50Hz	0.3 mm	0.02%
165 (2B-no collapse)	0.25g, 20Hz	0.2 mm	0.01%
166 (2B-no collapse)	0.25g, 15Hz	0.5 mm	0.03%
167 (2B-no collapse)	0.25g, 10Hz	1.1 mm	0.06%
168 (2B-no collapse)	0.25g, 8Hz	1.7 mm	0.09%
169 (2B-no collapse)	0.25g, 6Hz	3.7 mm	0.19%
170 (2B-no collapse)	0.25g, 5Hz	5.9 mm	0.30%
171 (2B-no collapse)	0.25g, 4Hz	11.0 mm	0.55%
172 (2B-no collapse)	0.25g, 3Hz	20.7 mm	1.04%
173 (2B-partial collapse)	0.25g, 2Hz	53.6 mm	2.68%
174 (2B-collapse)	0.25g, 2Hz	60.0 mm	3.00%
177 (2B-no collapse)	0.05g, 3Hz	0.4 mm	0.02%
179 (2B-no collapse)	0.10g, 3Hz	3.1 mm	0.16%
181 (2B-no collapse)	0.15g, 3Hz	12.6 mm	0.63%
183 (2B-no collapse)	0.20g, 3Hz	16.0 mm	0.80%
185 (2B-no collapse)	0.25g, 3Hz	20.9 mm	1.05%
187 (2B-no collapse)	0.30g, 3Hz	24.4 mm	1.22%
188 (2B-no collapse)	0.35g, 3Hz	25.5 mm	1.28%
189 (2B-no collapse)	0.40g, 3Hz	27.3 mm	1.37%
190 (2B-no collapse)	0.45g, 3Hz	28.8 mm	1.44%
191 (2B-partial collapse)	0.50g, 3Hz	30.1 mm	1.51%
192 (2B-partial collapse)	0.60g, 3Hz	32.2 mm	1.61%
193 (2B-partial collapse)	0.75g, 3Hz	33.6 mm	1.68%
194 (2B-collapse)	1.0g, 3Hz	55.3 mm	2.77%

Table 8: Shear displacement values for Configuration 2B.

Test Number and Configuration	PTA and Frequency	Shear Displacement	% Dimensionless Shear Displacement (w.r.t. the arch span of 2 m)
214 (2C-no collapse)	0.10g, 50Hz	0.1 mm	0.01%
215 (2C-no collapse)	0.10g, 20Hz	0.1 mm	0.01%
216 (2C-no collapse)	0.10g, 15Hz	0.2 mm	0.01%
217 (2C-no collapse)	0.10g, 10Hz	0.5 mm	0.03%
218 (2C-no collapse)	0.10g, 8Hz	0.8 mm	0.04%
219 (2C-no collapse)	0.10g, 6Hz	2.1 mm	0.11%
220 (2C-no collapse)	0.10g, 5Hz	3.2 mm	0.16%
221 (2C-no collapse)	0.10g, 4Hz	4.9 mm	0.25%
222 (2C-no collapse)	0.10g, 3Hz	7.4 mm	0.37%
223 (2C-no collapse)	0.10g, 2Hz	2.0 mm	0.10%
224 (2C-no collapse)	0.10g, 1Hz	2.2 mm	0.20%
226 (2C-no collapse)	0.25g, 50Hz	0.1 mm	0.01%
227 (2C-no collapse)	0.25g, 20Hz	0.2 mm	0.01%
228 (2C-no collapse)	0.25g, 15Hz	0.4 mm	0.02%
229 (2C-no collapse)	0.25g, 10Hz	1.1 mm	0.06%
230 (2C-no collapse)	0.25g, 8Hz	1.5 mm	0.08%
231 (2C-no collapse)	0.25g, 6Hz	0.2 mm	0.01%
232 (2C-no collapse)	0.25g, 5Hz	5.4 mm	0.27%
233 (2C-no collapse)	0.25g, 4Hz	10.5 mm	0.53%
234 (2C-no collapse)	0.25g, 3Hz	20.8 mm	1.04%
235 (2C-partial collapse)	0.25g, 2Hz	51.7 mm	2.59%
236 (2C-collapse)	0.25g, 2Hz	81.4 mm	4.07%
254 (2D-no collapse)	0.05g, 3Hz	1.4 mm	0.07%
258 (2D-no collapse)	0.10g, 3Hz	9.6 mm	0.48%
261 (2D-no collapse)	0.15g, 3Hz	14.1 mm	0.71%
262 (2D-no collapse)	0.20g, 3Hz	16.4 mm	0.82%
263 (2D-no collapse)	0.25g, 3Hz	18.6 mm	0.93%
264 (2D-no collapse)	0.30g, 3Hz	19.4 mm	0.97%
265 (2D-no collapse)	0.35g, 3Hz	20.8 mm	1.04%
266 (2D-collapse)	0.40g, 3Hz	20.5 mm	1.03%

Table 9: Shear displacement values for Configurations 2C and 2D.

The displacement values of 2B and 2C Configurations are hereafter collected in a graph (**Figure 63**) with reference to the relative test Frequency and for the same Peak Table Acceleration of 0.10g and 0.25g.

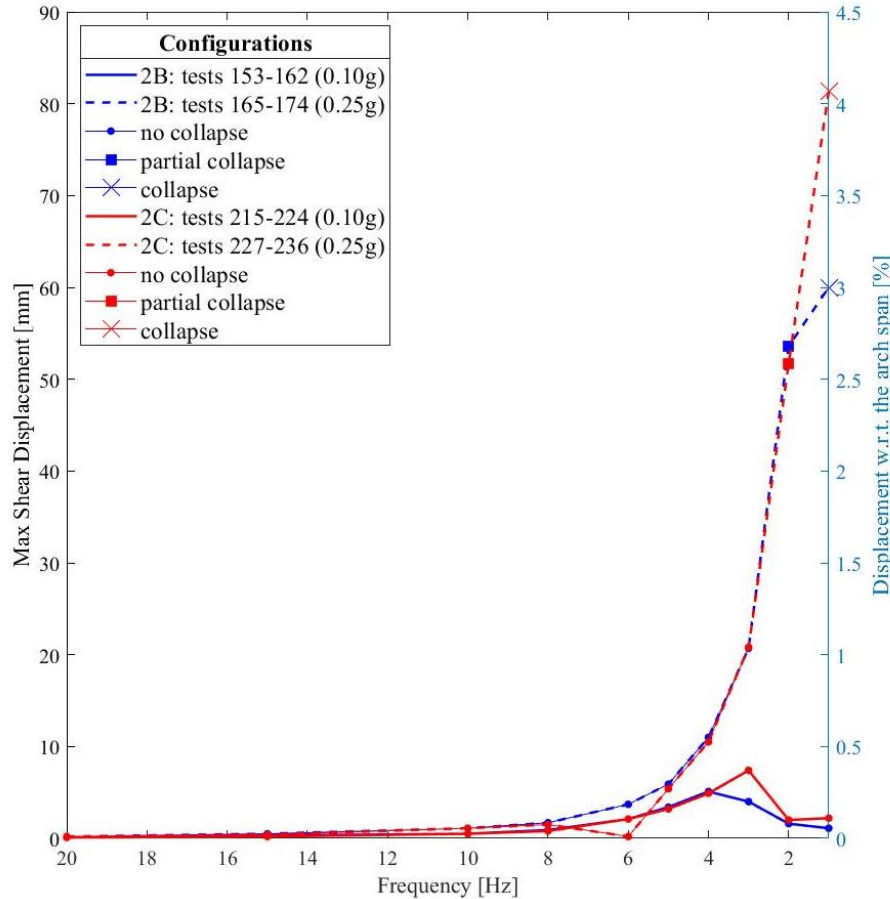


Figure 63: Shear displacement as a function of frequency for Configurations 2B and 2C.

As can be noted, the vault with plexiglass panels reaches the partial collapse at 2.68% and the total collapse at 3% spread of the longitudinal span, at 2 Hz and PTA of 0.25g. As regards the vault with cut plexiglass panels, under the same conditions, it reaches the partial collapse at 2.59% and the total at 4.07% spread of the longitudinal span.

Therefore, the difference in shear displacement between the configurations with plexiglass panels and cut plexiglass panels is quite small; the two configurations show a similar trend.

The graph in **Figure 64** illustrates the results of Configurations 2B and 2D with reference to the Peak Table Acceleration of each test and for the same Frequency of 3 Hz.

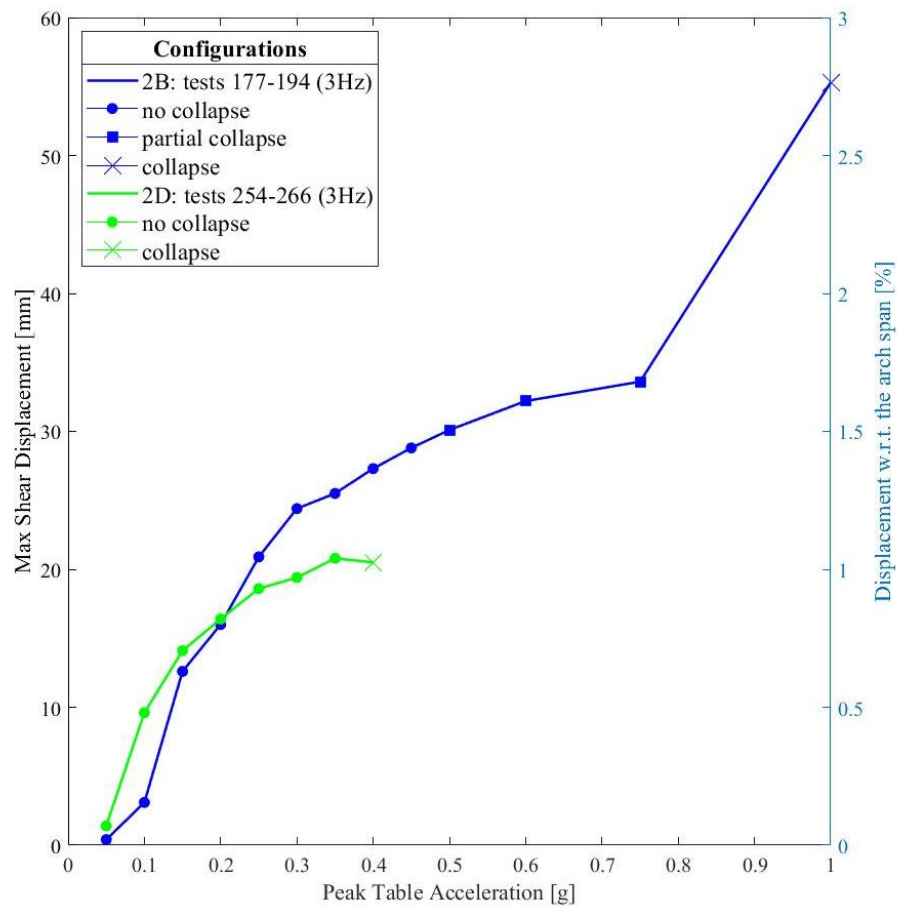


Figure 64: Shear displacement as a function of PTA for Configurations 2B and 2D.

As expected, the vault without panels in Configuration 2D (wood panels only in the corners) goes to failure for a shear displacement of 1.03%, that is a much smaller value than the other settings. This confirms the reason why vaults in buildings are, in general, properly bounded by a lateral confinement.

Regarding Configuration 2B, the vault starts to collapse with a spring deformation of 1.51% for 0.5g, up to reach gradually the total collapse at 2.77% of shear displacement for a PTA of 1g.

In conclusion, as regards the moveable Configuration, collapse occurs after the reaching of a shear displacement at the moveable corners equal to approximately 3% of the longitudinal span. This percentage can be assumed as a limit value for the moveable configuration. Moreover, this is in good agreement with the values obtained by Carfagnini et al. (2018) [2], Gaetani (2016) [3], Rossi et al. (2014) [4], and Milani et al. (2016) [5].

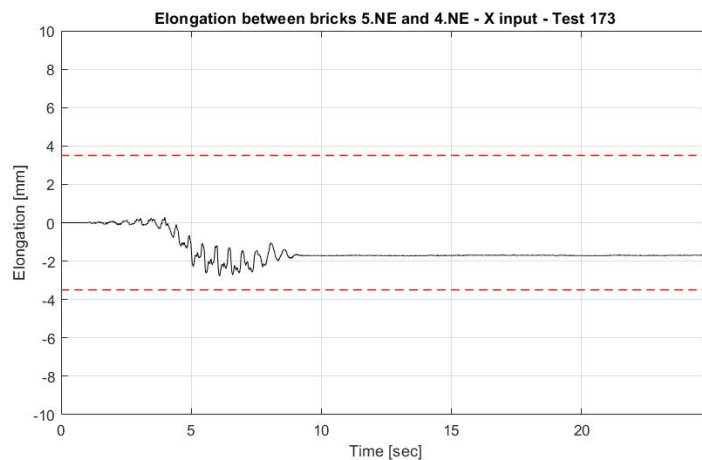
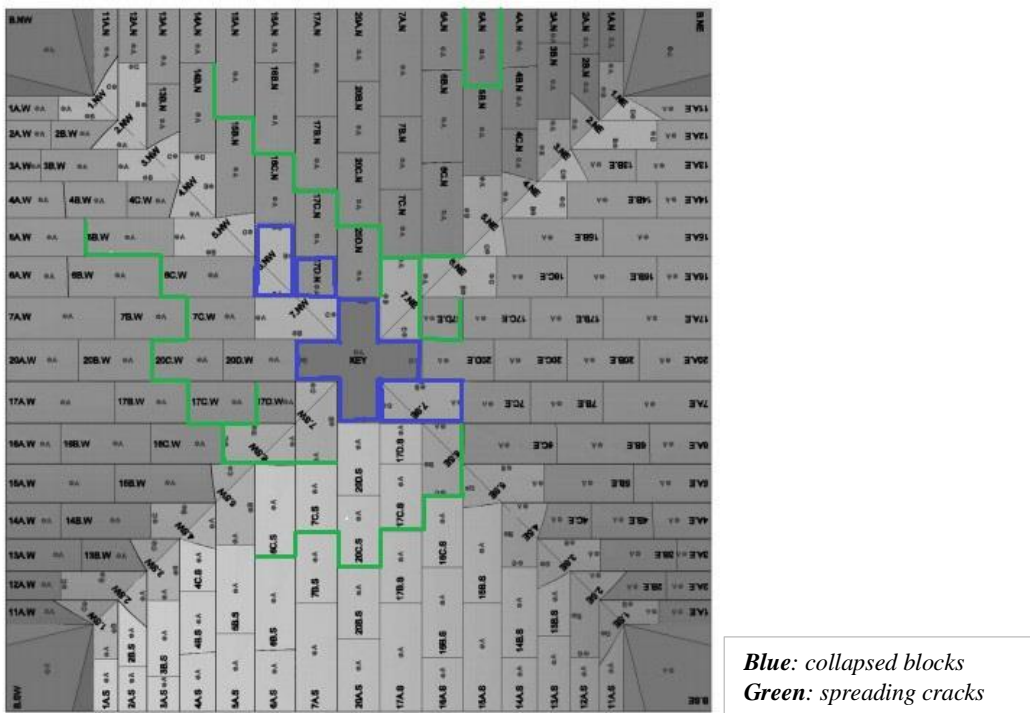
6. Critical arch elongation

The shear displacement is associated to the simultaneous elongation and shortening of the diagonal arches in the moveable setting. To better understand the collapse mechanisms, a suitable approach consists in studying how the length of these arches changes during tests. Given that the portions around the corners of the vault are sub-vertical, they are subjected to higher compression forces, by showing a mainly rigid behavior. Therefore, the purpose is to define a critical elongation of “sub-horizontal zones”, where compression forces, that are responsible for the arch equilibrium, are no longer able to withstand its own weight, leading to collapse.

The first step is to measure the “critical” elongation between two bricks of the diagonals. This means, experimentally, to observe how much space can be occupied by the adjacent gum layers of the blocks up to collapse. To do so, tests near the failure are examined and based on a previous work, it is taken into account that the space between blocks for a central arch (not diagonal) was measured around 3 mm.

Here below, a series of graphs are reported to evaluate the elongation between the markers of the bricks that are chosen in a critical area of the diagonal arches, according to a qualitative analysis on the left that highlights collapsed blocks and spreading cracks. The observed general trend is a critical elongation of around 3.5 mm, that is indicated in each graph by a red dotted line.

Figure 65 illustrates the vault mechanism at test 173, in which a partial collapse occurs. An initial diagonal “sliding” cracks (due to shear displacement) forms in the North and West webs, that lead to the failure of central part and to the partial failure of West web. Brick 6 on the NW diagonal collapses, as can be seen from the first graph on the right, where the overcoming of the red dotted line at 3.5 mm causes instability. Bricks 5 and 4 of the NE diagonal do not collapse; indeed in the second graph the red line is not overcome.



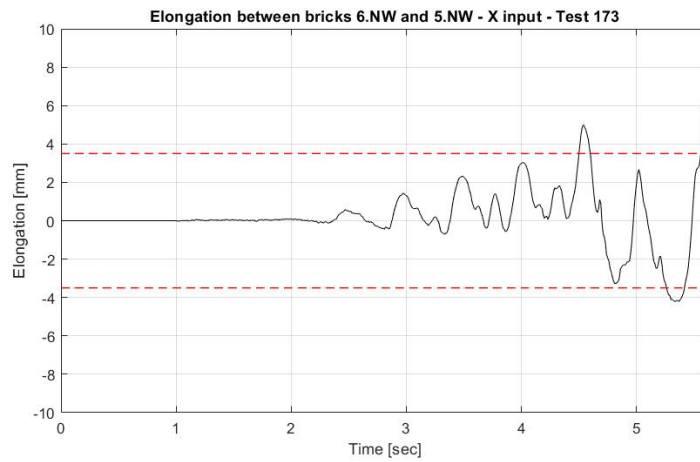
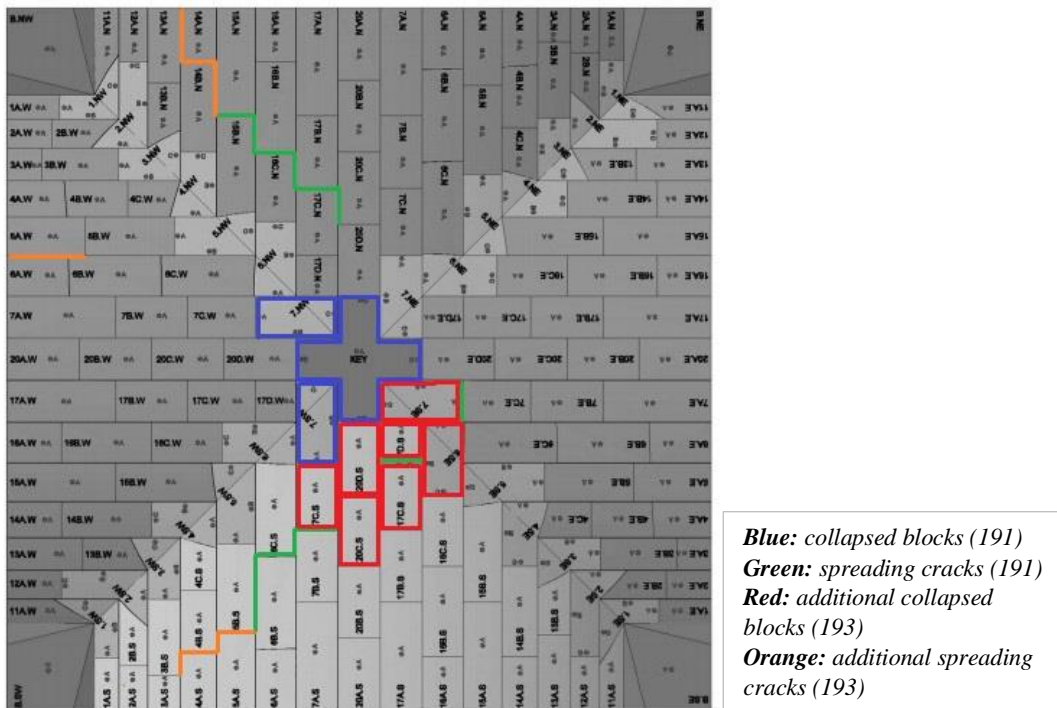


Figure 65: Scheme of the vault behaviour at test 173 and critical elongation examples.

Figure 66 represents the vault at test 193, in which a partial failure has already started from test 191, by spreading mostly in the South Web and in the SE-NW diagonal arch. Bricks 7 and 6 of the SE diagonal collapsed, by surpassing the “gum-layer” threshold. The elongation between the relative markers of bricks 5 and 4 is close to the limit, but it does not overcome it and the two blocks are safe.



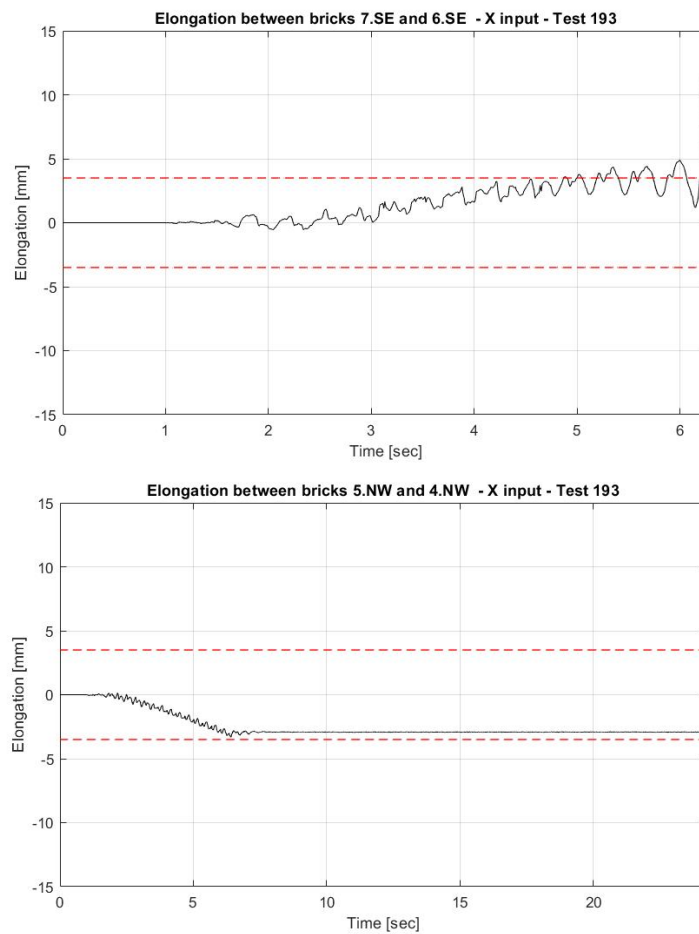


Figure 66: Scheme of the vault behaviour at test 193 and critical elongation examples.

To conclude the analysis, **Figure 67** shows the vault at test 235, in which a partial failure is reached mostly in the NW web because of “sliding” cracks. Bricks 6.NW and 7.NE collapsed, as can be noted in the picture and graphs. Here the critical value of around 3.5 mm is clearly visible.

In view of the foregoing, it can be concluded that 3.5 mm is a suitable value for the critical elongation between two adjacent bricks that, if overcome, causes destabilization and collapse of the involved blocks.

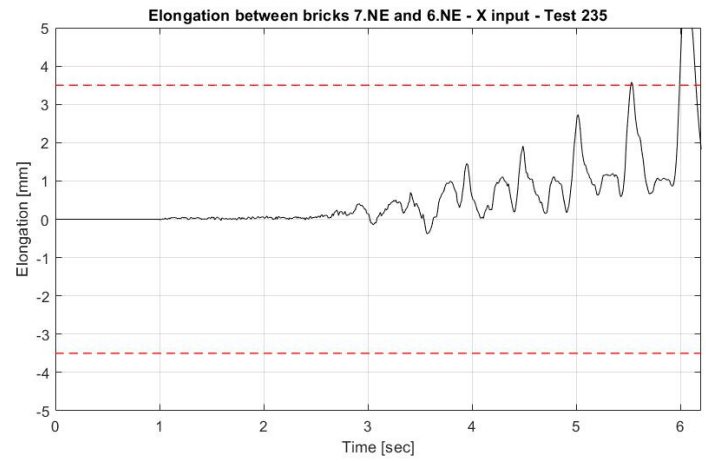
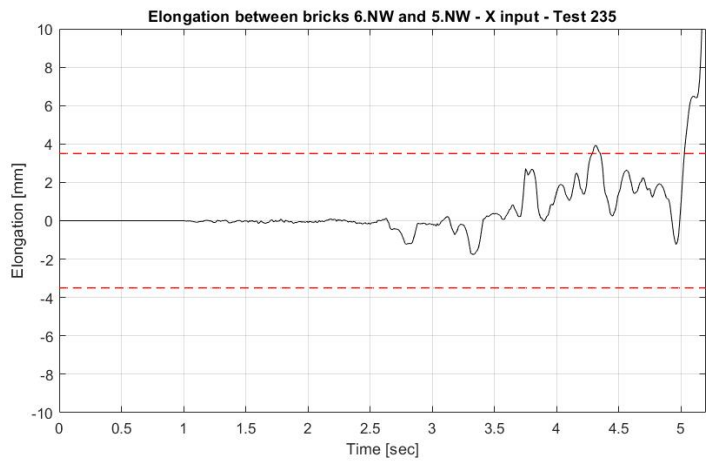
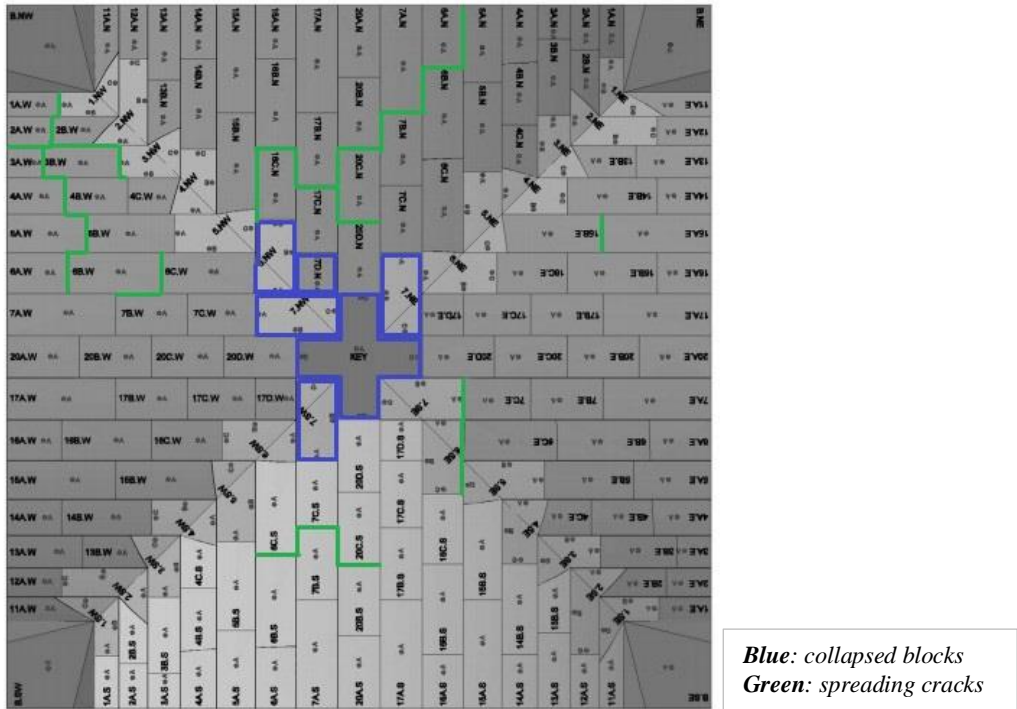


Figure 67: Scheme of the vault behaviour at test 235 and critical elongation examples.

From the assumed critical value of displacement between two adjacent bricks, the next step is to measure the critical elongation of the diagonal arches, whose bricks are the first to collapse after the keystone.

Given that the portions around the corners of the vault showed a rigid behaviour, in the first instance we could assume them as non-deformable, in order to focus on the central part of the diagonal arch.

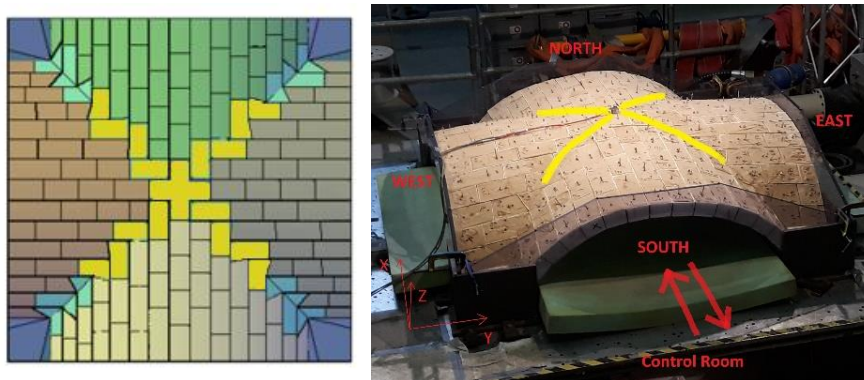


Figure 68: Scheme of the investigated diagonal arch segments.

The two segments in question of the diagonal arches in SE-NW and SW-NE directions are both composed by 9 blocks, as shown in yellow in **Figure 68**.

If the sum of the spaces between the blocks (each of them called s), exceeds a certain value, the compression forces responsible for the equilibrium of the arch are no more able to withstand the weight of the arch itself and collapse occurs. In view of the above consideration, the critical space between bricks is assumed as 3.5 mm.

Therefore, the maximum elongation of the arch portion is indicated as “critical elongation” ΔL and can be calculated by

$$\Delta L = 8s = 8 \cdot 0.35 = 2.8 \text{ cm} = 28 \text{ mm}$$

From a theoretical point of view, if ΔL for the considered portion exceeds the value of 28 mm, the vault collapses. The following provides some demonstrations of this theoretical assumption, based on tests near the collapse for different configurations.

Configuration 1B test 52 (0.95g, 2Hz) – collapse

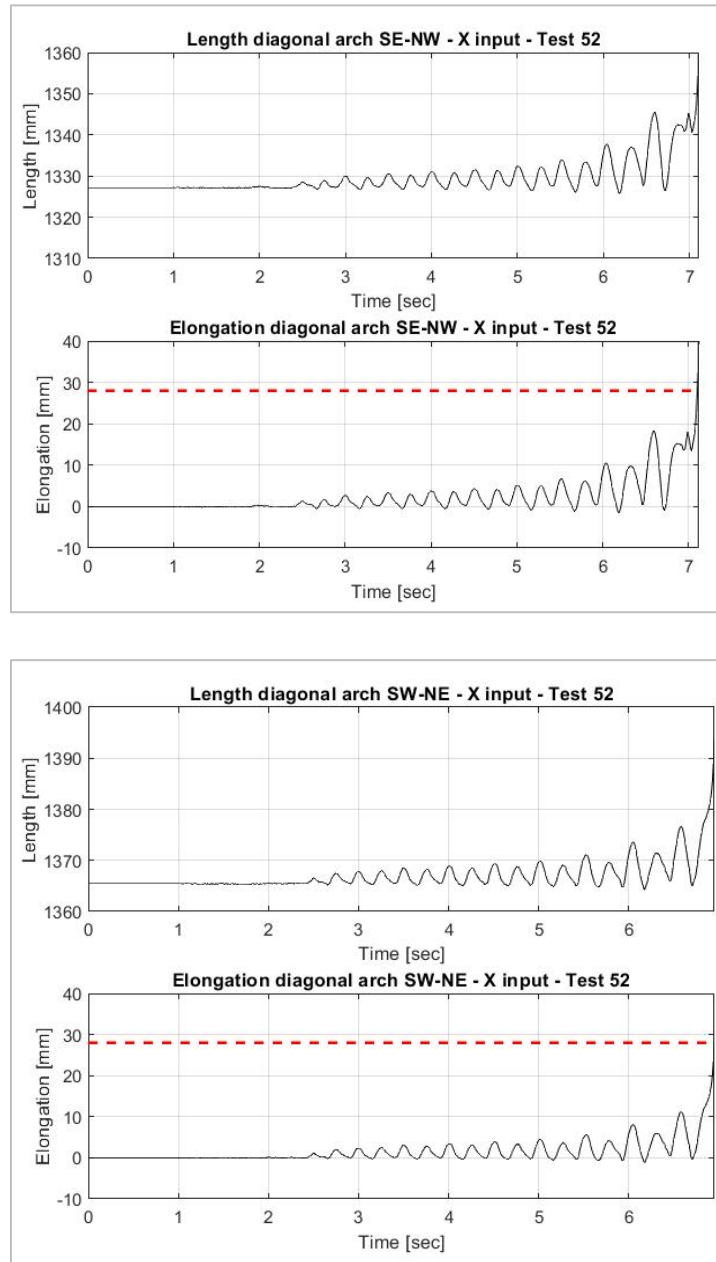


Figure 69: Diagonals length and elongation for test 52.

For the fixed configuration in **Figure 69**, the central portion of the diagonal arch goes to collapse with an elongation of about 28 mm in SE-NW direction and 25 mm in SW-NE direction, by staying around the assumed limit, indicated by the red dotted line.

Configuration 2B test 173 (0.25g, 2Hz) – partial collapse

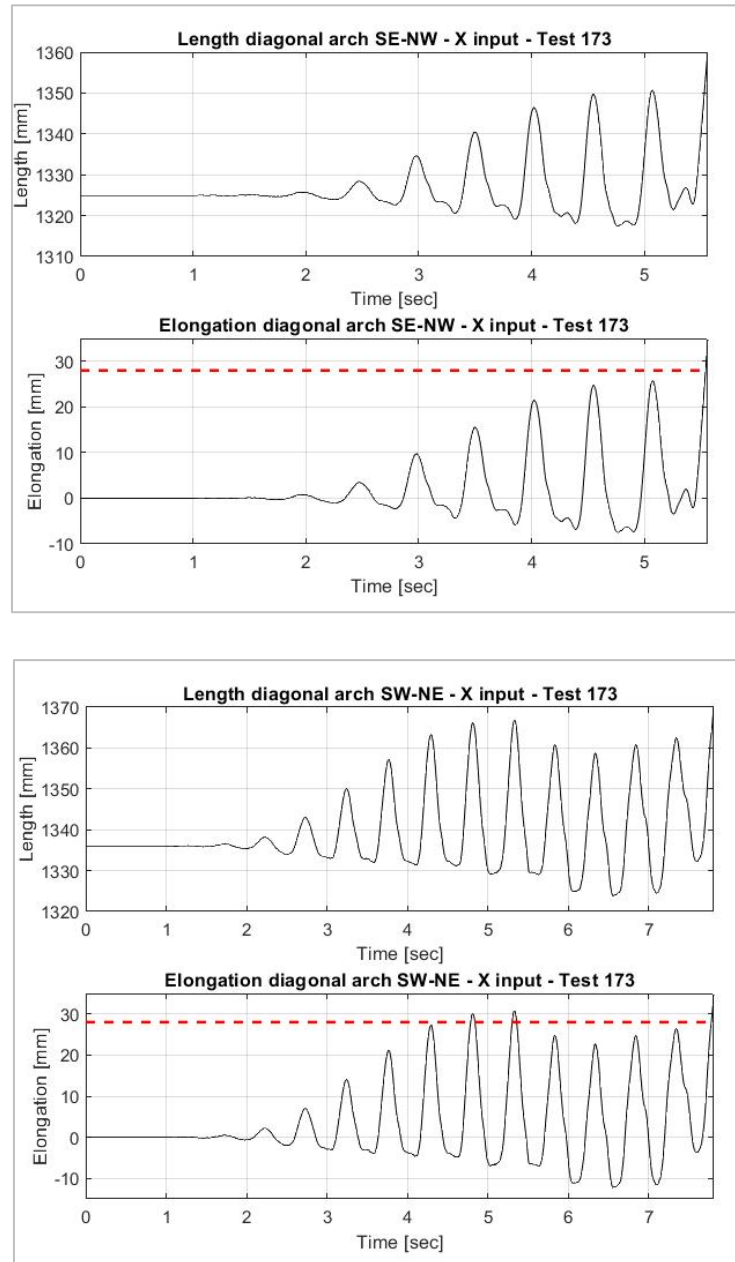


Figure 70: Diagonals length and elongation for test 52.

The time interval for the test with moveable configuration (**Figure 70**) is quite short, given that the partial collapse starts after 5.6 (for SE-NW) and 7.8 seconds (for SW-NE) from the beginning of the test. In the first case, the elongation of the arch near the collapse is around 28 mm; in the second case, an initial loss of equilibrium happens after 5 seconds with an opening between 25 and 30 mm, even if the collapse occurs later. Indeed, the SE-NW diagonal arch tends to collapse before the SW-NE diagonal arch.

Configuration 2B test 193 (0.75g, 3Hz) – partial collapse

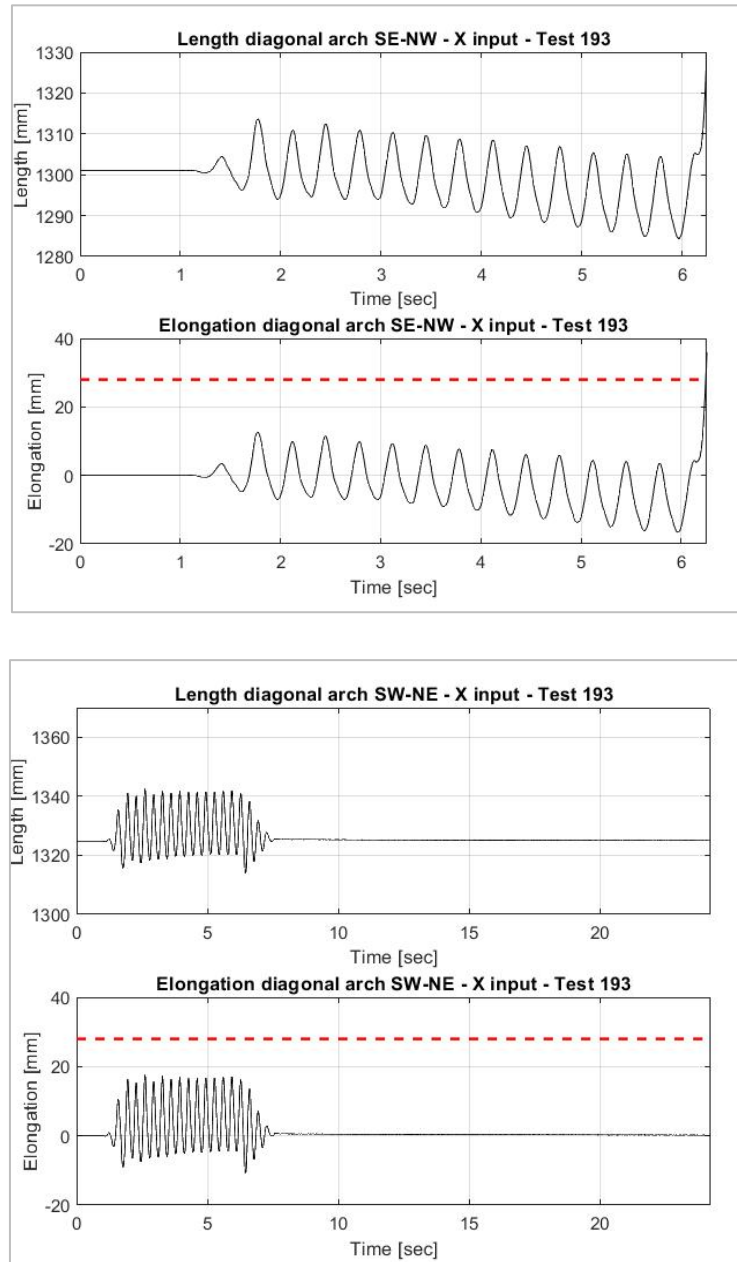


Figure 71: Diagonals length and elongation for test 193.

The collapse for the test in **Figure 71** is partial and it concerns the SE-NW diagonal arch, that reaches destabilization by overcoming the limit of 28 mm. The other diagonal arch withstands the excitation, as can be seen from the graph on the right.

Configuration 2C test 235 (0.25g, 2Hz) – partial collapse

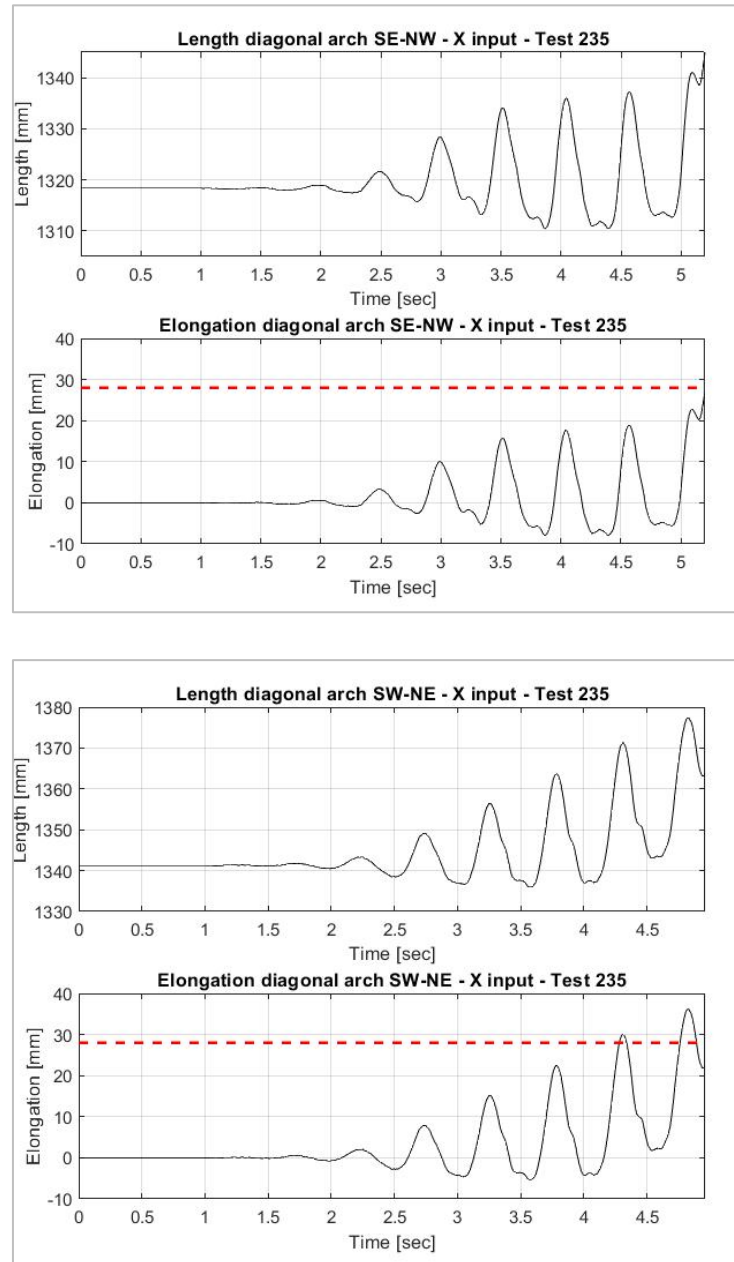


Figure 72: Diagonals length and elongation for test 235.

The diagonal arches collapse approximately the same time in this case (**Figure 72**), differently from test 173 on equal terms, by showing an elongation of about 28 mm for SE-NW and 35 mm for SW-NE. The reason of the difference in time from Configuration 2B may be the cutting of the North and South plexiglass panels, which increases the flexibility of the East side. This could allow cracks to better spread towards the East web, by leading to a simultaneous collapse of the diagonal arches.

In view of the above, it can be concluded that the value of 28 mm is a suitable critical threshold as concerns the elongation of the central part of diagonal arches, for the different configurations. This confirms the first assumption about the critical space between bricks.

Conclusions

The aim of this study was to extract further relevant information about the response of a masonry vault subjected to in-plane shear deformation mechanisms, that are typically the main cause of seismic damage in historic buildings.

The outcomes of the experimental campaign confirmed and improved the results of previous studies.

In particular, the behavior at collapse, named “critical”, is the main issue that has been investigated. The displacement data processing has led to the identification of the two collapse mechanisms related to the fixed and moveable configurations. To follow, a numerical evaluation has been carried out to quantify the respective failure line and shear displacement of the two configurations. Finally, critical elongation values have been introduced in the analysis of the displacements of bricks and diagonals, subjected to the compression forces responsible for the equilibrium of the vault.

The final objective of this work is the possibility to assume “safe limits” in the future seismic design and testing of masonry vaults, in a perspective of preservation.

References

- [1] G. Castellazzi, Mechanics of Historical Masonry Structures-Course Notes.
- [2] E. Britannica, «Vault,» [Online]. Available: <https://www.britannica.com/technology/vault-architecture>.
- [3] J. Michalew, «Ancient and Medieval Architecture,» [Online]. Available: <https://medievalheritage.eu/en/main-page/dictionary/groin-vault/>.
- [4] S. Huerta, «Galileo was Wrong: The Geometrical Design of MASONRY Arches,» 2006.
- [5] S. Mastrodicasa, Dissesti statici nelle strutture edilizie, HOEPLI, 1993.
- [6] F. Giovanetti, Manuale del recupero del comune di Città di Castello, DEI, 2000.
- [7] S. Holzer, «Vault analysis: continuum mechanics and rigid body approaches,» *Construction History Europe- an Summer School: Two Millennia of Vaults, Domes and*, 2011.
- [8] A. Gaetani, «Seismic Performance of Masonry Cross Vaults: Learning from Historical Development and Experimental Testing,» 2016.
- [9] M. Como, «Statics of historic masonry constructions,» *Springer-Verlag Berlin Heidelberg*, 2013.
- [10] R. Mark, J. Abel e K. and O'Neill, «Photoelastic and finite-element analysis of a quadripartite vault,» *Experimental Mechanics*, 1973.
- [11] R. Mark, Experiments in gothic structure, Cambridge: The MIT Press, 1982.
- [12] V. Cerardini, «Modelli sperimentali di volte in tufo e mattoni,» *La meccanica delle murature tra teoria e progetto*, 1996.
- [13] P. Faccio, P. Foraboschi e E. and Siviero, «Volte in muratura con rinforzi in FRP,» *L'Edilizia*, 1999.
- [14] D. Theodossopoulos, «Structural design of High Hothic vaulting systems in England,» *International Journal of Architectural Heritage*, 2008.
- [15] P. Foraboschi, «Strengthening of masonry arches with fiber-reinforced polymer strips,» *Journal of Composites for Construction*, 2004.
- [16] T. Van Mele, J. McInerney, M. DeJong e P. and Block, «Physical and computational discrete modelling of masonry vault collapse.,» *Structural Analysis of Historical Constructions*, 2012.
- [17] M. Rossi, C. Calderini, S. Lagomarsino e G. and Milani, «Seismic response of masonry vaulted structures: experimental and numerical modelling.,» in *9th International Masonry Conference*, Minho, 2014.
- [18] E. Shapiro, «Collapse mechanisms of small-scale unreinforced masonry vaults.,» 2012.
- [19] PERPETUATE, *DELIVERABLE D12 Results of experimental test on damage measures and reference values to be considered*, 2012.
- [20] C. Carfagnini, S. Baraccani, S. Silvestri and D. Theodossopoulos, «The effects of in-plane shear displacements at the springings of Gothic cross vaults.,» 2018.

Acknowledgments

A special thanks to my supervisor Prof. Ing. Stefano Silvestri and my co-supervisor Dr. Ing. Simonetta Baraccani that gave me the chance to join this project during my last days in Bristol. I can't explain my excitement the first day in which, walking out from University, I realized I could be part of this novel experiment. It was a great experience to help you in the laboratory. Despite the following hard and unbelievable times for the entire world, the online meetings, and the inevitable changes in the thesis elaboration, my biggest thanks to you concerns the strong motivation you gave me. I admit that writing a thesis completely in the distance has been a hard work, in which I put all my effort. Nevertheless, your feedback was always stimulating and proactive and I strongly believe that when a Professor "influence you to strive for excellence and make a difference in the world around you", he/she never lets you forget him. Thank you.

I want to thank my family "XL" and my boyfriend. You are the lights that guide me. You always gave me "wings to fly, roots to come back and reasons to stay". I never could be grateful enough for your constant support, for all the chances you never denied to me and for your love. You are my best example of respectable values.

A heartfelt thanks also to my friends, who always sustained me more than I've ever done, and especially in this last year, proved me that with the right people time never goes. I can't wait to see you again and more, because despite this situation, you always reminded me that "Whatever you do in this life, it's not legendary, unless your friends are there to see it." I missed you so much.

Finally, I want to dedicate my thoughts to every colleague, teacher, friend, neighbour and person I spent a good time with in my life, both in Italy and abroad. Each of them taught me that difference is the key to growth, that every experience can change your life, that if you keep your heart open and you are willing to learn, the world never stops to amaze you. And your wealth of memories will always remember you that life is a gift, so it doesn't worth not smiling.

Thank you all.